ABSTRACT

MCLEAN, MORGAN STUART LANCE KENT. A High Resolution Study of the ^{52}Cr(p,p$_0$) and ^{52}Cr(p,p$_1$) Reactions. (Under the direction of Dr. Gary E. Mitchell and Dr. John F. Shriner, Jr.)

High resolution measurements of the ^{52}Cr(p,p$_0$) and ^{52}Cr(p,p$_1$) cross sections were performed at the High Resolution Laboratory (HRL) of the Triangle Universities Nuclear Laboratory (TUNL). Results were obtained for the (p,p$_0$) reaction over the energy range E_p = 2.1039-3.4711 MeV and for the (p,p$_1$) reaction over the energy range E_p = 2.6101-3.4711 MeV. The primary goal was the improvement of the purity and completeness of the level sequences in ^{53}Mn. Excitation functions were generated at five angles for both reaction channels. Fits to the observed cross sections were obtained using the multi-channel, multi-level R-Matrix code, MULTI6. J^π assignments have been given to 263 resonances. Many resonances were observed for the first time, and many previously observed levels were given new quantum number assignments.

Level sequences of specific J^π were evaluated for purity and completeness using statistical tests based on random matrix theory. Several J^π assignments were revised after application of the statistical tests. The resulting nearest-neighbor spacing distributions were compared to the Wigner distribution, and the reduced width distributions were compared to the Porter-Thomas distribution. Estimates of the observed fraction of levels for each sequence were obtained using both the spacing and width distributions. Strength functions and level densities were determined for each J^π sequence. The data for $J = \frac{1}{2}$ allow a test of whether the level density depends on parity; no parity dependence was observed.

A HIGH RESOLUTION STUDY OF THE ^{52}Cr(p,p$_0$) and ^{52}Cr(p,p$_1$) REACTIONS

by

MORGAN STUART LANCE KENT MCLEAN

A dissertation submitted to the Graduate Faculty of North Carolina State University in partial fulfillment of the degree of Doctor of Philosophy

PHYSICS

Raleigh, North Carolina

2005

APPROVED BY:

D. Ronald Tilley

Mohamed Bourham

Gary E. Mitchell,
Co-chair of Advisory Committee

John F. Shriner, Jr.,
Co-chair of Advisory Committee

Dedication

To my wonderful parents Angus and Kay, my beautiful wife Valerie and my source of infinite joy, Elliott Orion. You all exceed my expectations and worth.

Biography

Personal

Morgan Stuart Lance Kent McLean

Born: February 3, 1967, Newport, Rhode Island

Education

University of North Carolina at Wilmington, Bachelor of Science, 1994

North Carolina State University, Master of Science, Physics, 1998

Academic Positions Held

Teaching Assistant, NCSU, 1994-1997

Teaching Assistant, North Carolina Central University, 1997

Research Assistant, TUNL, Duke University, 1997-2004

Physics Instructor, Lenoir Community College, Kinston, NC, 2003

Awards

Walter P. Schmid Award for Excellence in Physics, UNCW, 1994

NCSU Outstanding Teaching Assistant Award, 1995

Memberships

American Physical Society

ΠME National Mathematics Honor Fraternity

American Association of Physics Teachers

Acknowledgements

I have been truly fortunate to have been a part of the TUNL-HRL group. I owe a debt of gratitude to Dr. Gary Mitchell for the opportunities and support he has so generously provided for me. His direction in my research and thesis preparation have been invaluable and I am honored to be a part of his legacy. I am also particularly indebted to Dr. John Shriner. He has served as an excellent pedagogue and example of what it means to be a careful and thorough scientist. I especially grateful for his thoughtful and extensive assistance in preparing this thesis. My thanks are also extended to Dr. Mohamed Bourham and Dr. Ronald Tilley for their service on my advisory committee. I thank all of my committee members for their advice, patience and encouragement.

This work was made possible in large part by the outstanding TUNL technical staff. Chief among this talented group is the incomparable Chris Westerfeldt whose engineering prowess and good humor are surpassed only by his dedication to his family. He is a role model for us all. Special thanks are also extended to Richard O'Quinn, Paul Carter and John Dunham for their outstanding efforts towards keeping our laboratory running. Thanks also to Sidney Edwards, Patrick Mulkey, Bret Carlin and Alex Crowell for their superb work maintaining the computer and electronics systems. It has been a pleasure to work with such a skilled and congenial group of people.

Sincere thanks to Dr. Daniel McDevitt for his hard work and dedication during the experiments. Thanks to Dr. Undraa Agvaanluvsan and Dashdorj Dugersuren for their assistance and inspiration. Thanks also to Dr. Sharon Stephenson, Dr. Bret Crawford, Dr. Paul Wallace and Dr. Gerry Vavrina for serving as mentors and friends.

I am blessed to have made some fantastic friends during my time at NCSU and TUNL. These very special people deserve special thanks. I thank Dr. Chris Grossmann for introducing me to the HRL research group. I give him still greater thanks for being such an outstanding colleague and for his unsurpassed friendship. My profound gratitude is extended to Dr. Bill Beal for his many sacrifices and efforts for the sake of my research. I doubt I will ever meet another person with whom I am more in phase on as many wavelengths than Bill. Special thanks are also due to Dr. Stephen Lokitz for his dedication, his boundless good humor and for many convivial and thought-provoking discussions. Special thanks also to Dr. Carrie Rowland for her collaboration and companionship in the lab, gym and coffee shop.

Thanks to my parents Angus and Kay for their for their enduring devotion, love, and support. The greatest thanks are owed to my wife Valerie for her abiding love and sustenance and for believing in me no matter what.

Contents

List of Tables

List of Figures

Chapter 1

Introduction

An important approach to the understanding of spectra of quantum systems is the examination of their average properties. In nuclear physics, such average properties as the level density and strength function have a wide range of applications, including radioactive beam production, stellar nucleosynthesis, the exploration of exotic nuclei and nuclear reactions in general.

Precise determination of the average properties is extremely sensitive to the data quality. To evaluate the quality of a set of nuclear energy levels, it is useful to sort them into sequences that are identified according to the good quantum numbers of the system; in this work these quantum numbers are the total angular momentum J and parity π. Such sequences can then be tested for completeness and purity. A complete sequence is one that has no missing levels. A pure sequence is one that has no misassigned quantum numbers. The establishment of nearly pure and complete level sequences for the purpose of more accurate evaluation of level densities has been the recent focus of the High Resolution Laboratory (HRL) of the Triangle Universities Nuclear Laboratory (TUNL) in Durham, NC.

The ^{52}Cr(p,p$_0$) and ^{52}Cr(p,p$_1$) reactions have been studied previously [Mos71,

Oza85, Wyl71]. The previous work focused primarily on the examination of the structure of the isobaric analog states; no cross-section measurements were made for inelastic channels below $E_p \approx 3.2$ MeV. Recently, however, improvements have been made in the HRL control systems, computational facilities, and analytical methods. It was expected that with the improved system the ^{52}Cr(p,p$_1$) channel may be observable at a considerably lower energy than in previous work. Therefore, it seemed worthwhile to reexamine the proton resonances in ^{53}Mn with the goal of improving on the previous measurements.

The experiment described in the current work measured the differential cross-section for the ^{52}Cr(p,p$_0$)^{52}Cr and ^{52}Cr(p,p$_1$) ^{52}Cr reactions over the energy ranges E_p = 2.1039-3.4711 MeV and 2.6101-3.4711 MeV respectively. Data were collected at five angles simultaneously. Targets of 1.2-1.5 μg/cm^2 thickness were fabricated using chromium enriched to 99.74% ^{52}Cr. The measurements were performed using the modified KN-3000 Van de Graaff accelerator in the HRL. Yield curves were generated, and the resonance parameters for each of the observed resonances were determined using the multi-level, multi-channel, R-Matrix code MULTI6. The levels were sorted into sequences according to J^π values. The results are both a quantitative and qualitative improvement on the previous work. The level sequences were evaluated for purity and completeness, and the strength functions and level densities were determined.

This work consists of five chapters and three appendices. Chapter 2 discusses the experimental apparatus and methods. Chapter 3 outlines the process of generating the level sequences from the cross-section measurements and includes a brief overview of the R-matrix formalism. Chapter 4 is devoted to the analytical methods and results of the statistical tests. A short introduction to the relevant statistical theory is given, followed by determination of the strength functions and level densities.

A summary of the current work and the results is given in Chapter 5.

There are three appendices. Appendix A displays the data and fits for the ^{52}Cr(p,p$_0$) and ^{52}Cr(p,p$_1$) reactions. The tabulated resonance parameters are presented in Appendix B, first as a comprehensive listing and then as individual level sequences. The results of unfolding the energy dependence of the level densities are illustrated in Appendix C.

Chapter 2

Experimental Setup and Procedure

This chapter describes the laboratory apparatus and the methods used to generate the high quality data in the current work. The accelerator housed in the TUNL HRL is a modified High Voltage model KN-3000 and is described in section 2.1. The differential cross-section measurements are discussed in section 2.2. Preparation of the thin, chemically clean targets which are a necessity for high resolution experiments is described in section 2.3. The TUNL HRL employs several feedback and control loops that are explained in section 2.4. The data acquisition system is discussed in section 2.5. Finally, the automation of the data acquisition process is outlined in section 2.6.

2.1 KN Van de Graaff Accelerator

The TUNL-HRL houses a horizontally mounted KN-3000 Van de Graaff positive ion accelerator. Figure 2.1 is a schematic representation of the main accelerator components. Originally constructed with a 3 MV maximum terminal voltage, it has been upgraded to operate up to 4 MV. At the base of the accelerator, a 50-kV power supply delivers charge to a charging screen, which is in contact with a charging belt

that runs the length of the accelerator column. The belt conveys charge up the column to a collector screen that is connected to the terminal assembly. Charge accumulates on the dome which encases the terminal. The conveyor roller at the terminal end contains an alternator which powers the terminal.

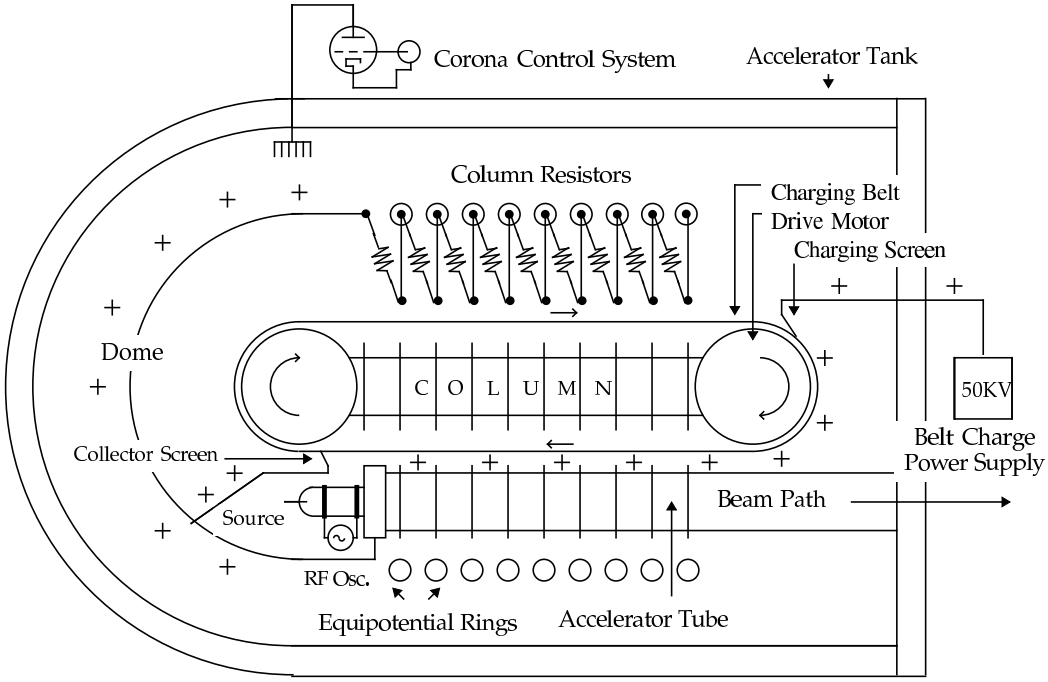

Figure 2.1: The TUNL HRL KN-3000 Van de Graaff accelerator.

The source is fed by any one of three adjacent gas storage bottles and is capable of ionizing H_2, D_2, or He. For the current work research grade H_2 was used. When the oscillator circuit is energized, an RF field is established and is coupled to the source bottle via a pair of wave guides. A standing RF wave is then generated within the bottle as the neutral gas is slowly fed in. Ionization of the gas occurs within the RF field, creating two species of positive ions, H^+ (protons) and $H_2{}^+$. Electrodes mounted at either end of the source produce a longitudinal electric field

which is used to extract the ion beam(s). Although the ion source can produce up to 1 mA of current, only $\sim$40 μA of output is required for a typical experiment. A focus electrode immediately outside the source allows the divergence of the emitted beam to be controlled as it enters the accelerator tube. After they have exited the source, the ion beams are driven down the tube by the accelerating field. A diffusion pump in conjunction with a liquid N_2 trap achieves a vacuum of $\lesssim 1$ μTorr inside the tube.

Charge flows back down the column to ground through a series of 69 high precision 600 MΩ resistors. Connecting each pair of resistors is an aluminum ring which encircles the column. The rings form equipotential planes and provide a step-wise field gradient along the accelerator tube that reduces unwanted divergence in the accelerated beams. The accelerator tube, column assembly, and terminal are all contained within a pressurized tank which is filled with a mixture of CO_2 and N_2 in concentrations of 20% and 80%, respectively. This buffer gas mixture prevents the electrical breakdown within the tank. It is essential that the buffer gas be kept dry (H_2O concentration < 40 ppm by volume) and the interior of the tank free of debris, as even the smallest of impurities can lead to unwanted discharges, so called "tank sparks." For the current experiment the tank was typically pressurized to $\sim$285 psi.

As they exit the base end of the accelerator tube, the accelerated ions encounter a set of electrostatic steerers which center the beam in the analyzing magnet. The beams are separated within the magnetic field due to the differing momenta of the ionic species. The vertically oriented magnetic field steers each beam to the left relative to the incident beam direction. The proton beam is deflected 25° and travels down the experimental leg of the beamline and on to the scattering chamber. The $H_2{}^+$ beam is deflected 17° and travels into the Electrostatic Analyzer (ESA) where it is used in the feedback loops that provide for improved beam energy resolution. An overhead schematic view of the beamlines is shown in Figure 2.2.

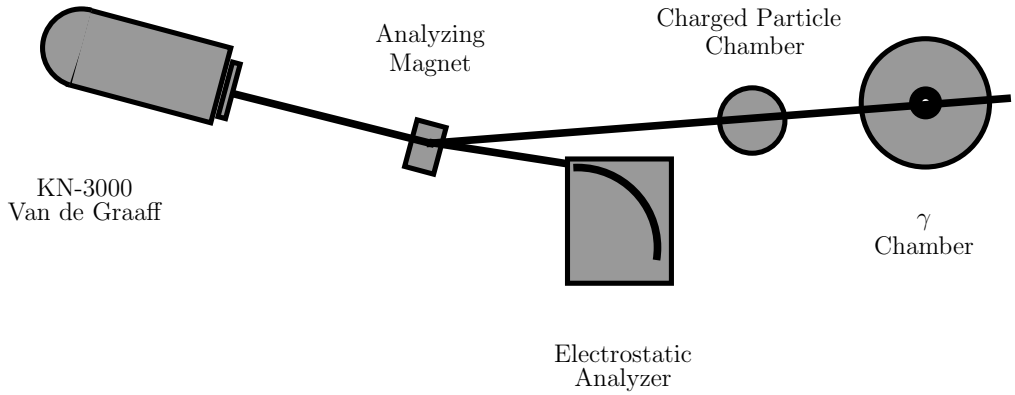

Figure 2.2: High Resolution Laboratory schematic.

2.2 Scattering Chamber and Detectors

After separation from the molecular beam in the analyzing magnet, the proton beam passes through electromagnetic steering and focusing elements. The accelerator operator adjusts (tunes) the various magnetic fields in order to maximize beam transport to the target. Prior to entering the scattering chamber, which is illustrated in Figure 2.3, the beam passes through a water-cooled collimator which produces a small, well-centered beam spot on the target surface. Inside the chamber, a target ladder holds up to four targets. This allows for the replacement of failed targets without frequent removal of the target ladder from the evacuated chamber. The target ladder also holds a tuning ring. Current is measured on the downstream collimator aperture, the tuning ring, and the Faraday cup (beam dump) which lies downstream from the chamber. Beam tunes of $\sim$5 μA of transmitted beam (beam on target) with $\sim$20 nA and $\sim$5 nA on the tuning ring and collimator, respectively, were typical for this experiment. For the current work, a diffusion pump was used in conjunction with a liquid N_2 trap to maintain a vacuum of $\lesssim$1 μTorr in the chamber. Five silicon

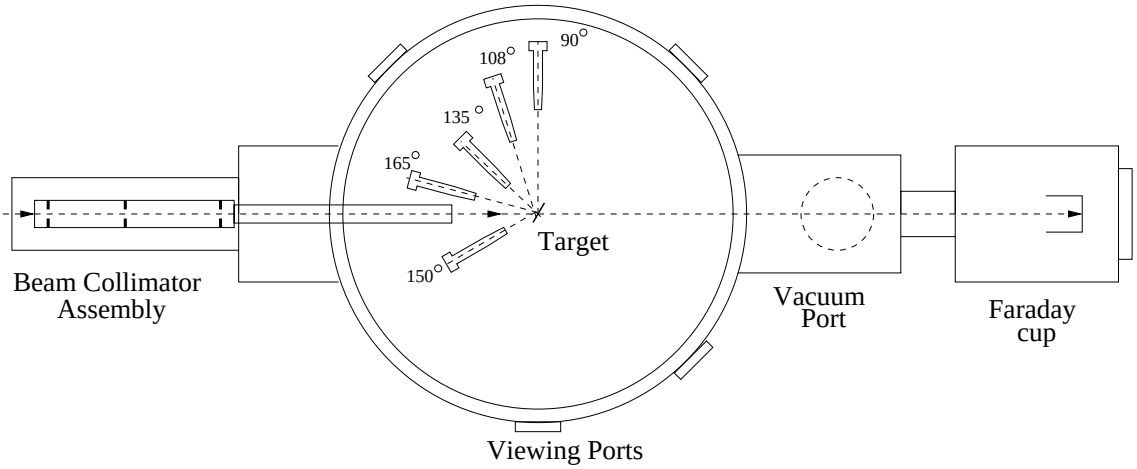

Figure 2.3: Overhead view of proton scattering chamber and detectors.

surface barrier (SSB) detectors with active layers 300 microns thick were mounted inside the chamber. The detectors require a +125 V bias and have typical resolution of 10-20 keV FWHM as measured via the ^{27}Al(p,p) reaction at E_p = 1.47 MeV. The detectors are placed at angles of 90°, 108°, 135°, 150° and 165° with respect to the beam direction. The detectors are mounted on aluminum pedestals and are fitted with snouts that feature collimators and suppression magnets for elimination of unwanted noise from backscattered electrons. The solid angles are chosen to provide approximately equivalent counting rates at all angles for Coulomb scattering, which is the predominant scattering mechanism. Table 2.1 lists the solid angle for each detector.

2.3 Targetry

Targets were prepared using the evaporator configuration illustrated in Figure 2.4. Thin carbon foils with areal densities of 2-5 μg/cm^2 were floated onto stainless steel target rings in a distilled water bath. After drying, the target rings were placed

Table 2.1: The charged-particle detector solid angles used in these measurements.

Detector Angle (degrees)	Solid Angle (msr)
90	0.53
108	0.90
135	1.54
150	1.84
165	2.04

in the evaporator. Chromium metal powder enriched to 99.74% ^{52}Cr was placed in an open 0.05 inch thick tungsten boat. The ends of the boat were clamped between high current electrodes. The boat was covered with a movable shutter. A base vacuum of $\lesssim$1 μTorr was kept in the evaporator via a diffusion pump and liquid N_2 trap. After the chamber was evacuated, the power supply was activated and the current increased over the course of three minutes. The shutter remained closed during this time. Slowly raising the current allowed the boat and sample to outgas with minimum impact on the vacuum. Once the current had reached $\sim$250 A, outgassing was complete and evaporation of the sample had begun. Then the shutter was opened for 90 seconds to allow chromium deposition on the carbon foils. The shutter was then closed and the current reduced to zero. This method produced targets with a ^{52}Cr areal density of 1.5 μg/cm^2. Although results varied from batch to batch, most spectra obtained from targets prepared in this manner had negligible contaminant peaks. The associated energy loss in these targets was $\sim$100 eV.

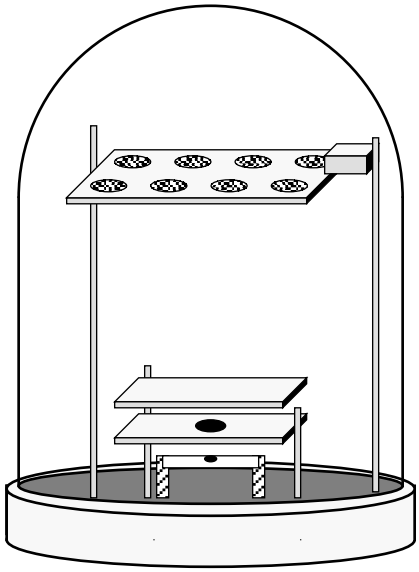

Figure 2.4: The TUNL evaporator system.

2.4 Control Systems

The HRL Van de Graaff accelerator is of the traditional design which employs a rubberized cotton belt to convey charge from the charging power supply to the terminal. Such systems are quite robust and capable of producing high beam loads for extended periods of time. They are, however, subject to instabilities in beam energy. In the vast majority of Van de Graaff installations, the standard feedback systems that accompany the accelerators can reliably control the terminal voltage to within 1 kV. Such energy resolution is insufficient if one seeks to obtain the level of precision required for the experiments carried out in the HRL. The TUNL HRL employs several control loops to further improve upon the standard method. In this section we discuss the detailed operation of the four main control systems in the TUNL HRL. Figure 2.5 is a schematic view of the control loops described here. These control loops make extensive use of the PC-based control program LabVIEW. Several

LabVIEW applications have been developed in the HRL. A LabVIEW application is known as a "virtual instrument," or alternatively by the acronym "vi."

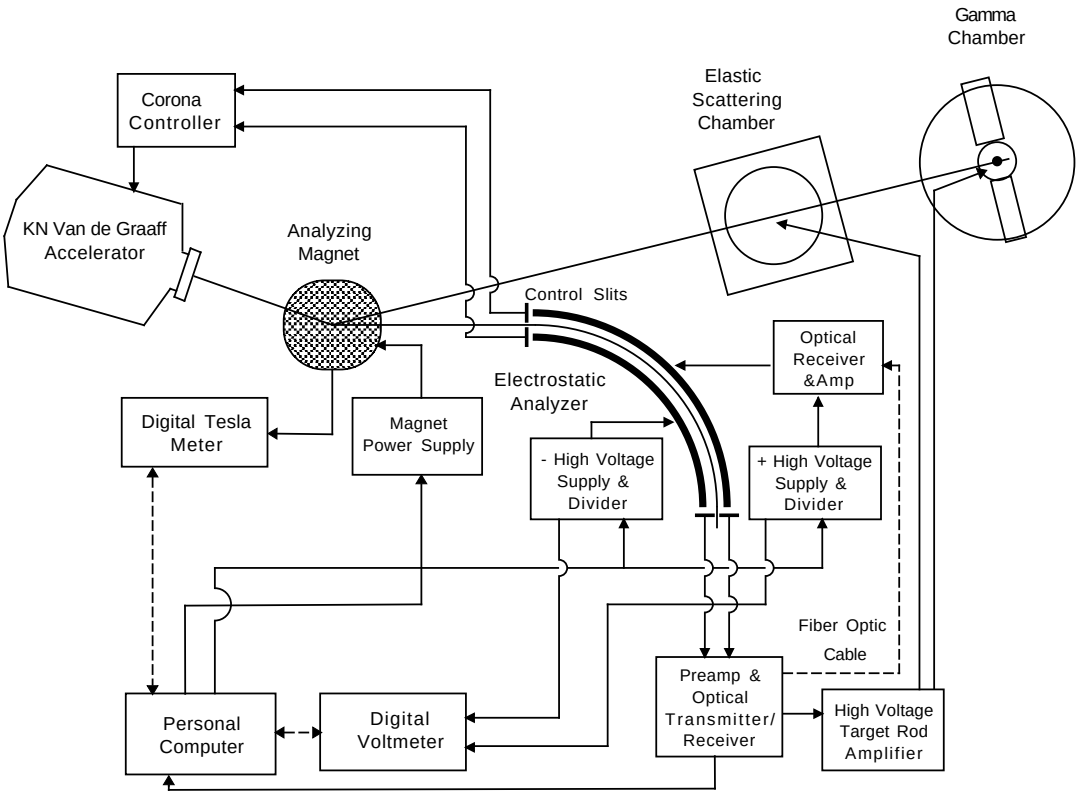

Figure 2.5: The TUNL HRL control loops.

2.4.1 Corona Controller

The implementation of the corona control loop in the TUNL HRL is unique. A corona discharge is maintained within the accelerator tank between the terminal dome and a needle array which is mounted on a movable shaft providing the steep localized field gradients that allow the discharge to occur. The baseline corona load is controlled by varying the distance of the needles from the dome. Fluctuations in beam position are measured at a set of slits mounted on the 17° beamline. Current

signals from the slit pair are sent to a driver amplifier mounted on the exterior of the accelerator tank. The driver amplifier makes adjustments to the corona load until the difference in slit current is minimized. In standard practice, the experimental beam is used to drive the corona feedback circuit. The HRL system instead makes use of the molecular beam for this purpose.

2.4.2 Electrostatic Analyzer

After passing through the corona slits, the molecular beam enters the electrostatic analyzer (ESA). The ESA performs two functions, maintaining the beam within a very narrow energy window and generating a signal that drives the magnet and homogenizer control systems. The ESA consists of a pair of curved steel plates that are connected to highly stable, programmable, high-voltage power supplies of opposite polarity. The geometry of the ESA enclosure dictates that for beam to pass through the center of the ESA, the ratio of the potential difference between the plates V′, and the accelerating potential V must be V/V′=111.37. The ESA control vi accepts the desired beam energy set point signal from the VAX workstation via a PC serial port. The scaling factor is applied, and the resulting digital output is sent through an external digital-to-analog converter (DAC) to the ESA power supplies. As the power supplies are of opposite polarity, only one programming voltage is generated and is sent to both power supplies simultaneously. A digital voltmeter monitors the potential difference between the plates and sends the reading to the PC. The control program then generates a programming signal based on the deviation of the reading from the desired voltage. A data acquisition inhibit signal is generated whenever the measured ESA plate potential difference is found to be outside of the acceptable limits, typically ±31 eV. The molecular beam is shaped by a 0.635-mm wide object

slit aperture at the entrance to the ESA and fully transmitted beam passes through a 0.25-mm wide image slit aperture at the exit. With the proper bias applied to the plates, successful transport of beam through the ESA ensures that the ratio of the error in the actual energy ΔE to the set point energy E is $\Delta E/E \sim 1/5000$. Current is read from each of the image slit plates and fed separately to a preamplifier which generates the error or "slit difference" signal used in the remaining control loops.

2.4.3 Magnet Controller

The magnet control vi has two distinct modes of operation, manual and "slit" mode. The manual mode is the more basic of the two. In manual mode, the operator enters the desired field setting into the PC directly. The vi calculates the appropriate digital output setting which is sent to a custom DAC. The DAC then sends a programming voltage to the magnet power supply. A high-precision Hall probe digital Tesla meter (DTM) reads the resulting field and reports back to the PC via a fiber optic link. (The close proximity of the magnet to the accelerator and its associated transient electrical spikes necessitate the use of optically isolated communication between the PC and DTM.) The vi then calculates and issues the corrected programming signal based on the deviation of the resultant field from the desired field. The loop is executed continually as long as the vi is active. In this mode of operation, the magnet control loop is capable of maintaining the magnetic field to within ± 0.1 G for fields below 6 kG and within ± 0.2 G for fields above 6 kG.

When operated in slit mode, the vi takes periodic readings of the image slit difference signal previously described. The vi is programmed to make adjustments to the field in order to minimize the slit difference signal. Since the sample frequency is $\sim$1 Hz, the magnet is essentially only acting upon the DC component of the slit

difference signal. As adjustments to the field are made by successive iterations of the magnet control loop, small corrections to the terminal will be made by the corona controller, since a change in the magnetic field setting will change the position of the beam on the corona slits. The results of this particular loop are a tight matching of the terminal potential to the magnetic field and a well-centered ESA beam. Operation in slit mode allows the system to compensate automatically for inevitable drift in terminal voltage. It is also crucial to the automation of the incrementation of the beam energy as described in section 2.6.

2.4.4 Homogenizer

The purpose of the homogenizer is to compensate for the fluctuations in the beam energy that remain despite the action of the other control systems. The homogenizer also consists of two distinct subsystems. These subsystems operate independently of the LabVIEW programs. The first of these is the outer plate driver. This system is simply a high-precision bipolar solid state amplifier with an output range from -15 V to +15 V. It takes the image slit difference signal as input and applies the amplified signal on top of the bias applied by the outer plate HV power supply. This requires that the driver amplifier float at the outer plate power supply output voltage. The driver amplifier is therefore located on a platform under the ESA enclosure that is coupled to the outer plate output. A fiber optic link is used to send the slit difference signal to the amplifier and to return a sample of the amplifier output to an oscilloscope. At the beginning of (and periodically throughout) the experiment, the operator adjusts the slit difference preamp gain until the outer plate driver control loop minimizes the slit difference signal as observed on an oscilloscope trace. The ESA beam is then maximally centered, and the resultant slit difference signal is as

true a measurement of the beam energy fluctuations as can be obtained.

The remaining control system, the target rod driver circuit, takes the real time image slit difference signal as input. The target rod driver amplifier has a fixed gain of 111.37, which is, as noted earlier, the proportionality factor between the slit difference signal and the error in proton beam energy. The amplifier drives a +6 kV power supply that is connected to the target rod ladder. The circuit is designed such that the target rod voltage is +3 kV when the slit difference signal is zero and varies between 0 and +6 kV as the signal varies. Floating the target rod in this manner allows the use of a unipolar power supply. The target rod driver thus provides a correction bias in real time that matches the error in beam energy. This system is also equipped with an inhibit signal that can be activated to prevent data acquisition whenever the target rod driver HV power supply is not activated. Periodically, it is necessary to calibrate the high-precision amplifiers to ensure that the 1/111.37 ratio of the slit difference signal to driver output voltages is maintained. The result of the operation of this system is excellent energy resolution. In this experiment, the system resolution was typically ∼280 eV.

2.5 Data Acquisition

The TUNL HRL charged particle data acquisition system is depicted in Figure 2.6. Raw pulses are received from the detectors by Ortec 142 preamplifiers mounted outside the scattering chamber. The preamplifiers send the pulses to Ortec 572 spectroscopy amplifiers in the control room. The unipolar (energy) outputs from the amplifiers are sent to the multiplexer via a 900 nsec delay loop. The delay is necessary to synchronize the arrival of the energy and gate signals at the multiplexer. Each bipolar signal is split and sent to both an Ortec 551 timing single channel analyzer

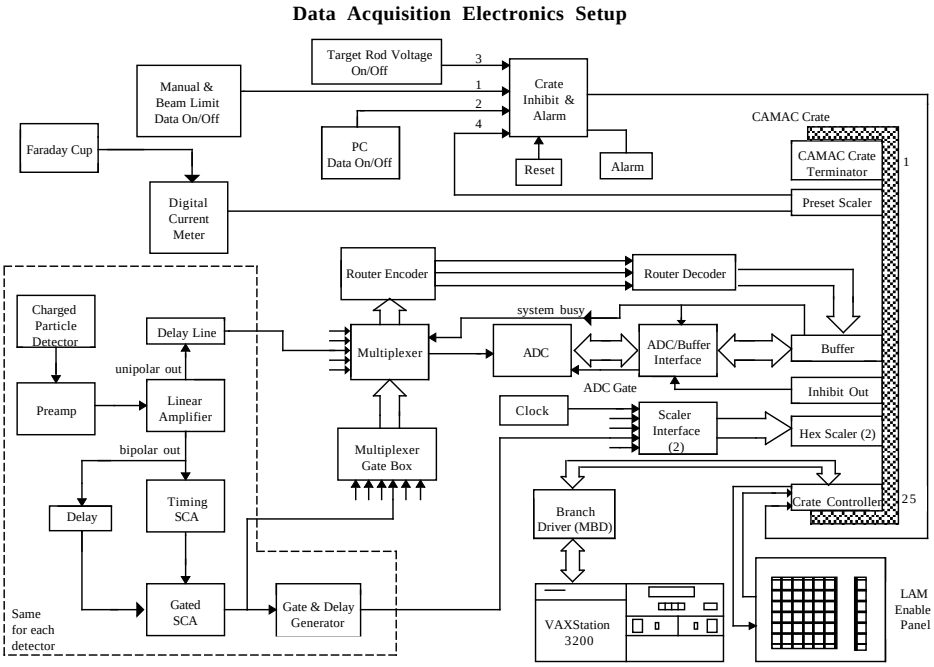

Figure 2.6: The TUNL HRL charged particle data acquisition electronics. The components surrounded by dashed lines are repeated for each of the five detectors.

(TSCA) and, after a 500 nsec delay, a Hewlett-Packard 5583 gated single channel analyzer (SCA). Each TSCA is set to generate signals for peaks that correspond to carbon scattering events. The TSCA outputs are sent to the SCAs which veto the carbon signals and are also used to set upper and lower energy limits. The window is chosen to admit as much spectral data as possible while minimizing the inclusion of both low energy noise and pile-up peaks at the top of the output range. Only signals that fall within the desired energy range and also are not associated with carbon scattering events will generate an output from the SCA. Two gate outputs from the SCA are used in this configuration. The first gate output is sent to the input of the

multiplexer gate interface, and the second gate signal to the scaler interface module via an Ortec 416 gate and delay generator (GDG). The Ortec 416 and 572 have front panel outputs which can be connected to an oscilloscope so that the operator can monitor and adjust carbon event vetoing. With the exception of the pre-amplifiers, all of the signal processing electronics are NIM standard devices. Pulses that produce valid gate signals will trigger the multiplexer gate interface, and energy signals at the corresponding multiplexer inputs will be accepted. The multiplexer passes all events to a Northern 521 analog-to-digital converter (ADC) in a single data stream. The ADC is set to accept data in a 1 - 10 Volt range and convert it to 512 digital channels. The digitized data are sent in a single stream to a CAMAC based buffer module. The multiplexer gate information is passed to the TUNL buffer interface and router encoder which ensure that each event in the data stream is placed in the proper channel in the data buffer. Scaler pulses arrive in a CAMAC based scaler buffer via the custom TUNL scaler interface module.

A crate controller in conjunction with the LAM panel manages data flow across the CAMAC bus. The crate controller handles the I/O while the LAM (literally "Look At Me") enables specific channels on the bus for processing. The crate controller interfaces with the VAX workstation via the microprogrammable branch driver (MBD). Sorting codes are downloaded from the VAX to the MBD. When a module occupying a slot in the CAMAC crate signals that it is ready to send information across the bus and its corresponding LAM coordinates are enabled, the MBD executes the appropriate sorting code. The VAX workstation runs the XSYS data acquisition and analysis package as developed by TUNL [Sod87]. Spectral data, scalers and other parameters are sorted into XSYS data areas. Figure 2.7 shows a typical spectrum from this experiment. The CAMAC crate also contains the scaler module for the beam current integrator (BCI) and the inhibit interface. When the

inhibits are enabled, data acquisition is suspended whenever one of the control systems determines that a system parameter is outside of the acceptable limits or when the CAMAC crate controller needs to read data across the bus. Data acquisition is also inhibited by the BCI preset scaler when it signifies the end of a data run. Data acquisition may also be inhibited manually by the operator as appropriate.

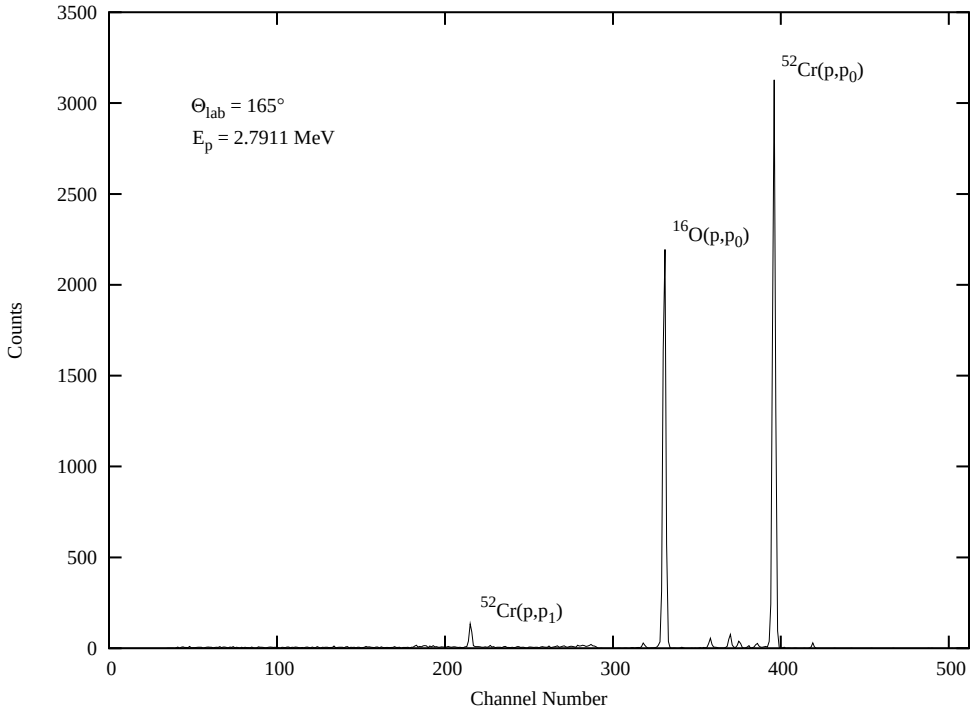

Figure 2.7: A typical p + ^{52}Cr spectrum.

2.6 Data Acquisition Automation

This section explains the process of data acquisition and online yield curve generation in the TUNL HRL and the unique way that the HRL control systems perform rapid machine energy changes between data runs. The accelerator operator initiates the process of generating a yield curve by inputting the starting energy for

the run, the preset amount of BCI required for each data point, and size of the energy increment between points. For the current work, typical BCI presets were 250 - 400 μC with 100 - 400 eV energy increments. Once the machine energy has been set, data collection begins and continues until the BCI preset has been reached. The spectral data accumulate in XSYS data areas and can be viewed during the course of the run. Windows are set around the ^{52}Cr(p,p$_0$) and ^{52}Cr(p,p$_1$) peaks in each spectrum and can be monitored and adjusted during the run. When preset is reached, data collection is inhibited while a VAX subprocess performs several operations. A data file which contains the raw spectral data and various run parameters is written to tape or disk. The VAX then issues the command to increment the beam energy. The counts within the windows are summed, and the sums are stored as data points in separate yield curve data areas. There is a separate yield curve data area for each reaction at each angle. (The yield curve data areas are not automatically written to disk or tape; they can however, be reproduced offline at a later time.) Once the yield curves points have been stored, the VAX clears the spectra and issues the command to begin a new run. This process repeats until the operator intervenes by issuing the HALT command.

Between data runs, the manner is which the control systems respond to the energy change command issued by the VAX is of special importance. The VAX sends a string containing the new energy to the PC. The ESA vi adjusts the plate voltages to reflect the new desired energy. The analyzer beam is then no longer perfectly centered between the exit slits, and the resulting slit difference signal causes the magnet vi to change the field of the analyzing magnet accordingly. This change in the magnetic field then causes the beam to be off-center in the corona slits. The corona control circuit compensates for the offset by shifting the nominal corona current load. In the case of a positive energy step, the corona load decreases, causing the column current

and thus the beam energy to increase. Energy stepping is thus accomplished without the operator having to adjust the machine controls. After many iterations of this process, it is necessary to adjust the belt charge to stabilize the corona, column, and beam currents; this adjustment can be made "on the fly" since the feedback loops will quickly stabilize the system with the new belt charge current. Eventually, however, the process must be halted to allow the operator to retune the beam.

Chapter 3

Determination of Resonance Parameters

The differential cross-section was measured for the ^{52}Cr(p,p$_0$) and ^{52}Cr(p,p$_1$) reactions. Results were obtained for the elastic reaction over the incident proton energy range E_p = 2.1039-3.4711 MeV and for the inelastic reaction over the energy range E_p = 2.6101-3.4711 MeV. Data were obtained for the ^{52}Cr(p,p$_0$) and ^{52}Cr(p,p$_1$) reactions at the angles Θ_{lab} = 90°, 108°, 135°, 159°, and 165°. Excitation functions were generated and the data fit with the multi-level, multi-channel R-matrix code MULTI6. Resonance parameters were obtained for 263 resonances, 62 of which had measurable contributions from the inelastic channel. Section 3.1 provides a brief introduction to the R-matrix formalism which is used to obtain the expression for the cross section that is used by the fitting code. Section 3.2 details the generation of excitation functions including the data reduction and fitting procedure. The absolute energy calibration is explained in Section 3.3. In Section 3.4 the results are summarized and compared to the previous work.

3.1 Reaction Formalism

The proton resonances observed in the current work are best understood in the compound nucleus picture. The widths associated with these resonances are very small in comparison to the widths associated with direct processes such as transfer or knockout reactions. For example, the median s-wave resonance in the current work has an observed width $\Gamma = 305$ eV. This corresponds to a lifetime $\tau = \frac{\hbar}{\Gamma} \sim 2\text{x}10^{-18}$ seconds. The mean nuclear transit time for a proton in the current work is $\sim 2.6\text{x}10^{-22}$ seconds. The mean lifetime of a resonance in this experiment is therefore several orders of magnitude greater than the time it takes for the proton to pass through the region of possible strong nuclear interaction. A similar phenomenon in low-energy neutron scattering prompted Niels Bohr to propose the compound nuclear picture [Boh36].

In the compound nuclear picture, the incident nucleon combines with the target nucleus and the incident nucleon energy is quickly distributed among the constituent nucleons of the compound nucleus. Over the lifetime of the compound system, the nucleus may progress through many intermediate states before a single nucleon (or combination of nucleons such as an α particle) attains sufficient energy to emerge from the nucleus. Furthermore, the evolution of the compound nuclear system is independent of the initial states. Following the initial work of Kapur and Peierls [Kap38], Wigner and Eisenbud formulated an approach to the analysis of compound systems that is independent of the form of the nuclear potential [Wig47]. The following discussion is meant to highlight the main points of the formalism as specifically applied to the reactions observed in the experiment. For a complete treatment of R-matrix theory the reader is referred to the comprehensive review published by Lane and Thomas [Lan58]. The formulation and notation of Lane and Thomas will be

followed as closely as possible.

The most convenient coupling scheme for scattering of unpolarized projectiles by unpolarized targets, such as the ones used in the current work, is known as the channel spin representation. In this representation the projectile spin $\vec{I}_1$ and the target spin $\vec{I}_2$ couple to form the channel spin $\vec{s} = \vec{I}_1 + \vec{I}_2$. The projectile and target spin obey the standard rules for addition of angular momenta. The target, projectile, and channel spins have projections i_1, i_2, and ν respectively. The target and projectile constitute the "entrance" channel from which the compound state is formed. The resulting nuclear state of spin $\vec{J}$ (and projection M) is formed by coupling the channel spin $\vec{s}$ to the relative angular momentum $\vec{\ell}$ of the target and projectile. Channels are given the label c, and particle pairs are denoted by the letter α. A channel c containing a particle pair α is then described by the set $\{\alpha s \ell J M\}$. The compound state may decay through one or more "exit" channels. The exit channels available to the compound state are those which do not violate the conservation of energy or angular momentum. Such channels are referred to as "open", while those that are prohibited are called "closed". A graphical depiction of the channel spin angular momentum coupling scheme as specifically applied to the ^{52}Cr(p,p$_0$) and ^{52}Cr(p,p$_1$) reactions is given in Figure 3.1.

The R-matrix approach makes no attempt to approximate the form of the nuclear potential. Instead, the scattering problem is divided into two regions of interaction. The first of these is the external region where only the Coulomb force acts. The second region is the internal region where the nuclear force (whose form is unknown) is active. The boundary between these two regions is known as the channel radius and is defined as

$$a_c = r_o(A_1^{1/3} + A_2^{1/3}),$$

Elastic scattering

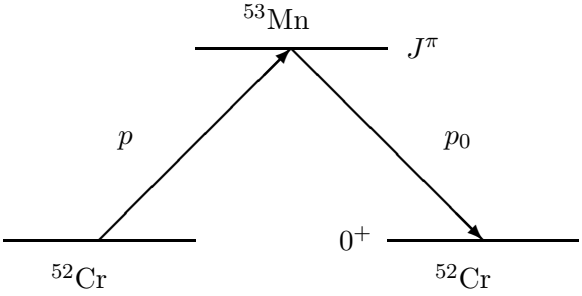

$$\vec{J} = \left(\vec{0} \oplus \vec{\tfrac{1}{2}}\right) \oplus \vec{\ell'}$$

$\vec{\ell} = \vec{\ell'}$ for elastic scattering

$s' = \frac{1}{2}$ only exit channel

Inelastic scattering

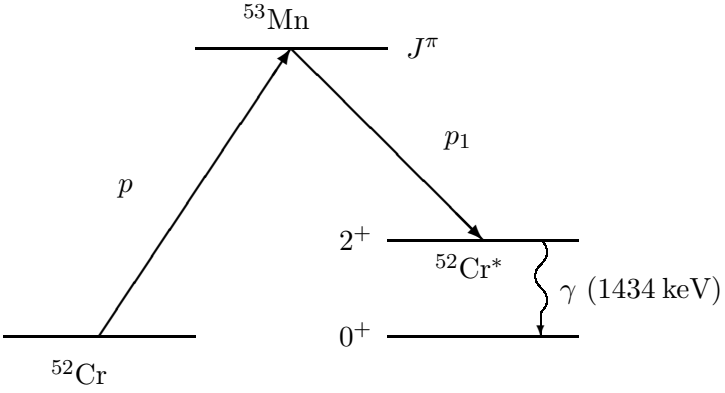

$$\vec{J} = \left(\vec{2} \oplus \vec{\tfrac{1}{2}}\right) \oplus \vec{\ell'}$$

exit channels $s' = \left(\frac{3}{2}, \frac{5}{2}\right)$

various ℓ' for each

Figure 3.1: The channel spin representation and the ^{52}Cr(p,p$_0$) and ^{52}Cr(p,p$_1$) reactions.

where A_1 and A_2 are the masses of the reactants and $r_o = 1.2$ fm. Using the R-matrix method, wave functions of good spin and parity are obtained by solving the Schrödinger equation in the internal and external regions separately. The solutions for the internal and external wave functions are then matched at the channel surface S_c defined by a_c. The result is a solution that can be expressed in a form that is convenient for calculation of the reaction cross section. Some additional convenient definitions are:

$$\begin{aligned}
\text{the reduced mass of the system} \qquad & M_c = M_\alpha = \frac{M_{\alpha_1} M_{\alpha_2}}{M_{\alpha_1} + M_{\alpha_2}}, \\
\text{particle two's position relative to particle one} \qquad & \mathbf{r}_c = \mathbf{r}_\alpha, \\
\text{the energy of the relative motion} \qquad & E_c = E_\alpha, \\
\text{the wave number} \qquad & k_c = k_\alpha = \left[\frac{2M_\alpha E_\alpha}{\hbar^2}\right]^{\frac{1}{2}}, \\
\text{the relative velocity} \qquad & v_c = v_\alpha = \frac{\hbar k_c}{M_c}, \\
\text{the Coulomb field parameter} \qquad & \eta_c = \eta_\alpha = \frac{Z_{\alpha_1} Z_{\alpha_2} e^2}{\hbar v_\alpha} \\
\text{the dimensionless radial coordinate} \qquad & \rho_c = \rho_\alpha = k_c r_c
\end{aligned}$$

3.1.1 External Wave functions

In the external region, where only the Coulomb force is present, the Schrödinger equation $H\Psi = E\Psi$ can be solved exactly. In the center of mass frame the Schrödinger equation can be written

$$(-\frac{\hbar^2}{2M_\alpha}\nabla^2_{r_\alpha} + \frac{Z_{\alpha_1} Z_{\alpha_2} e^2}{r_\alpha} + T^{int}_{\alpha_1} + V^{int}_{\alpha_1} + T^{int}_{\alpha_2} + V^{int}_{\alpha_2})\Psi^{ext} = E\Psi^{ext}, \tag{3.1}$$

where the term T^{int} and V^{int} refer for the internal motion Hamiltonians for the reactants. The solution is separable in terms of the relative motion wavefunction and individual channel wavefunctions and has the form

$$\Psi^{ext} = \chi(\vec{r}_\alpha)\psi_{\alpha_1}(q_{\alpha_1})\psi_{\alpha_2}(q_{\alpha_2}). \tag{3.2}$$

(q_{α_1} and q_{α_2} are the internal coordinates that depend only on the relative position of the particles for the channels α_1 and α_2 .) In the channel spin representation the individual particle wavefunctions are coupled to form

$$\psi_{\alpha s\nu} = \sum_{i_1+i_2=\nu} (I_1 I_2 i_1 i_2 \mid s\nu)\psi_{\alpha_1}(I_1, i_1)\psi_{\alpha_2}(I_2, i_2). \tag{3.3}$$

Further separating the relative motion wavefunction into angular and radial parts gives

$$\chi \sim \left[\frac{\mathrm{i}^\ell Y_\ell^m(\Theta_\alpha, \phi_\alpha)}{r_\alpha}\right] u_{\alpha s\ell}(r_\alpha), \tag{3.4}$$

where $u_{\alpha s\ell}(r_\alpha)$ satisfies the radial equation

$$-\frac{\hbar^2}{2M_\alpha}(\frac{d^2}{dr_\alpha^2} - \frac{\ell(\ell+1)}{r_\alpha^2})u_{\alpha s\ell}(r_\alpha) + (\frac{Z_{\alpha_1} Z_{\alpha_2} e^2}{r_\alpha} - E_\alpha)u_{\alpha s\ell}(r_\alpha) = 0. \tag{3.5}$$

The well-known positive energy solutions to Equation (3.5) are the regular and irregular Coulomb functions $F_c \equiv F_{\alpha_\ell}(\rho_\alpha, \eta_{\alpha\ell})$ and $G_c \equiv G_{\alpha_\ell}(\rho_\alpha, \eta_{\alpha\ell})$. Putting the spatial solutions in the form of incoming and outgoing waves gives

$$I_c^+ = (G_c - \mathrm{i}F_c)e^{\mathrm{i}\omega_c} \qquad \text{and} \qquad O_c^+ = (O_c + \mathrm{i}F_c)e^{-\mathrm{i}\omega_c} \tag{3.6}$$

where

$$\omega_c \equiv \omega_{\alpha\ell} = \sum_{n=1}^{\ell} \tan^{-1}\left(\frac{\eta_\alpha}{\eta}\right). \tag{3.7}$$

The components of the individual wavefunctions for the external region may then be re-combined to form the orthonormal incoming and outgoing channel wavefunctions

$$\mathcal{I}^+_{\alpha s\ell\nu m} = \left(\mathrm{i}^\ell Y^m_\ell\right) \frac{I^+_{\alpha\ell}}{r_\alpha\sqrt{v_\alpha}}\psi_{\alpha s\nu} \qquad \text{and} \qquad \mathcal{O}^+_{\alpha s\ell\nu m} = \left(\mathrm{i}^\ell Y^m_\ell\right) \frac{O^+_{\alpha\ell}}{r_\alpha\sqrt{v_\alpha}}\psi_{\alpha s\nu}. \tag{3.8}$$

The total external wavefunction can then be expressed as

$$\Psi^{ext} = \sum_c \left(x_c\mathcal{O}^+_c + y_c\mathcal{I}^+_c\right). \tag{3.9}$$

The coefficients x_c and y_c are the amplitudes for the outgoing and incoming channel waves respectively. For a specific incident channel c, $y_c = 1$ and the wavefunction can be written

$$\Psi^{ext} = \mathcal{I}_c - \sum_{c'} U_{cc'}y_c \tag{3.10}$$

where the collision matrix $U_{cc'}$ is implicitly defined through the relation

$$x_{c'} = -\sum_c U_{cc'}y_c. \tag{3.11}$$

The elements of $U_{cc'}$ give the amplitudes of the transition probability from channel c to channel c'.

3.1.2 Internal Wavefunctions

In the interior region ($r < a_c$), where the exact form of the Hamiltonian is unknown, a solution to the Schrödinger equation

$$H\Psi^{int} = E\Psi^{int} \tag{3.12}$$

is given by the eigenfunction expansion

$$\Psi^{int} = \sum_{\lambda} A_\lambda X_\lambda \tag{3.13}$$

where the eigenstates X_λ satisfy the relation

$$HX_\lambda = E_\lambda X_\lambda. \tag{3.14}$$

The energy-dependent coefficients are determined by the integral

$$A_\lambda = \int_\tau X_\lambda^* \Psi^{int} d\tau, \tag{3.15}$$

where τ represents the volume bounded by the channel surface S_c. In order to determine the coefficients, the boundary conditions for the wavefunctions on the channel surface must be known.

3.1.3 Boundary Conditions and the R-matrix

In order to specify the boundary conditions, we first express the total external wavefunction as the product

$$\phi_{\alpha s\ell\nu m} u_{\alpha s\ell}(r_\alpha) = \psi^{ext}, \qquad \text{where} \qquad \phi_{\alpha s\ell\nu m} = \left[\frac{\mathrm{i}^\ell Y_\ell^m(\Theta_\alpha, \phi_\alpha)}{r_\alpha}\right] \psi_{\alpha s\nu}. \tag{3.16}$$

The "surface functions" $\phi_{\alpha s \ell \nu m}$ form a complete orthonormal set on the channel surface S_c. The value and derivative of the radial wavefunctions on the channel surface are used to form the quantities

$$V_c = \sqrt{\frac{\hbar^2}{2M_c a_c}} u_c(a_c) \qquad \text{and} \qquad D_c = \sqrt{\frac{a_c \hbar^2}{2M_c}} \left[\frac{du_c}{dr_c}\right]_{r_c = a_c}. \tag{3.17}$$

Writing these quantities as integrals over the channel surface gives

$$V_c = \sqrt{\frac{\hbar^2}{2M_c a_c}} \int_{S_c} \phi_c^* \Psi dS \qquad \text{and} \qquad D_c = V_c + \sqrt{\frac{a_c \hbar^2}{2M_c}} \int_{S_c} \phi_c^* \nabla_n \Psi dS. \tag{3.18}$$

Orthogonality of the surface functions ϕ allows the wavefunction and its derivative to be expressed as

$$\Psi = \sum_n \sqrt{\frac{2M_c a_c}{\hbar^2}} V_c \phi_c \qquad \text{and} \qquad \nabla_n \Psi = \sum_n \sqrt{\frac{2M_c}{a_c \hbar^2}} (D_c - V_c) \phi_c. \tag{3.19}$$

Similarly, performing the surface integrals with the internal wavefunctions X_λ in lieu of Ψ yields the quantities

$$\gamma_{\lambda c} = \sqrt{\frac{\hbar^2}{2M_c a_c}} \int_{S_c} \phi^* X_\lambda dS \qquad \text{and} \qquad \delta_{\lambda c} = \gamma_{\lambda c} + \sqrt{\frac{a_c \hbar^2}{2M_c}} \int_{S_c} \phi^* \nabla_n X_\lambda dS. \tag{3.20}$$

The boundary condition equates the logarithmic derivatives in the internal and external regions and is expressed

$$\frac{D_c}{V_c} = \frac{\delta_{\lambda c}}{\gamma_{\lambda c}} \equiv B_c. \tag{3.21}$$

The energy independent quantity $\gamma_{\lambda c}^2$ is known as the resonance reduced width and has units of energy. For real values of B_c, the value of the eigenfunctions and hence

$\gamma_{\lambda c}^2$ will also be real numbers.

An expression for the coefficients A_λ can be obtained by multiplying Equation 3.12 by X_λ^* and subtracting the complex conjugate of Equation 3.14 and applying Green's Theorem to the result. This results in the expression

$$\begin{aligned}(E - E_\lambda)A_\lambda &= -\frac{\hbar^2}{2M_c}\int_{S_c}(X_\lambda^*\nabla_n\Psi^{int} - \Psi^{int}\nabla_n X_\lambda^*)dS \\ &= \sum_c (D_c - B_c V_c)\gamma_{\lambda c}. \end{aligned} \tag{3.22}$$

Combining this result with Equation 3.13 leads to an expression for the internal wavefunction

$$\Psi^{int} = \sum_c \left[\sum_\lambda \frac{X_\lambda \gamma_{\lambda c}}{E - E_\lambda}\right] D_c. \tag{3.23}$$

Multiplying Equation 3.23 by ϕ_c^* and integrating over the channel surface S_c yields the expression for the boundary value of the total wave function

$$V_{c'} = \sum_c R_{cc'}(D_c - V_c B_c) \qquad \text{where} \qquad R_{cc'} = \sum_\lambda \frac{\gamma_{\lambda c'}\gamma_{\lambda c}}{E_\lambda - E}. \tag{3.24}$$

3.1.4 Differential Cross Sections

In order to obtain an expression for the differential cross section, an expression for the collision matrix elements $U_{cc'}$ in terms of the elements $R_{cc'}$ of the R-matrix is sought. Using Equation 3.9 the quantities V_c and D_c can be expressed in terms of the functions I_c^+ and O_c^+ as

$$V_c = \frac{\hbar}{\sqrt{2}}\left[\rho_c^{-\frac{1}{2}} O_c x_c + \rho_c^{-\frac{1}{2}} I_c y_c\right] \qquad \text{and} \qquad D_c = \frac{\hbar}{\sqrt{2}}\left[\rho_c^{-\frac{1}{2}} O_c' x_c + \rho_c^{-\frac{1}{2}} I_c' y_c\right]. \tag{3.25}$$

Applying the above expressions to Equation 3.24 and comparing the result to Equation 3.11 yields an expression for the collision matrix $\mathbf{U}$ in terms of the R-matrix $\mathbf{R}$

$$\mathbf{U} = \left[\rho^{-\frac{1}{2}}\mathbf{O} - \mathbf{R}\left(\rho^{\frac{1}{2}}\mathbf{O}' - \mathbf{B}\rho^{-\frac{1}{2}}\mathbf{O}\right)\right]^{-1}\left[\rho^{-\frac{1}{2}}\mathbf{I} - \mathbf{R}\left(\rho^{\frac{1}{2}}\mathbf{I}' - \mathbf{B}\rho^{-\frac{1}{2}}\mathbf{I}\right)\right], \tag{3.26}$$

where $\mathbf{B}$. $\mathbf{I}$, and $\mathbf{O}$ are diagonal matrices constructed from the elements defined by Equations 3.21 and 3.6 respectively. The individual elements of the collision matrix are

$$U_{cc'} = e^{\mathrm{i}(\omega_c+\omega_c'-\varphi_c-\varphi_{c'})}\left[\delta_{cc'} + 2\mathrm{i}P_c^{\frac{1}{2}}\frac{1}{1-R_{cc'}L_{c'}}R_{cc'}P_{c'}^{\frac{1}{2}}\right] \tag{3.27}$$

where

$$L_c \equiv \left[\rho_c\frac{O_c'}{O_c}\right]_{r_c=a_c} - B_c = [S_c - B_c] + \mathrm{i}P_c. \tag{3.28}$$

The penetrability

$$P_c = \left[\frac{\rho_c}{F_c^2+G_c^2}\right]_{r_c=a_c} \tag{3.29}$$

quantifies the extent to which the channel wavefunction penetrates the channel surface. The shift function

$$S_c = \left[\rho_c\frac{F_cF_c' + G_cG_c'}{F_c^2+G_c^2}\right]_{r_c=a_c} \tag{3.30}$$

is related to the difference between the resonance energy and the energy eigenvalue for the compound state. The hard-sphere phase shift is defined as

$$\varphi_c \equiv \tan^{-1}\left(\frac{F_c}{G_c}\right). \tag{3.31}$$

When evaluating the transition probabilities $U_{cc'}$ it is convenient to define the partial laboratory width

$$\Gamma_{\lambda c} = 2P_c\gamma_{\lambda c}^2. \tag{3.32}$$

The reduced widths $\gamma_{\lambda c}^2$ are, however, a more transparent means of quantifying the strength of the coupling between entrance channel and the eigenstates of the compound system since they do not depend on the penetrability P_c.

The expression for the cross section in terms of the elements of the collision matrix **U** as derived by Lane and Thomas is

$$\begin{aligned}\frac{d\sigma_{\alpha s,\alpha' s'}}{d\Omega_{\alpha'}} &= \frac{\pi}{k_\alpha^2}|C_{\alpha'}(\theta_{\alpha'})|^2\delta_{\alpha' s',\alpha s} \\ &+ \frac{1}{k_\alpha^2(2s+1)}\sum_L B_L(\alpha' s',\alpha s)P_L(\cos\theta_{\alpha'}) \\ &+ \frac{\sqrt{\pi}}{k_\alpha^2(2s+1)}\sum_{J\ell}(2J+1)\delta_{\alpha' s'\ell',\alpha s\ell}Re[iT^J_{\alpha' s'\ell',\alpha s\ell}]C_{\alpha'}(\theta_{\alpha'})P_\ell(\cos\theta),\end{aligned} \tag{3.33}$$

where

$$\begin{aligned}B_L(\alpha' s',\alpha s) &= \frac{1}{4}(-1)^{(s-s')}\sum_{J_1J_2\ell_1\ell_2\ell_1'\ell_2'}\overline{Z}(\ell_1,J_1\ell_2J_2,sL) \\ &\times \overline{Z}(\ell_1',J_1\ell_2'J_2,s'L)\left(T^{J_1}_{\alpha' s'\ell_1',\alpha s\ell_1}\right)\left(T^{J_2}_{\alpha' s'\ell_2',\alpha s\ell_2}\right)^*,\end{aligned} \tag{3.34}$$

$$T^J_{\alpha' s'\ell',\alpha s\ell} = e^{2i\omega_{\alpha'\ell'}}\delta_{\alpha' s'\ell',\alpha s\ell} - U^J_{\alpha' s'\ell',\alpha s\ell}, \tag{3.35}$$

and

$$C_\alpha = \frac{1}{\sqrt{4\pi}}\eta_\alpha\csc^2\left(\frac{\theta_\alpha}{2}\right)e^{-2i\eta_\alpha\log\left[\sin\left(\frac{\theta_\alpha}{2}\right)\right]}. \tag{3.36}$$

In Equation 3.33 the first term denotes pure Coulomb scattering, the second resonant scattering and the third the interference between the first two. For all but elastic scattering, only the second term is present. The $\overline{Z}$ coefficients are the Z coefficients

of Blatt and Biedenharn *et al.* [Bie52] with the phase convention of Huby [Hub54]. The $P_\ell(\cos\theta)$ are the Legendre polynomials with the phase convention of Condon and Shortly [Con51].

Since the current work involved both unpolarized beam and targets, the total differential cross section is obtained by averaging over the possible initial (beam) polarization states and summing over the possible final (ejectile) polarization states. The final result for a given channel is then:

$$\frac{d\sigma_{\alpha,\alpha'}}{d\Omega_{\alpha'}} = \frac{1}{(2I_1+1)(2I_2+1)} \sum_{ss'} \frac{d\sigma_{\alpha,s,\alpha',s'}}{d\Omega_{\alpha'}}. \tag{3.37}$$

3.2 Data Reduction and Fitting Procedure

This section describes the processing of the raw data and extraction of the resonance parameters via the fitting code. Before fitting the data it is necessary to reduce the raw data to the highest quality set. During the experiment, data acquisition may be interrupted for various reasons such as tank sparks, target failure, mechanical difficulties, or the re-examination of a portion of the data. Whenever data acquisition is halted, the operator must retake data from the most recent energy range where significant structure in the yield curves has been observed before proceeding. This ensures that there are no gaps in the energy range of the data. The raw data therefore consists of many overlapping segments of various lengths that are stored on disk and tape for offline analysis.

The data segments are evaluated individually for quality. The XDISKREAD program allows yield curves to be regenerated offline on a segment by segment basis. This process is referred to as "stripping". The spectral window boundaries, background subtraction, and calibration parameters all can be adjusted as needed during

the stripping process. Great care was taken in the stripping process to minimize apparent fluctuations in the yield that are not due to variations in the cross-section. If a segment shows no obvious anomalies or discontinuities, it becomes a candidate for use in the final data set. Once the candidate segments are chosen, a best set is chosen which, when properly spliced together, spans the entire range of E_p for the experiment. Of the approximately 200 segments contained in the raw data set, 78 were used to perform the analysis. Once the data has been stripped and the best set of segments identified, the segments are fitted individually. Since the statistical analysis is sensitive to the spacings between the levels, great care must go into joining the overlapping segments to form the final data set. Often the event that caused data acquisition to be halted during the experiment is associated with a shift in the observed E_p. Therefore, as the segments are fitted, the energy shifts must be noted. Starting with the second segment that is to be fitted, the observed energy shift relative to the last segment used is entered into its corresponding MULTI6 input file. MULTI6 adjusts the output to compensate for the observed energy shift. The result is a set of fitted segments that is self-consistent with respect to energy.

Fitting of each data segment proceeds from an initial set of trial parameters for each resonance that are refined over successive runs of MULTI6. MULTI6 uses the expression for the cross section given by Equation 3.33 to calculate the cross section based on the input parameters. The variable resonance parameters consist of the resonance energy E, the total angular momentum J, the parity π, the laboratory width Γ_p or $\Gamma_{p'}$ (for the elastic and inelastic channels respectively), the channel spin s' and the exit channel relative angular momentum ℓ'. (Quantities such as nuclear mass, charge, and channel radius whose values do not change from resonance to resonance are also included in the MULTI6 input files.) The rules for addition of angular momenta constrain the choices for J, s' and ℓ'. The observed angular momentum

combinations are summarized in Table 3.1. (Though the rules for angular momentum coupling allow for some higher ℓ' values than those listed, they were not used in fitting the data as they lead to anomalously large reduced widths for the energy range covered.) The observed resonance shapes are compared to the theoretical shapes generated by MULTI6 and the parameters are adjusted until, by visual inspection, the calculated shape matches the data as closely as possible. Sample shapes for the ^{52}Cr(p,p$_0$) reaction cross sections are shown in Figure 3.2.

Although the general shapes for the ^{52}Cr(p,p$_1$) reaction cross sections are the same for all angles and choices of angular momenta, they may be distinguished by their angular distributions. With the exception of the $J = \frac{1}{2}$ cases (whose angular distributions are isotropic for all values of s' and ℓ') the angular distributions depend upon the values of J^π, s' and ℓ'. Figure 3.3 shows some relevant examples of the angular distributions. As will be shown in the example that follows, these angular distribution are useful tools in removing ambiguities in uncertain J^π assignments. Additionally, the characteristically sharp peaks in the resonance shapes often aid the location of the exact resonance energy.

Another factor that can affect the shapes of the resonances is the energy resolution of the system. Beam energy fluctuations and energy loss in the target inevitably lead to a degradation of the observed shapes from the ideal. MULTI6 convolves a resolution function into the calculated shapes to account for these effects. Several parameters may be adjusted that generate an asymmetric (with respect to energy) smear which is included in the cross section calculation. The greater the smear, the less sharply defined the shapes will be. Each segment may have its own resolution function, but it is common for the resolution function to remain constant over several data segments for a period of time when the experimental system was undisturbed. For the current work, the asymmetric smear was typically between 275 eV and 375

Table 3.1: Summary of angular momentum couplings for the observed values of J^π.

J^π	channel	channel spin s'	ℓ'
$\frac{1}{2}^+$	p_0	$\frac{1}{2}$	0
	p_1	$\frac{3}{2}$	2
		$\frac{5}{2}$	2
$\frac{1}{2}^-$	p_0	$\frac{1}{2}$	1
	p_1	$\frac{3}{2}$	1
		$\frac{5}{2}$	3
$\frac{3}{2}^-$	p_0	$\frac{1}{2}$	1
	p_1	$\frac{3}{2}$	1,3
		$\frac{5}{2}$	1,3
$\frac{3}{2}^+$	p_0	$\frac{1}{2}$	2
	p_1	$\frac{3}{2}$	0,2
		$\frac{5}{2}$	2
$\frac{5}{2}^+$	p_0	$\frac{1}{2}$	2
	p_1	$\frac{3}{2}$	2
		$\frac{5}{2}$	0,2
$\frac{5}{2}^-$	p_0	$\frac{1}{2}$	3
	p_1	$\frac{3}{2}$	1,3
		$\frac{5}{2}$	1,3
$\frac{7}{2}^-$	p_0	$\frac{1}{2}$	3
	p_1	$\frac{3}{2}$	3
		$\frac{5}{2}$	1,3

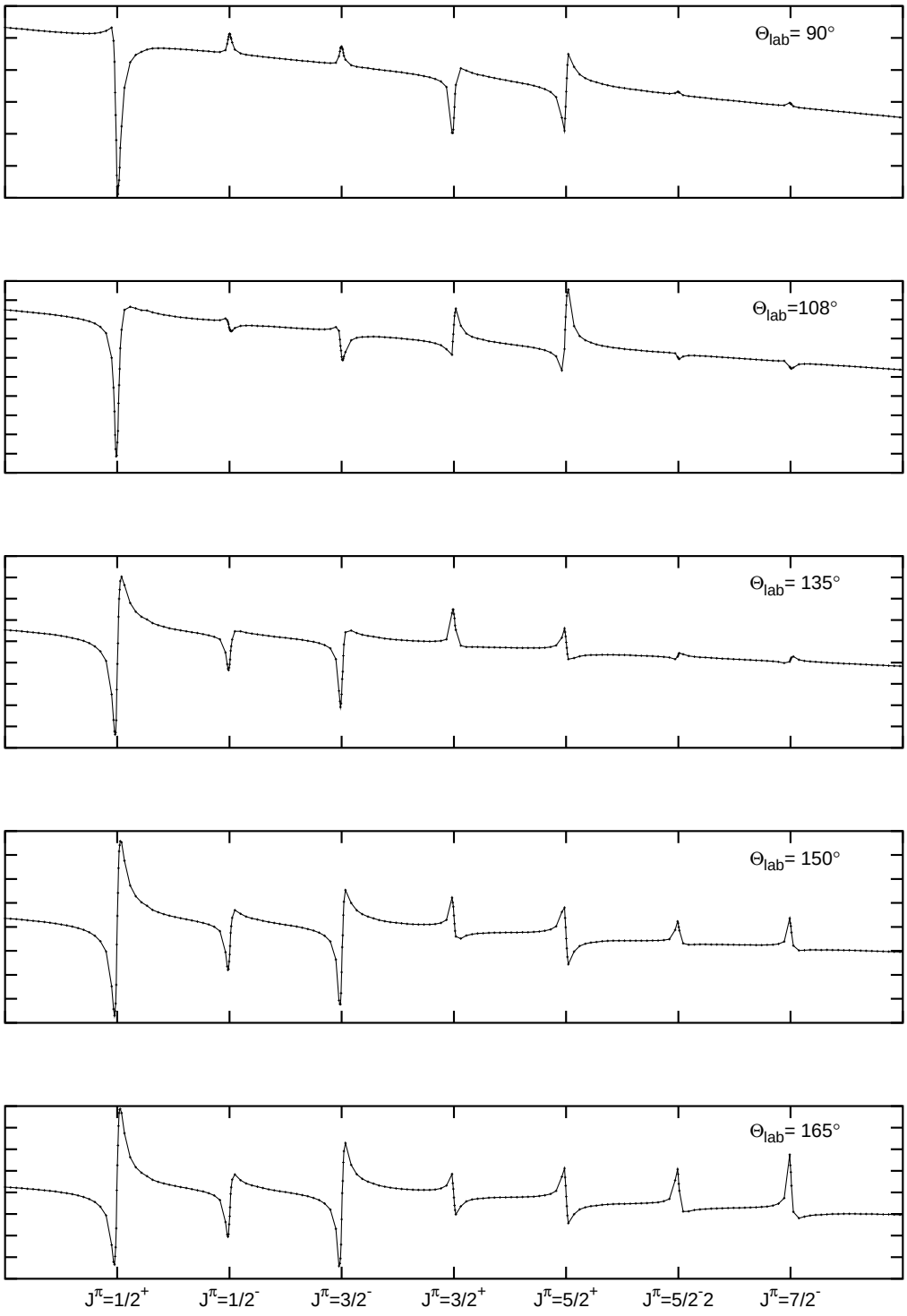

Figure 3.2: Sample resonance shapes for the ^{52}Cr(p,p$_0$) reaction. The scale and strengths have been chosen to illustrate the shapes typically observed.

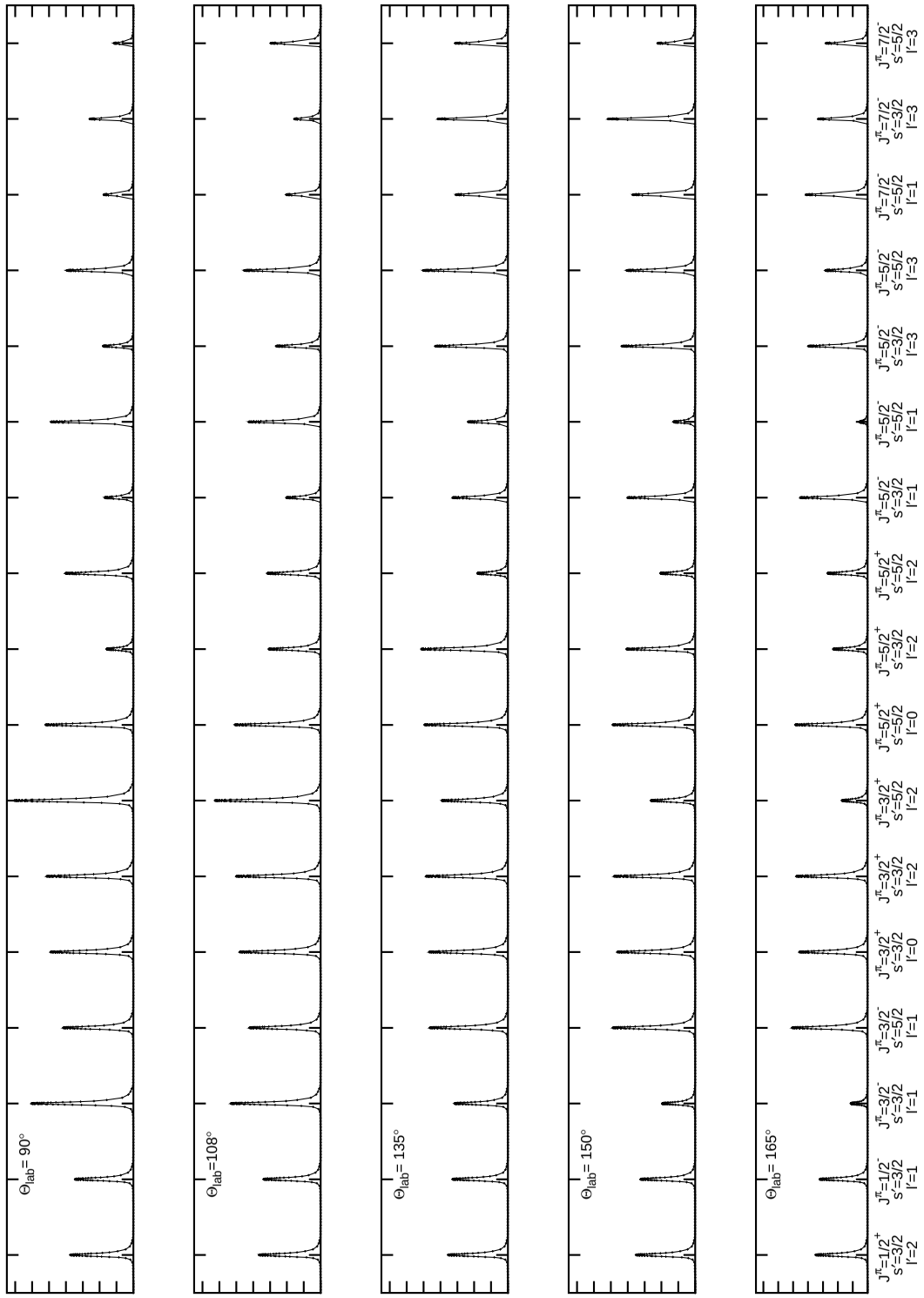

Figure 3.3: Sample angular distributions for the ^{52}Cr(p,p$_1$) reaction. The scale and widths have been chosen to facilitate comparison of the distributions.

eV. It is this quantity that is quoted as the energy resolution of the system.

A resonance shape is best fit when the resonance is well isolated and has a large width Γ_p. However, the strength of the TUNL-HRL system is that it enables the measurement of resonances which may be small and/or overlapping. Fitting such resonance shapes presents a challenge. Where the inelastic channel results are inconclusive, ambiguities may remain in the J^π assignments even after the fits have been refined as much as possible. In the current work this is often the case when attempting to make assignments for $\ell = 2$ resonances. Below approximately $\Gamma_p \approx$ 35 eV the $\frac{3}{2}^+$ and $\frac{5}{2}^+$ resonance shapes are nearly indistinguishable. For this reason, many of the $\ell = 2$ assignments must be considered tentative. The situation is similar for the $\ell = 3$ states. Since none of the $\ell = 3$ resonances observed exhibit conclusive angular distributions in the inelastic channel, their J^π assignments remain ambiguous. They have all been given arbitrary $J^\pi = \frac{5}{2}^-$ assignments.

The advantages of the improved resolution of the experimental system and the presence of inelastic scattering data are realized when analyzing the $\ell = 1$ resonances. The similarity between their elastic scattering cross section shapes, makes discerning $J = \frac{1}{2}^-$ from $J = \frac{3}{2}^-$ resonances difficult when the elastic width is small (say $\Gamma_p \leq 50$ eV). However, for inelastic scattering the angular distribution for a $J^\pi = \frac{1}{2}^-$ resonance is usually readily discerned from that of a $J^\pi = \frac{3}{2}^-$ resonance. Many weak resonances that were previously fit with $J^\pi = \frac{1}{2}^-$ were given new assignments of $J^\pi = \frac{3}{2}^-$ due to the presence of anisotropic angular distributions in the inelastic channel. Figure 3.4 shows a weak resonance that was previously given a $J^\pi = \frac{1}{2}^-$ assignment. The new inelastic channel results show a clear anisotropy in the angular distribution and the assignment was revised to $J^\pi = \frac{3}{2}^-$.

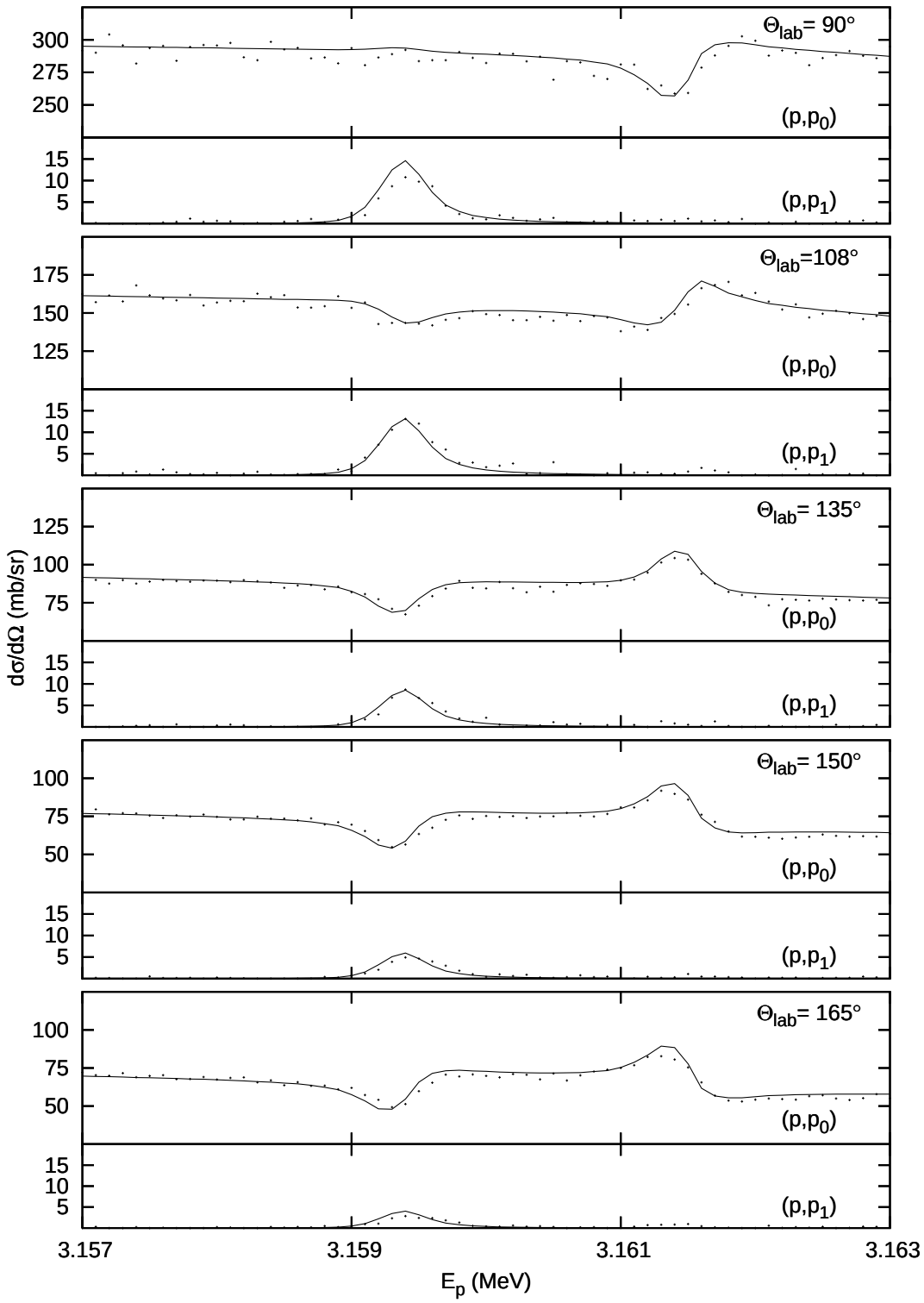

Figure 3.4: The data and fits for the ^{52}Cr(p,p$_0$) and ^{52}Cr(p,p$_1$) reactions for 3.157 MeV $\leq$ E $_p$ $\leq$ 3.163 MeV. The anisotropic angular distribution of the (p,p$_1$) cross sections at E$_p$ = 3.1595 MeV led to the reassignment of the resonance from $\frac{1}{2}^-$ to $\frac{3}{2}^-$.

3.3 Energy Calibration

The data reduction procedure compensates for local shifts in the observed E_p, but it does not address any systematic error in the observed E_p. For the current work two well-established standard resonances were measured and a linear fit to the two calibration points was performed. At the outset of the experiment, immediately before the first of the ^{52}Cr(p,p) data was collected, the low energy calibration point was measured. For this point, the $\frac{1}{2}^+$ resonance at $E_p = 1.8840$ MeV in ^{44}Ca(p,p$_0$) was used. This resonance is an established secondary standard against the ^{7}Li(p,n) threshold which occurs at $E_p = 1.8806$ MeV [Wim74]. In the current work, the ^{44}Ca resonance appeared at $E_p = 1.8795$ MeV. It should be noted that the current data set does not contain any points below 2.1000 MeV, making the choice of the ^{44}Ca resonance less than ideal. Subsequent to completion of the data collection for the entire energy range covered in the experiment, a measurement was made of the $J^\pi = \frac{5}{2}^+$ resonance in the ^{56}Fe(p,p$_0$) reaction which occurs at $E_p = 3.2369$ MeV. It was found at $E_p = 3.2361$ MeV. This resonance is established as a secondary standard to the ^{13}C(p,n) threshold at $E_p = 3.2357$ MeV [Nel83]. Since the ^{56}Fe calibration data were taken after the completion of the ^{52}Cr data collection, a concurrent measurement was made of the nearby $\frac{5}{2}^+$ resonance observed at $E_p = 3.2448$ MeV in the ^{52}Cr(p,p) reaction. It is of interest to note that this resonance was observed at the exact same energy during the calibration run as during the original data collection. Since the difference between the observed E_p and the established resonance energies is relatively small, the calibration results in a relatively small correction.

3.4 Results

A total of 263 resonances were fitted. Of these, 62 had measurable contributions from the inelastic channel. Additionally, 25 reassignments were made. The most common reassignment was the change of a $J^\pi = \frac{1}{2}^-$ resonance to a $J^\pi = \frac{3}{2}^-$ resonance. Table 3.2 gives a comparison of the sequences of resonances observed in the current work to those accounted for by the previous work of Moses and Ozawa [Mos70, Oza85] over the same energy range.

Table 3.2: Number of observed resonances grouped by J^π.

J^π	Previous†		Current	
	(p,p$_0$)	(p,p$_1$)	(p,p$_0$)	(p,p$_1$)
$\frac{1}{2}^+$	50	0	54	2
$\frac{1}{2}^-$	51	0	46	4
$\frac{3}{2}^-$	23	2	49	14
$\frac{3}{2}^+$	21	2	21	4
$\frac{5}{2}^+$	52	6	86	33
$\frac{5}{2}^-, \frac{7}{2}^-$	0	0	7	3
Total	197	10	263	62

†[Mos70, Oza85]

Chapter 4

Analysis of Level Sequences

Level sequences were obtained for the p + ^{52}Cr reactions for $J^\pi = \frac{1}{2}^+, \frac{1}{2}^-, \frac{3}{2}^-$, and $\ell = 2$ for 8624 keV $\lesssim$ E$_x$ $\lesssim$ 9965 keV. Several statistics have been evaluated for each of the sequences. The present chapter contains a brief introduction to the relevant theory, a description of the analytical methods, and presentation of the results. Section 4.1 summarizes the theoretical background. The analysis of the level spacings for each sequence is described in section 4.2. Section 4.3 details the analysis of the reduced width distributions and calculation of the strength functions for each sequence. In section 4.4 the level densities are calculated and the parity dependence examined for $J = \frac{1}{2}$.

4.1 Theoretical Background

The level sequences obtained in the current work are evaluated for completeness and purity by comparing the distributions of the nearest-neighbor spacings and reduced widths to the predictions of random matrix theory (RMT). RMT was first applied to compound nuclear states by Wigner [Wig65]. More recently, the general

theory of random matrices is described by Mehta [Meh91], and a review of the role of RMT in quantum systems is provided by Guhr *et al.* [Guh98]. In RMT, the nuclear Hamiltonian is assumed to be a random variable with probability distribution $P(H)$. The Hamiltonians, H, are assumed real and symmetric. The specific form of $P(H)$ arises from the inclusion of the appropriate symmetries. First, the condition of invariance under transformation of basis vectors is placed on $P(H)$. This relationship is expressed as

$$P(H')dH' = P(H)dH. \tag{4.1}$$

Further imposing rotational symmetry and time-reversal invariance of the compound nuclear system dictates that the Hamiltonians be orthogonal. This implies that

$$H' = OHO^T, \tag{4.2}$$

where O belongs to the orthogonal group $O(N)$. Secondly, the condition that the elements of H are statistically independent is imposed. Thus $P(H)$ is separable. This can be expressed as

$$P(H) = \prod_{i<j} f_{ij}(H_{ij}), \tag{4.3}$$

where the f_{ij} are independently normalized. The resulting distribution has a Gaussian form and can be shown to be

$$P(H) = e^{-a\,\mathrm{tr}(H^2)+b\,\mathrm{tr}(H)+c}, \tag{4.4}$$

where a, b, and c are constants and $\mathrm{tr}(H)$ is the trace of the Hamiltonian. The ensemble of matrices with the above probability distribution is known as the Gaussian Orthogonal Ensemble (GOE). As the dynamic properties of the system are not part

of the construction, no predictions concerning them are given by the theory. Rather, using RMT, it is possible to understand the fluctuation properties of the eigenvalue spectrum. Comparison with GOE statistics can in appropriate cases provide a useful means of assessing a data set for purity and completeness. Purity means that the sequences consist of levels with the same quantum numbers. Completeness means that there are no levels missing.

4.2 Spacing Analysis

The first statistical test performed is the nearest-neighbor spacing distribution (NNSD) analysis. The fluctuations of the level spacings about the mean value for each sequence are examined. First, the exponential dependence of the level densities on energy is unfolded from each sequence. Repeated attempts are then made to correct the sequences for spacings that are anomalously far from average. The resulting spacing distributions are then compared to those of the GOE.

The parameter of interest is the normalized nearest-neighbor level spacing, to which the variable x is assigned. It is defined as

$$x \equiv \frac{S}{D}, \tag{4.5}$$

where S is the difference in energy between two adjacent levels (nearest-neighbors) in a sequence, and D is the mean value of S. For a sequence comprised of N levels, there will thus be $N-1$ values of S and, hence, of x. The assumption that the level spacings within a sequence are uncorrelated leads naturally to a Poisson distribution

for $P(x)$. Such a distribution has the form

$$P_P(x) = e^{-x}. \tag{4.6}$$

Random matrix theory, however, predicts that the probability density function, $P(x)$, has a different form. For the GOE version of random matrix theory, the probability density function is

$$P_{GOE}(x) = \frac{\pi x}{2} e^{-\frac{\pi x^2}{4}}, \tag{4.7}$$

which is known as the Wigner distribution. Comparisons of the two forms for $P(x)$, as well as the probability distribution functions, $F(x)$, are shown in figure 4.1. The characteristic that most clearly distinguishes the two forms of $P(x)$ is their behavior near $x = 0$. For the Poisson distribution $P_P(0) = 1$, whereas for the Wigner distribution $P_{GOE}(0) = 0$. The large x behavior of the Wigner distribution is qualitatively similar to the Poisson. The property of $P_{GOE}(x)$ approaching zero as x approaches zero is known as level repulsion. Comparison of the continuous distributions to the results of the experiment can be performed by plotting the histogrammed data concurrently with the theoretical curves. Even for a sequence that is both pure and complete, agreement with the predictions of RMT is not automatic. RMT assumes a uniform level density, while nuclear energy level densities exhibit an exponential increase with increasing energy. Therefore, before further analysis can be performed, this dependence is unfolded from each sequence via the method described by Shriner *et al.* [Shr90]. This procedure is outlined and the raw and unfolded data presented in Appendix C. The unfolded sequences are used for all of the spacing analyses.

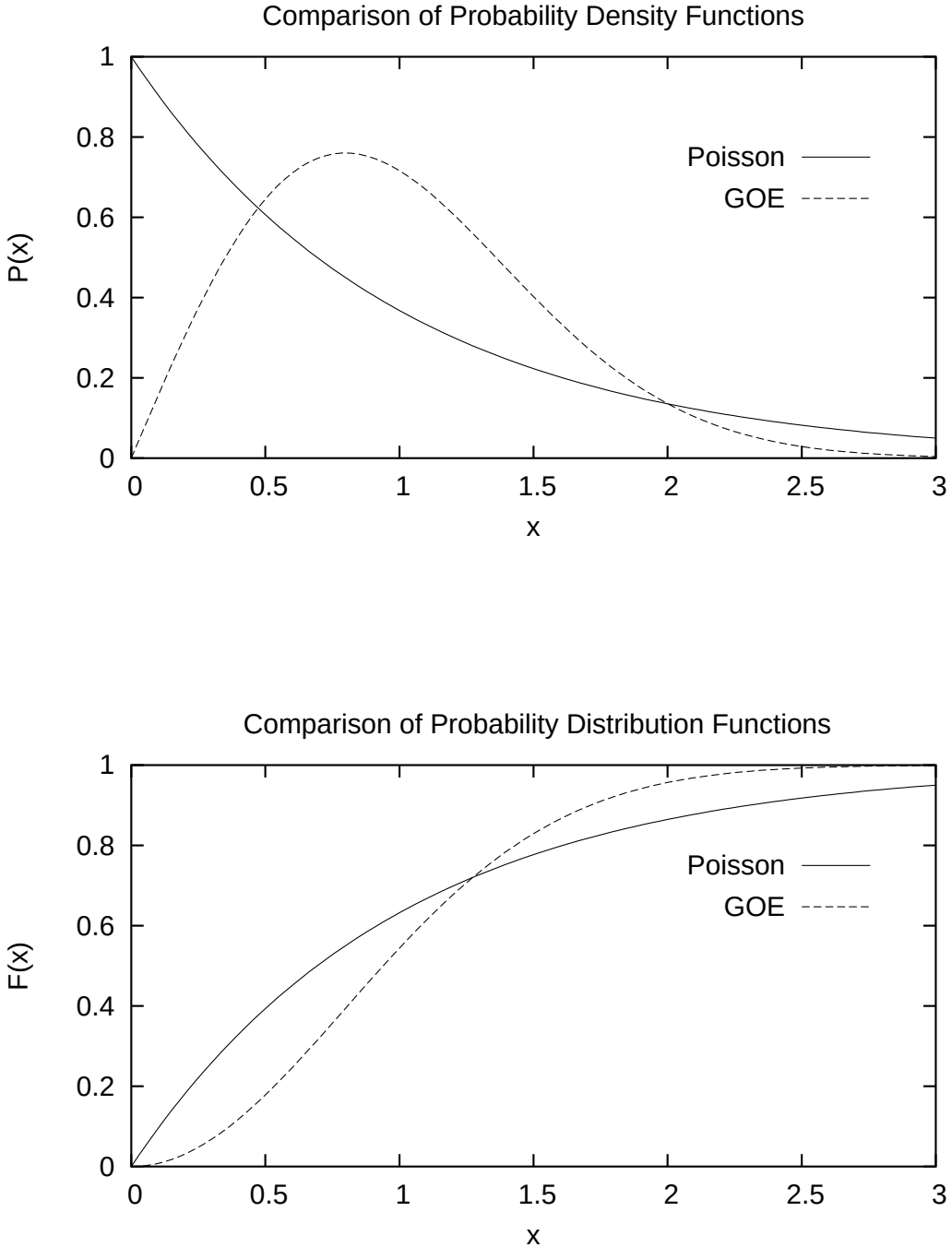

Figure 4.1: The nearest-neighbor spacing probability density function $P(x)$ and probability distribution function F(x) for the Poisson (solid line) and GOE (dashed line) distributions.

4.2.1 Spacing Anomaly Analysis

It is possible to identify specific values of x which may arise from missing or misassigned levels. This involves searching the level sequences for values of x that are so large or so small as to be unlikely given the GOE distribution, so called "spacing anomalies." In some cases, it is possible to remove the anomalous spacings by reexamining the fits to the data and making adjustments to the assignments.

Examination of $F_{GOE}(x)$ shows 98% probablity for $x \leq 2.23$. Therefore, assuming a sequence that is both pure and complete, it is expected that 2% of the x values will be greater than 2.23. Similarly, one expects only 1% of the level spacings in a sequence to have x values greater than 2.42 and only 0.1% of the x values will be above 3.00. These examples are chosen because they make convenient points for evaluation. A scatter plot of the x values reveals spacings that are anomalous. Where a spacing is unexpectedly large, a possible missing level is indicated.

In a similar way, one can determine limits below which x values are unlikely to appear. Examination of $F_{GOE}(x)$ shows that 2% of the spacings will be expected to have $x \leq 0.16$, 1% will have $x \leq 0.11$, and 0.01% will have $x \leq 0.004$. Spacings that are improbably small suggest the presence of levels in the sequence with improper J^{π} assignments. Another more convenient method of visualizing the low-x spacing anomalies is obtained by plotting $\frac{1}{x}$ instead of x. In this case the 2%, 1%, and 0.1% cutoffs become 6.25, 8.84, and 25.0 respectively. Figure 4.2 shows expanded views of the probability distribution function for the Wigner distribution in the low-and high-x regions. The spacing anomaly analysis allows for the identification of specific regions in the experimental data that should be evaluated for missing or misassigned levels. Figures 4.3 - 4.5 show the x and $\frac{1}{x}$ plots for both the previous work of Moses [Mos70] and the current work for each of the J^{π} sequences. (The spacing anomaly

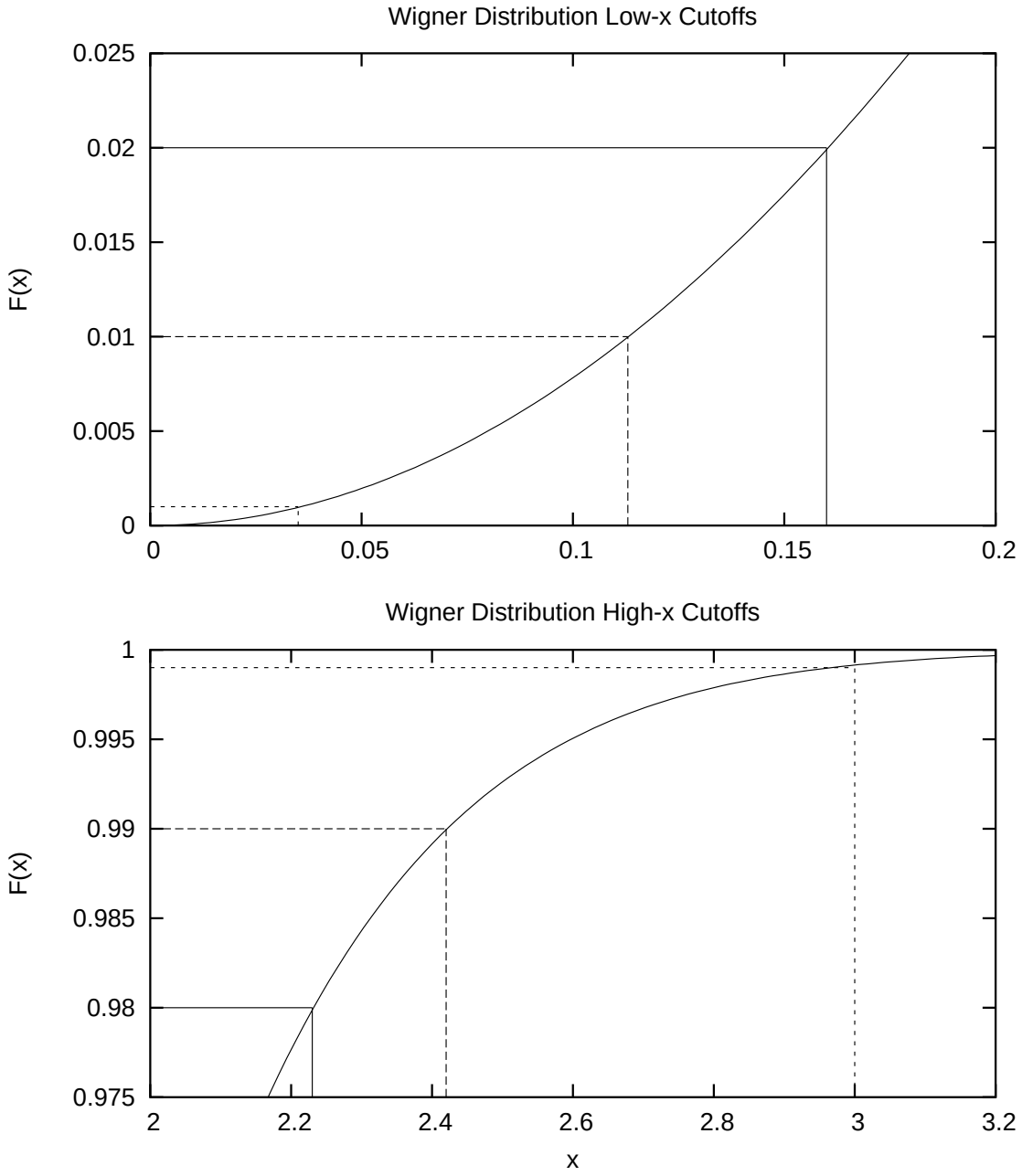

Figure 4.2: Expanded views of the probability distribution function plot for the Wigner distribution. The 2%, 1% and 0.1% cut-off points are given by the solid, dashed and dotted lines respectively. For the upper plot, the cutoffs indicate the percentage of spacings that should lie below the corresponding x value. For the lower plot, the cutoffs indicate the percentage of spacings expected above the cutoffs.

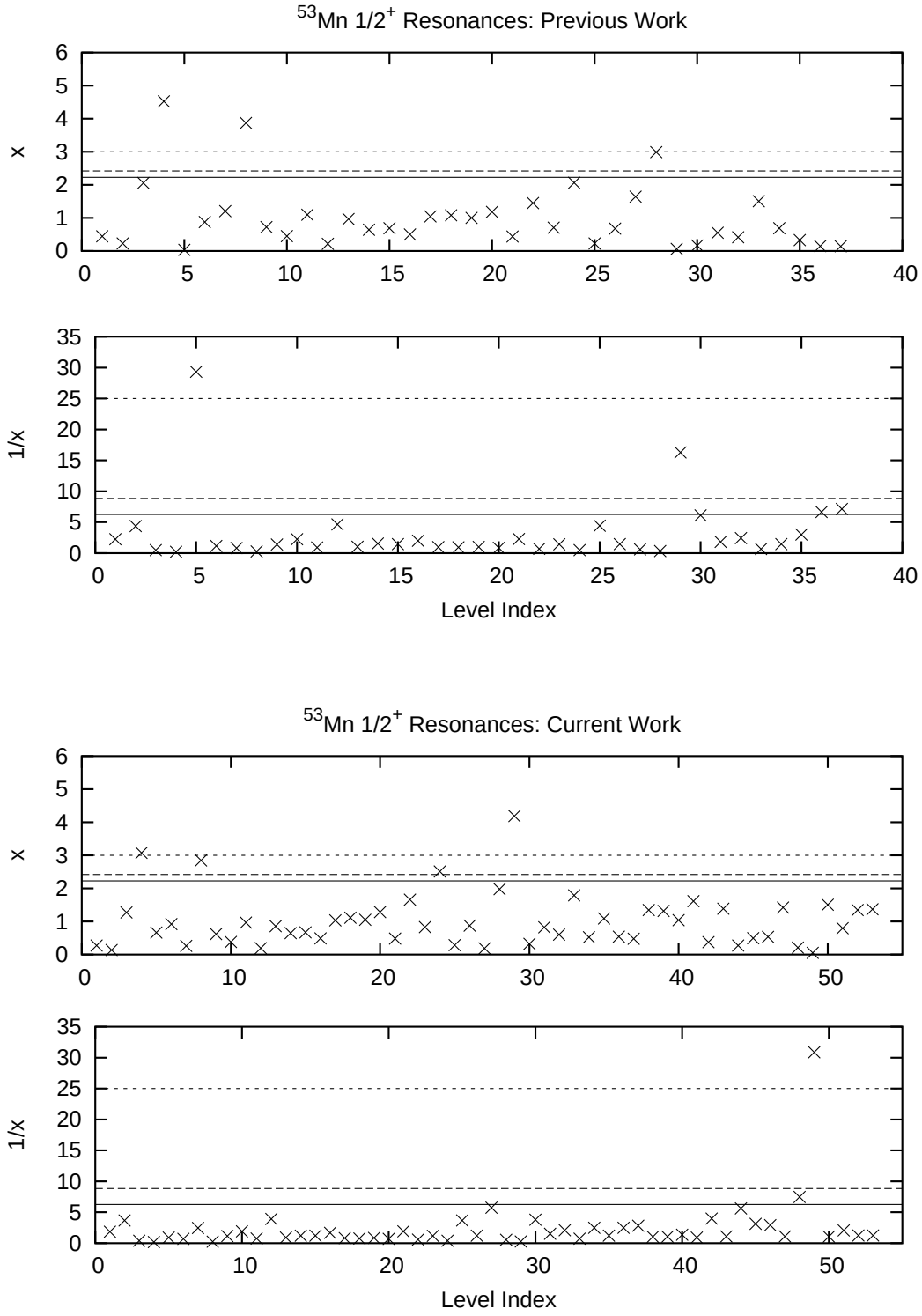

Figure 4.3: The spacing anomaly plots for the $J^\pi = \frac{1}{2}^+$ level sequence obtained from the previous work (top) and current work (bottom). Note the removal of the anomaly, at level index five, in the $\frac{1}{x}$ plots. This results from the correction of a misassigned level.

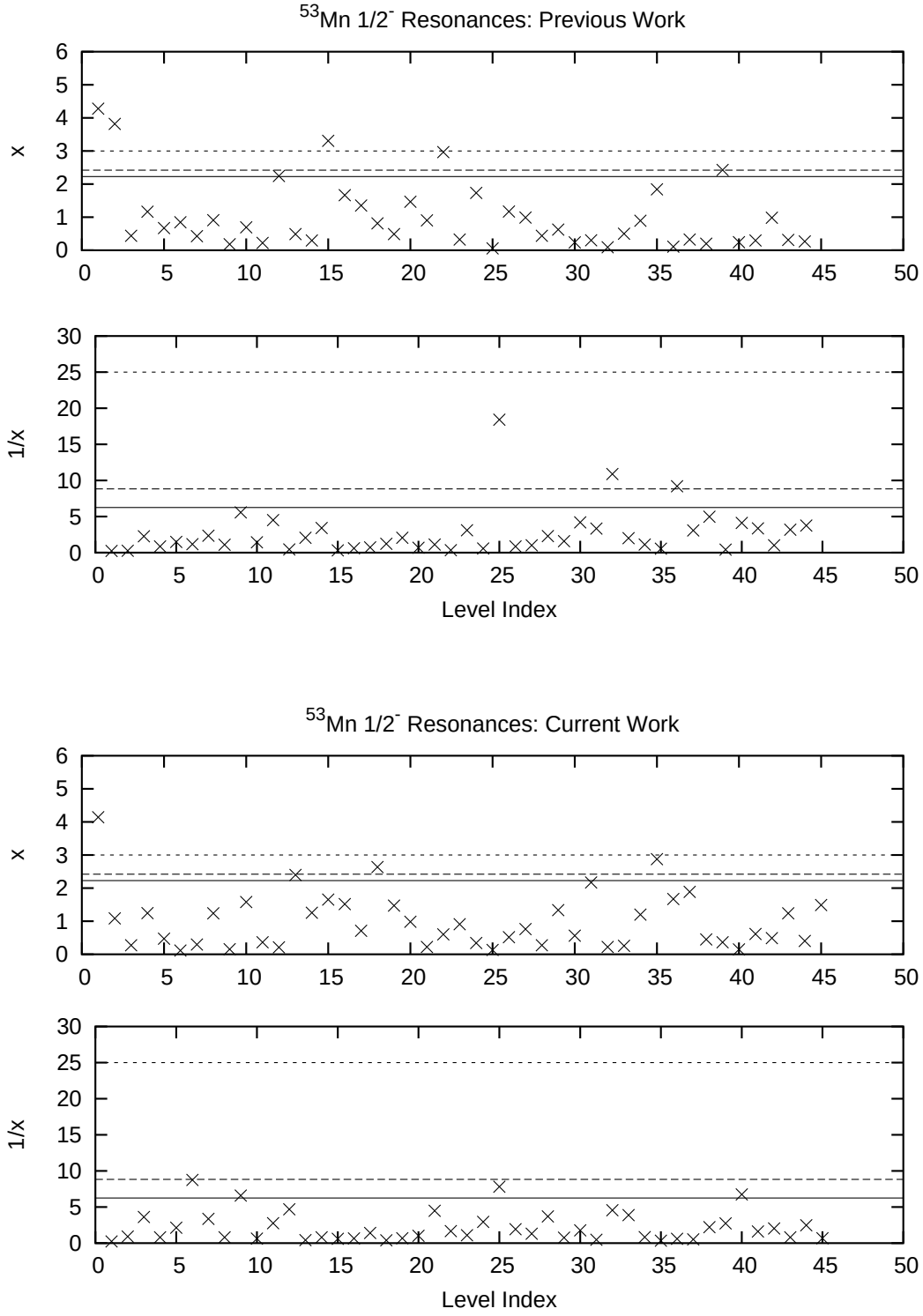

Figure 4.4: The spacing anomaly plots for the $J^\pi = \frac{1}{2}^-$ level sequence obtained from the previous work (top) and current work (bottom). Reassignments and energy corrections to several levels result in an improvement in the overall agreement with the statistical limits.

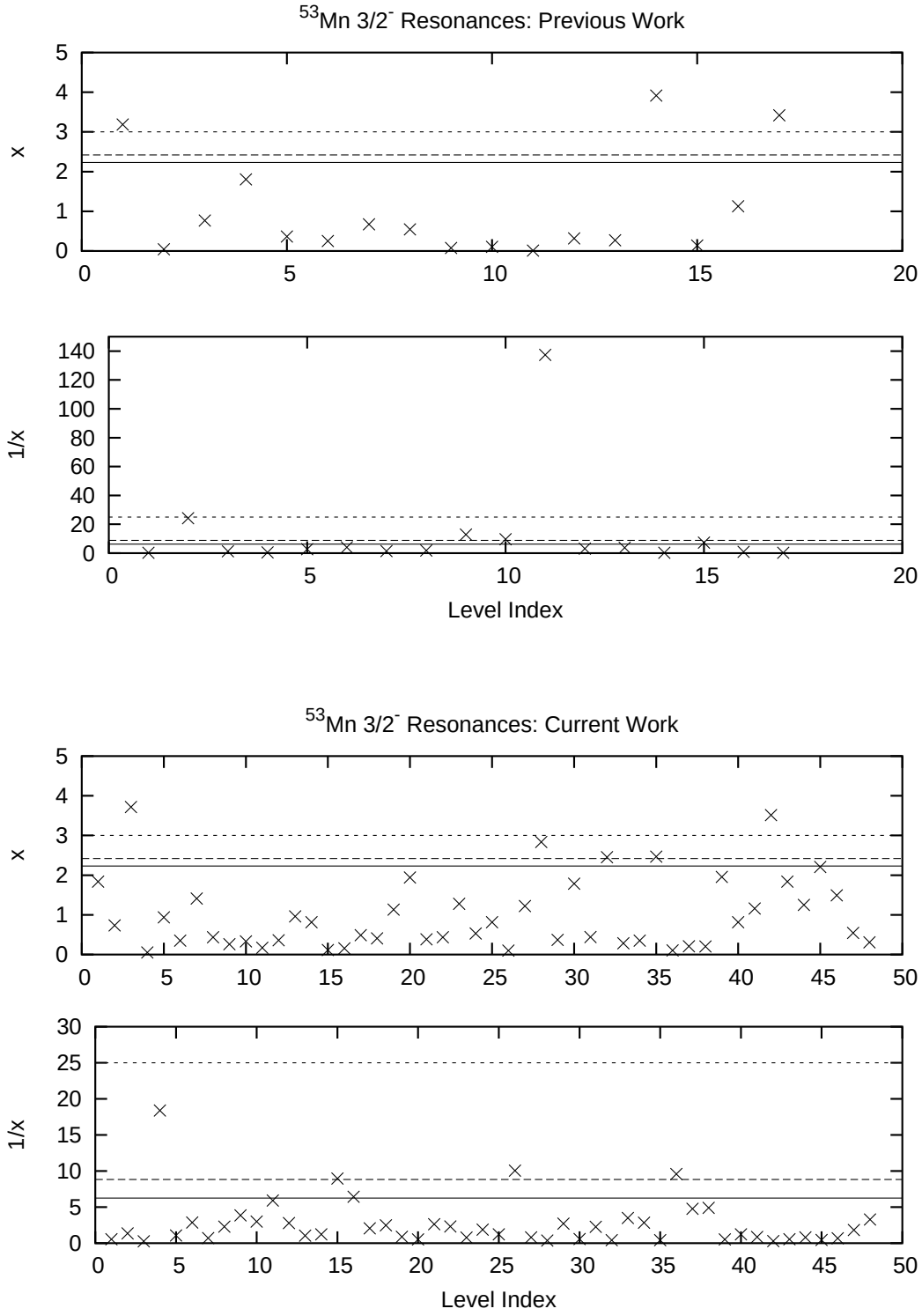

Figure 4.5: The spacing anomaly plots for the $J^\pi = \frac{3}{2}^-$ level sequence obtained from the previous work (top) and current work (bottom). Note the removal of the anomaly in the previous work at level index eleven which results from the removal of a spurious assignment.

analysis cannot be performed on the $\ell = 2$ case as it is a mixed sequence and therefore is not expected to obey the Wigner distribution.) The plots for the current work represent the results obtained after removal of several anomalies following the initial fitting of the experimental data. In general, the agreement is better in the $\frac{1}{x}$ plots that it is in the x plots. This is indicative of missing levels. As the strength analysis will show, there are some levels that are too weak to be detected experimentally.

4.2.2 Spacing Distributions

Comparisons of the nearest-neighbor spacing distributions to the Wigner and Poisson distributions are shown in Figures 4.6 - 4.9. The probability density for the NNSD is generated by sorting the spacings into bins of width $\frac{1}{3}$, and calculating $P(x)$ for the given interval. The results are then plotted as a histogram against the continuous theoretical curves. The probability distribution function for the nearest-neighbor spacings is generated by plotting the cumulative number of spacings in the ordered sequence versus the x values. The resulting "staircase" function is plotted against the continuous theoretical curves.

The agreement of the experimental results with the GOE varies by sequence. For the $J^\pi = \frac{1}{2}^+$ sequence, although the maximum in the Wigner distribution is reproduced by the binned data, the characteristic level repulsion is not apparent and the behavior near zero does not match the GOE distribution. The probability distribution function plot is also ambiguous. For the $J^\pi = \frac{1}{2}^-$ and $J^\pi = \frac{3}{2}^-$ sequences the overall agreement with the GOE is poor. Neither of the $P(x)$ plots exhibit evidence of level repulsion and in both cases anomalously large spacings lead to poor agreement for $x \gtrsim 2.5$. In both cases the $F(x)$ plots favor the Poisson distribution. Since the $\ell = 2$ mixed sequence consists of resonances with both $J^\pi = \frac{3}{2}^+$ and $\frac{5}{2}^+$,

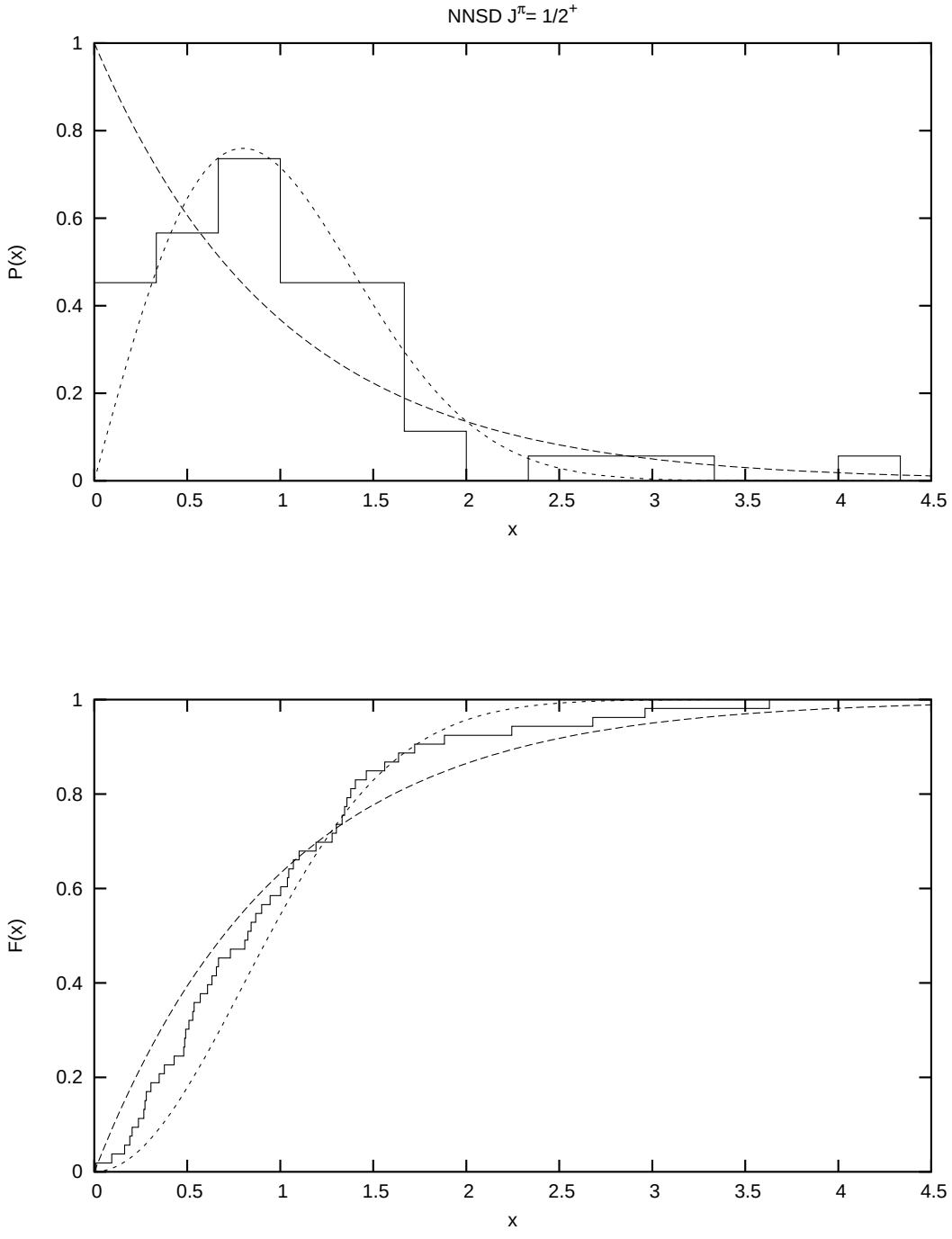

Figure 4.6: The nearest-neighbor spacing probability density function (upper) and nearest-neighbor spacing probability distribution function (lower) for the $J^{\pi} = \frac{1}{2}^{+}$ level sequence.

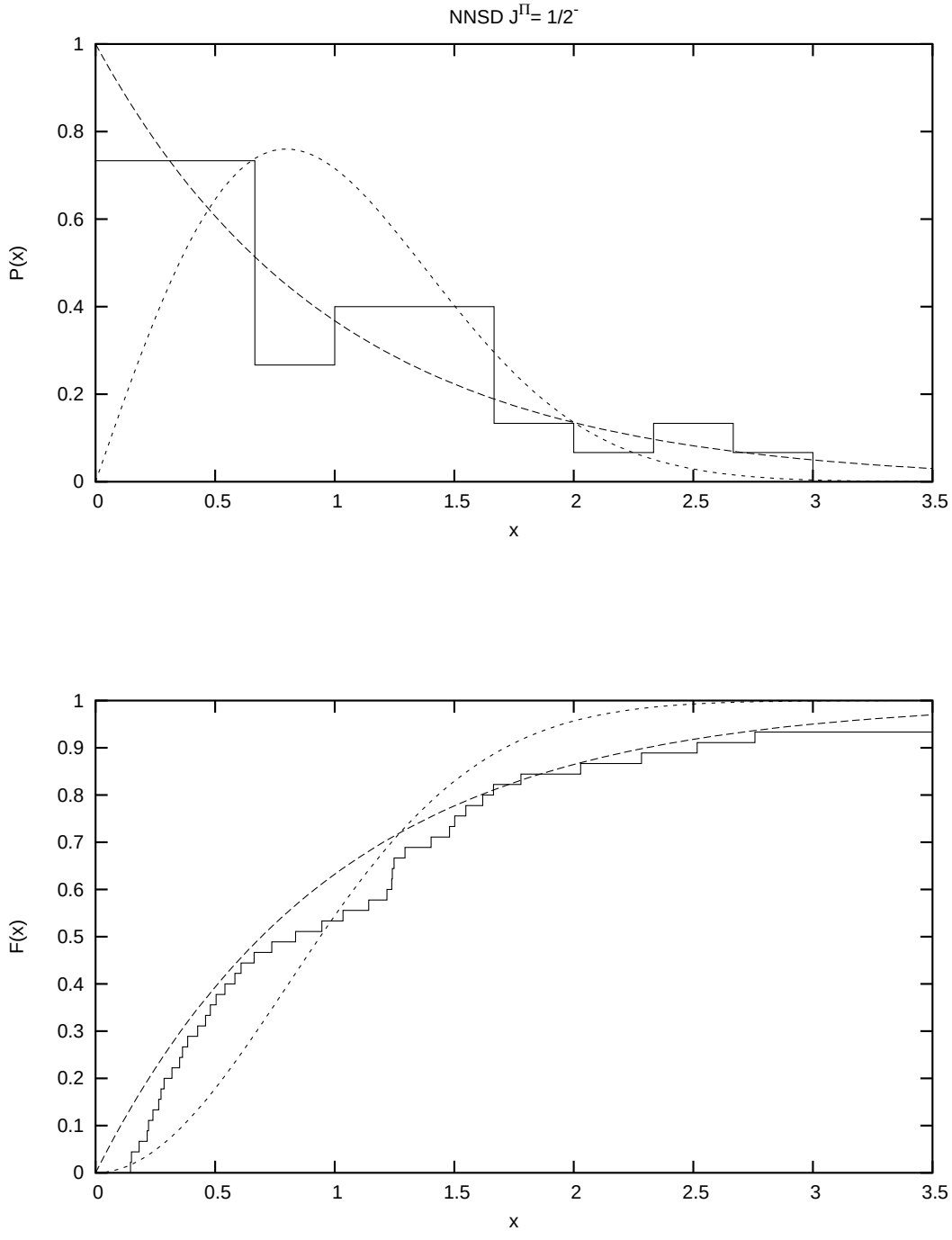

Figure 4.7: The nearest-neighbor spacing probability density function (upper) and nearest-neighbor spacing probability distribution function (lower) for the $J^\pi = \frac{1}{2}^-$ level sequence.

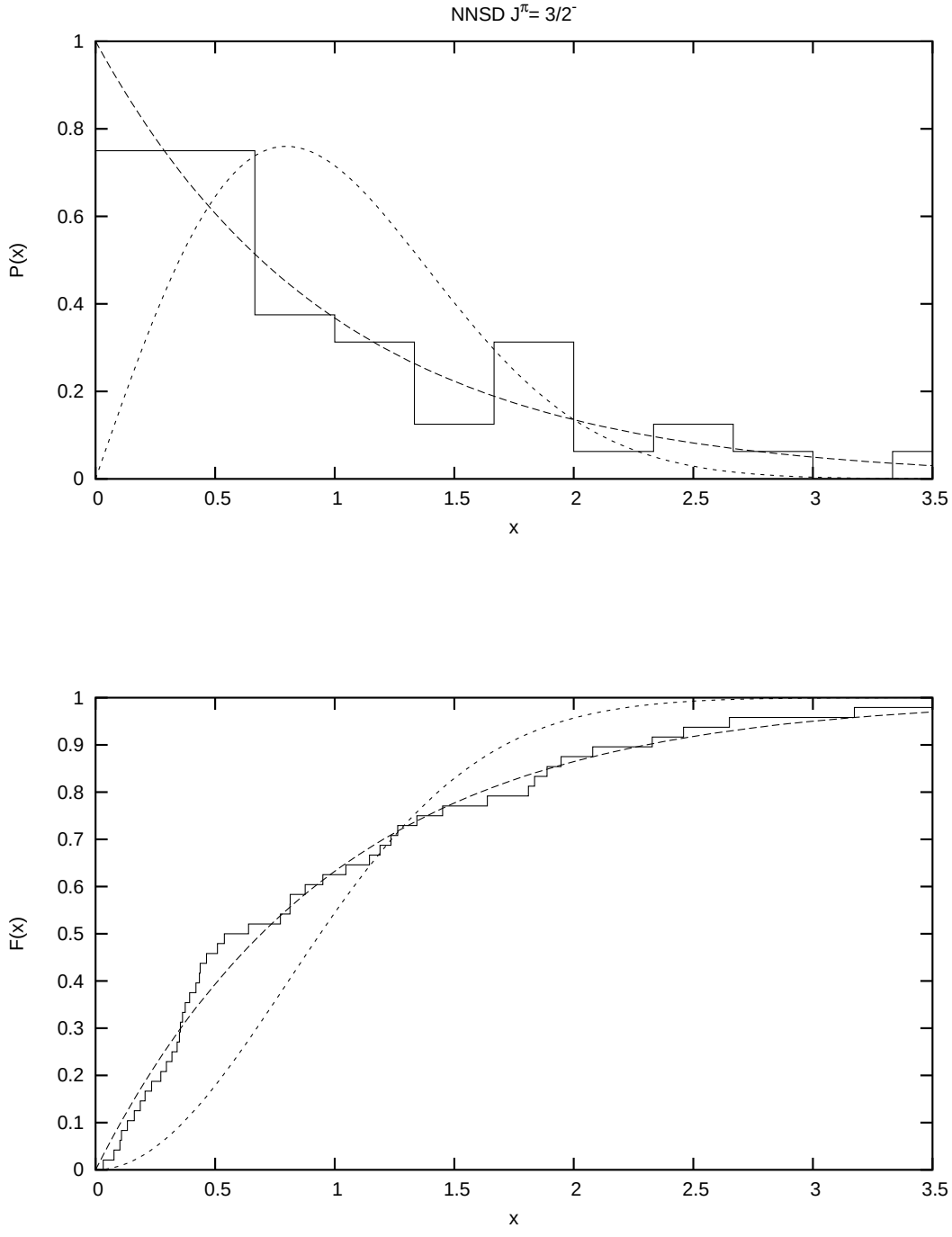

Figure 4.8: The nearest-neighbor spacing probability density function (upper) and nearest-neighbor spacing probability distribution function (lower) for the $J^{\pi} = \frac{3}{2}^{-}$ level sequence.

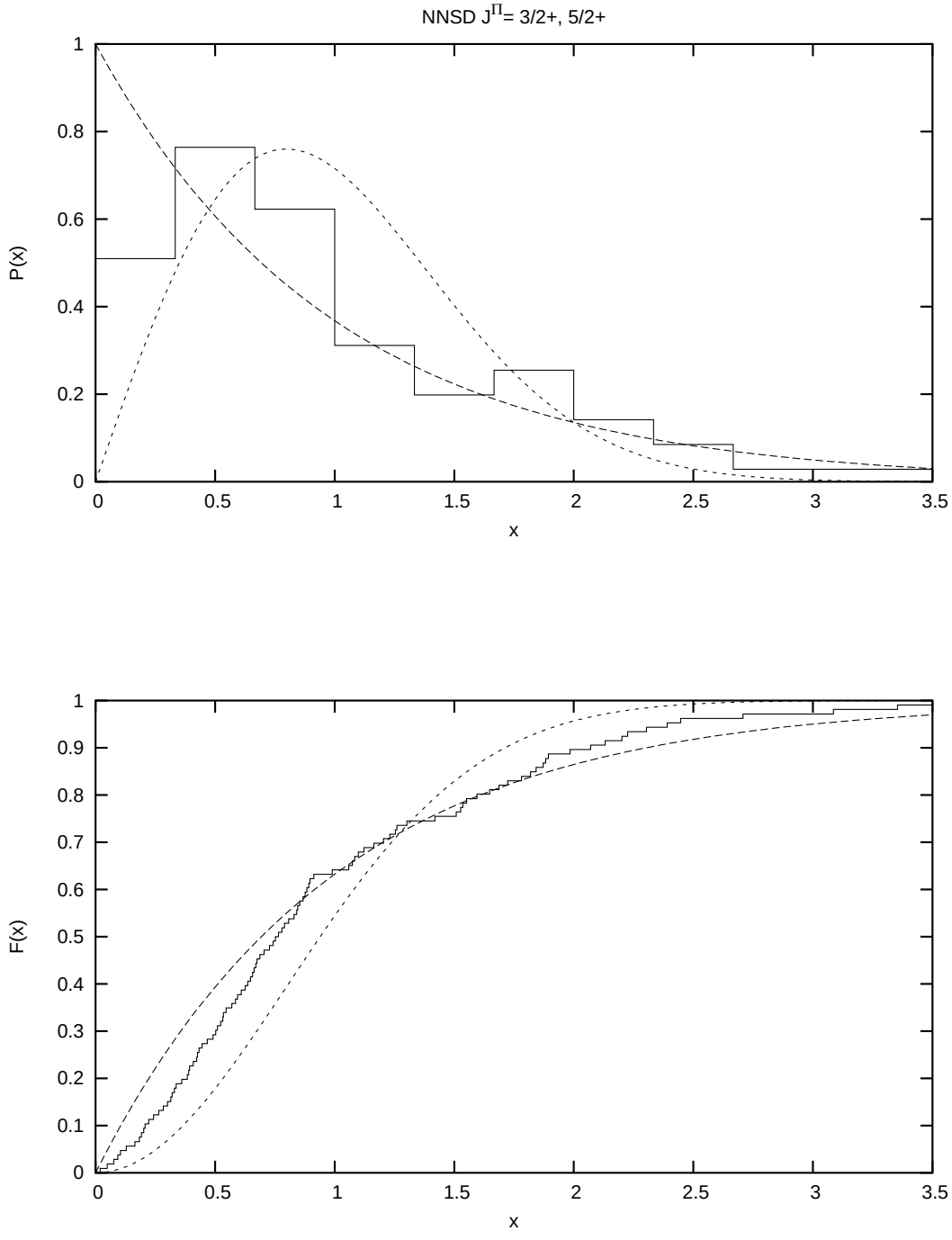

Figure 4.9: The nearest-neighbor spacing probability density function (upper) and nearest-neighbor spacing probability distribution function (lower) for the $J^\pi = \frac{3}{2}^+, \frac{3}{2}^+$ combined sequence.

direct comparison of the NNSD with the GOE is not valid. The distribution for such a mixed sequence is expected to fall somewhere between the GOE and Poisson distributions. The NNSD plot for the $\ell = 2$ combined sequence gives the expected result.

4.3 Reduced Width Analysis

Another statistical test of data quality involves the distribution of the reduced widths. The data must first be corrected for the presence of isobaric analog states. The reduced width distributions are then compared to the predictions of the GOE. Finally, the strength functions are determined for each sequence.

For a sequence containing levels with reduced widths γ^2 and mean $\langle\gamma^2\rangle$, the dimensionless parameter y is defined by

$$y_i \equiv \frac{\gamma_i^2}{\langle\gamma^2\rangle}. \tag{4.8}$$

The GOE prediction for the probability density function is

$$P(y) = \frac{1}{\sqrt{2\pi y}} e^{-\frac{y}{2}}, \tag{4.9}$$

which is known as the Porter-Thomas distribution [Por56]. Examination of $P(y)$ reveals that the smaller reduced widths have the largest probability. The weakest resonances, however, are the least likely to be observed experimentally. Therefore, the experimental sequences are expected to be incomplete. The majority of the total reduced width for a sequence, however, is contained in the levels with the largest reduced widths. For example, if the weakest 25% of the levels are missing from a sequence, only 1% of the cumulative strength of the sequence will be lost.

4.3.1 Identification of Analog States

When examining the reduced widths, care must be taken to identify isobaric analog states. Isospin is the quantum number which reflects the charge independence of the nuclear force. Nucleons are assigned isospin $T = \frac{1}{2}$, and the z-projections of the isospin vector are $T_z = \frac{1}{2}$ and $T_z = -\frac{1}{2}$ for the neutron and proton respectively. For a nucleus comprised of N neutrons and Z protons, the z-component of the total nuclear isospin is $T_z = \frac{1}{2}(N - Z)$. Isobars are nuclei with the same number of nucleons, A.

The family of isobars of interest in the current work is the $A = 53$ multiplet; the focus here is the ^{53}Cr "parent" and the ^{53}Mn "daughter" or analog. The daughter state is formed by exchanging a neutron in the parent for a proton. Analog states have the same J^π and E_x when corrected for the internal energy differences between isobars. The energy difference between the parent and daughter consists of the Coulomb energy difference, ΔE$_c$, between the isobars and the mass-energy difference, δ, between the neutron and the proton. The analog state will then have an excitation energy of ΔE$_c$ - δ above the parent state. The relationship between the excitation energy, E_x, in the parent state and center of mass energy, E_{cm}, of the projectile proton is given by

$$\Delta E_c = B_n + E_{cm} - E_x, \tag{4.10}$$

where B_n is the neutron separation energy for the parent. An estimate for ΔE_c can be obtained via the semi-empirical approximation [Jän69]

$$\Delta E_c \approx \frac{C_1 Z_< + C_2}{A^{\frac{1}{3}}}, \tag{4.11}$$

with $C_1 = 1389$ keV and $C_2 = -2041$ keV. $Z_<$ is the number of protons in the target

nucleus. For $A = 53$ and $Z = 24$, this expression yields $\Delta E_c \approx 8.331$ MeV. Equation 4.10 can then be re-arranged to give an approximate relationship between the center of mass energy of the incident proton and the excitation energy in the parent, $E_{cm} = E_x + 0.392$ MeV. A graphical representation of the energy relationships within the parent-daughter system is given in Figure 4.10. There is an enhancement of the

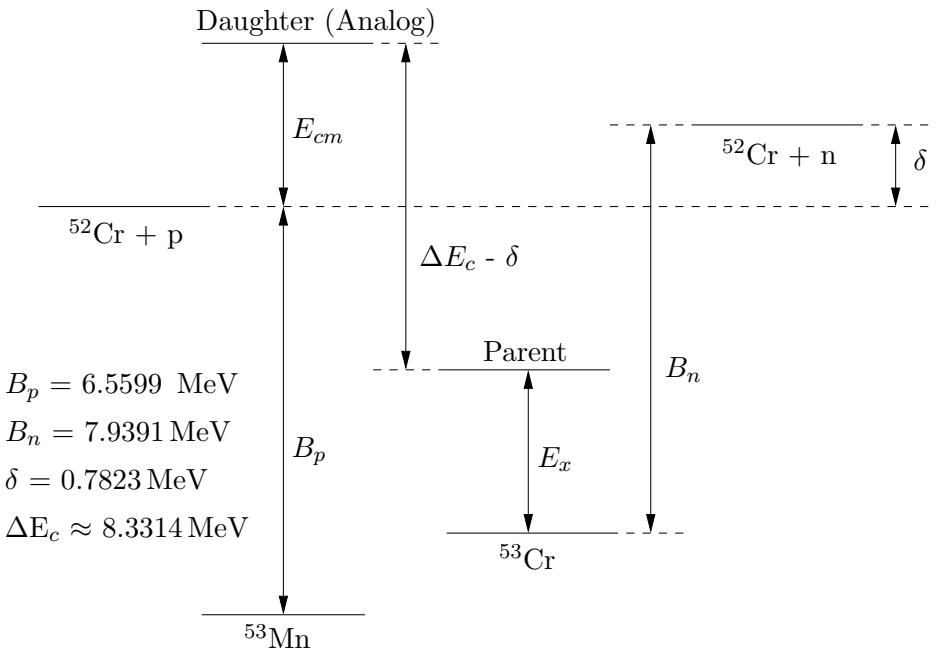

Figure 4.10: The energy relationships in the parent-daughter system consisting of ^{53}Cr and ^{53}Mn. The neutron separation energy for ^{53}Cr and proton separation energy for ^{53}Mn are taken from the 2003 mass evaluation [Nnd04].

width of the analog state in the daughter nucleus.

The analog state may enhance the widths of one or more neighboring states (fragments) in the daughter that share the same J^π. This effect distorts the reduced width distribution. It is possible to analyze the fine structure of fragmented analog states [Bil76], but such detailed analysis is not required for the current work. In order to compare the reduced width distribution with the theoretical predictions, it suffices

Table 4.1: Summary of isobaric analog states removed from the sequences prior to the reduced width analysis.

	^{53}Cr Parent State	^{53}Mn Analog Fragments		
J^π	E_x(MeV)	E_p (MeV)	E_{cm} (MeV)	E_x (MeV)
$\frac{1}{2}^-$	2.6699	3.1297	3.0701	9.6300
		3.1365	3.0768	9.6367
$\frac{3}{2}^-$	2.3207	2.7710	2.7182	9.2781
		2.7752	2.7224	9.2823
		2.7886	2.7356	9.2954

to remove the (possibly fragmented) analog states which have noticeable effects on the reduced widths. The identification of the analog states is facilitated by plotting the reduced widths γ^2, and the reduced width sums $\Sigma\gamma^2$ versus excitation energy, as shown in figures 4.14 - 4.18. Analog states often are seen as sudden, large increases in the plots of $\Sigma\gamma^2$ vs E_x. In the reduced width plots the presence of analog states is indicated in the $\frac{1}{2}^-$ and $\frac{3}{2}^-$ sequences. The analog states are not highly fragmented in either case and the analog states can be identified by inspection. The analog fragments are listed in Table 4.1. As previously stated, fitting the distributions of the analog states is not a goal of the current work. In the previous work however, uncertainty remained as to possible fragmentation of the $E_x = 2.6699$ MeV, $J^\pi = \frac{1}{2}^-$ parent state in ^{53}Cr beyond the energy range measured. New data collected at $E_p >$ 3.2 MeV, however, do not indicate the presence of additional daughter states.

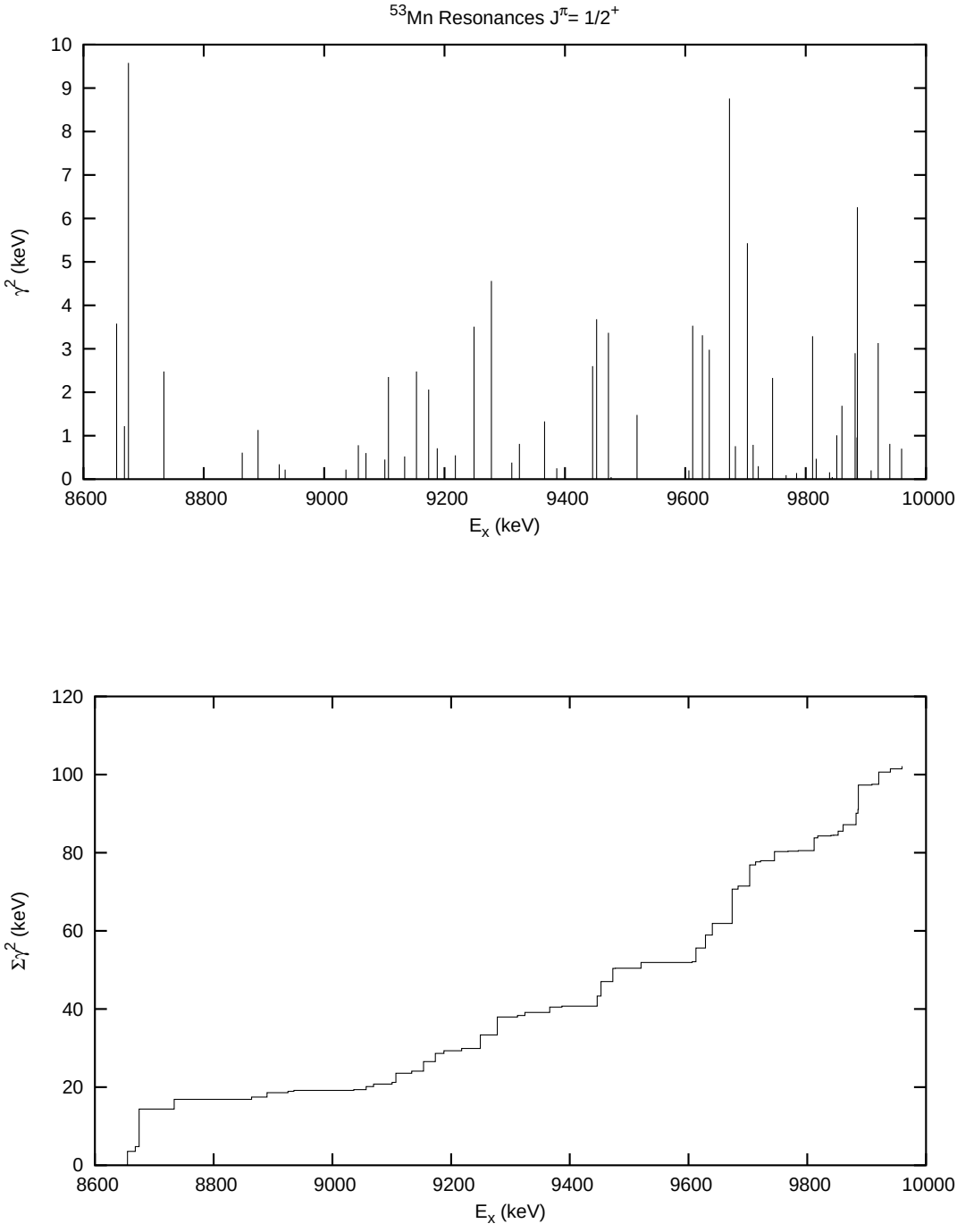

Figure 4.11: The γ^2 and $\Sigma\gamma^2$plots for the $J^\pi = \frac{1}{2}^+$ level sequence. No analog states are observed in this sequence.

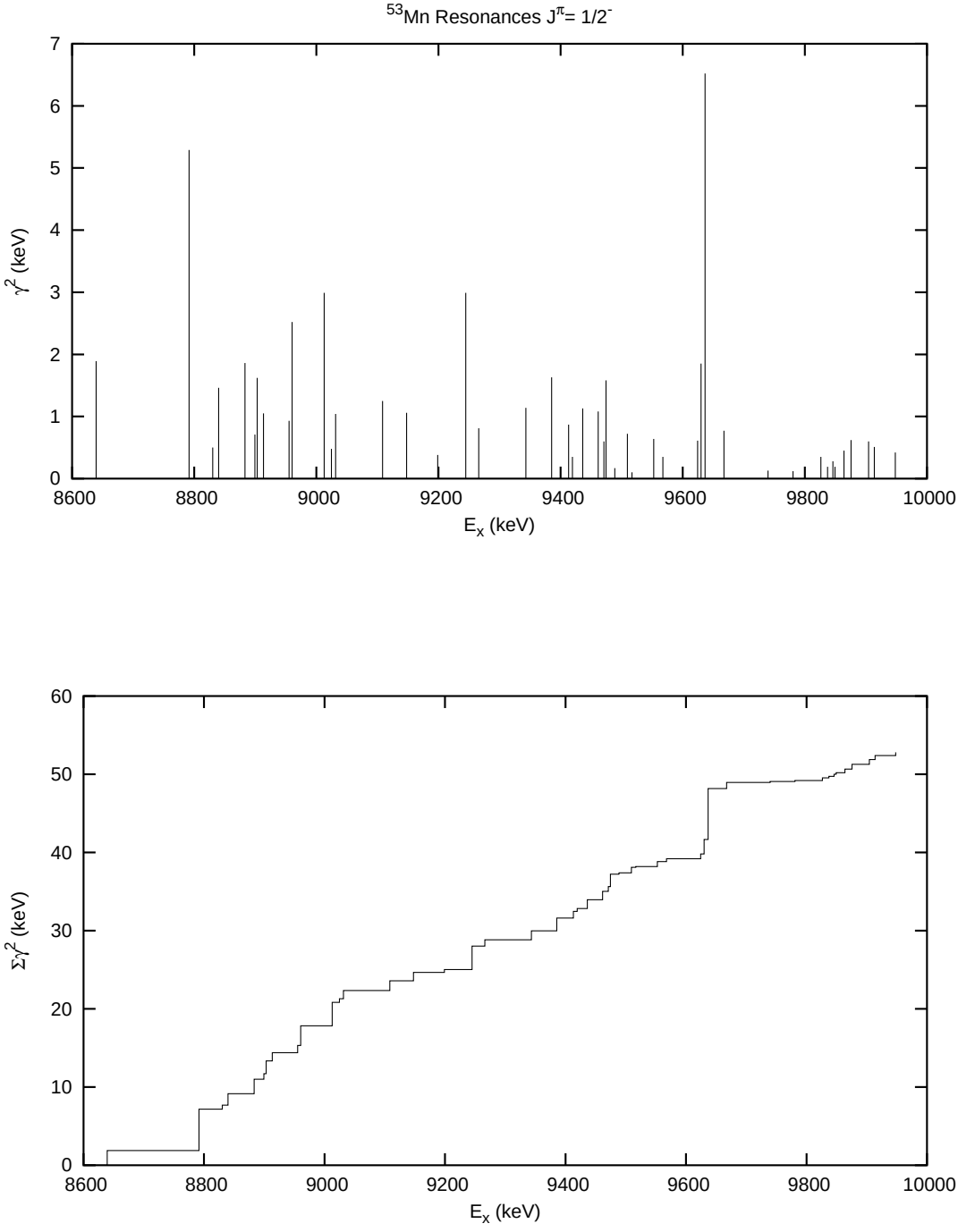

Figure 4.12: The γ^2 and $\Sigma\gamma^2$plots for the $J^\pi = \frac{1}{2}^-$ level sequence. The presence of an analog state is indicated at $E_x \sim 9600$ keV.

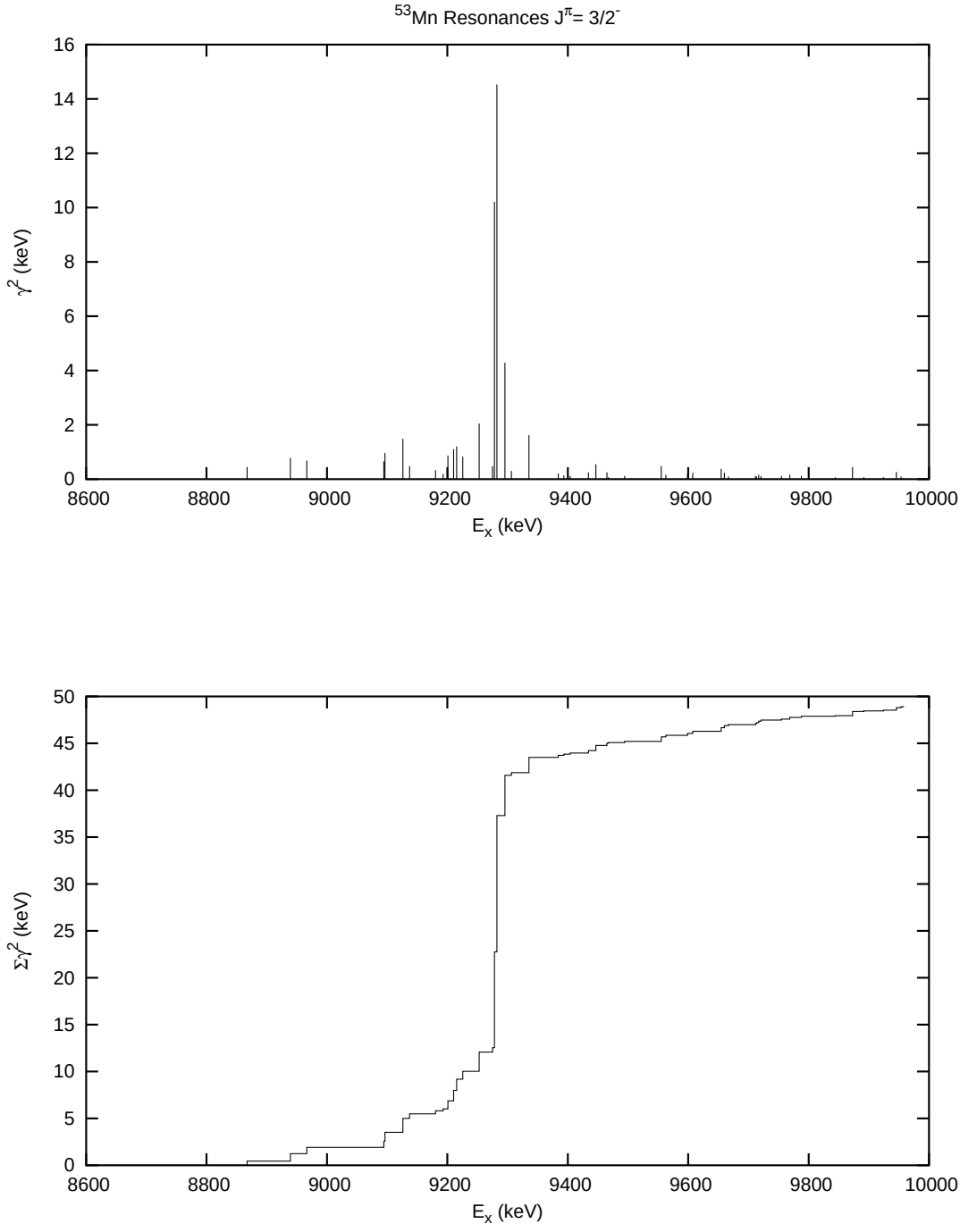

Figure 4.13: The γ^2 and $\Sigma\gamma^2$plots for the $J^\pi = \frac{3}{2}^-$ level sequence. The presence of an analog state is indicated at $E_x \sim 9300$ keV.

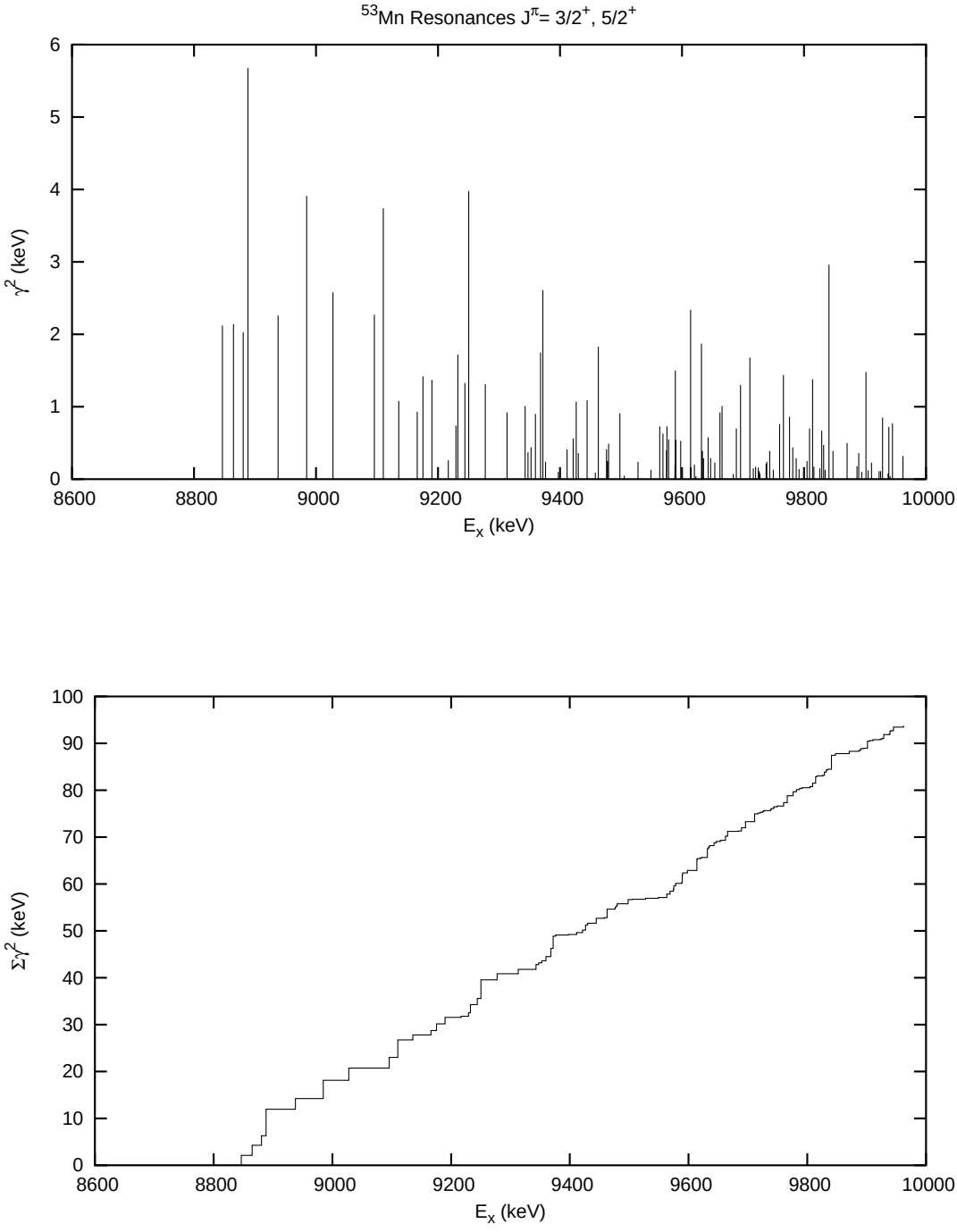

Figure 4.14: The γ^2 and $\Sigma\gamma^2$plots for the $J^\pi = \frac{3}{2}^+, \frac{5}{2}^+$ combined sequence. No analog states are observed in this sequence.

4.3.2 Reduced Width Distributions

The reduced width distributions can be used to test the completeness of a level sequence. The histogrammed reduced widths for each sequence are plotted along with the scaled probability density functions. The $\frac{1}{\sqrt{y}}$ behavior of the Porter-Thomas distribution is removed by plotting $y^{\frac{1}{2}}P(y)$ vs y. A comparison which removes the effect of bin size in the histograms is also made by plotting the integrated probability density function versus the cumulative probability for each sequence. In general, the data agree reasonably well with the Porter-Thomas distribution above a cut-off value. The absence of levels is apparent in all of the sequences. As predicted, there is strong evidence of missing levels at small values of y. Figures 4.15-4.18 show the plots described above for each level sequence.

For the $J^\pi = \frac{1}{2}^+$ sequence, there is nominal agreement with GOE statistics in both plots, and a sharp low-y cut-off is apparent. In the $J^\pi = \frac{1}{2}^-$ case, the agreement in the scaled probability density function is again reasonable, while the probability distribution function exhibits stronger evidence for missing levels with small reduced widths. The $J^\pi = \frac{3}{2}^-$ results are similar to these for the $\frac{1}{2}^-$sequence with slightly better agreement between the probability distribution and the binned data. Interestingly, the agreement of the $J^\pi = \frac{5}{2}^+, \frac{3}{2}^+$ combined sequence is as good or better than any of the J^π specific sequences. The combined sequence is not expected to follow the GOE, however, and should only be used for comparison to the other sequences.

4.3.3 Strength Functions

Models of nuclear reactions typically predict values for the strength function S. S is therefore useful in testing the agreement of a particular model with experimental

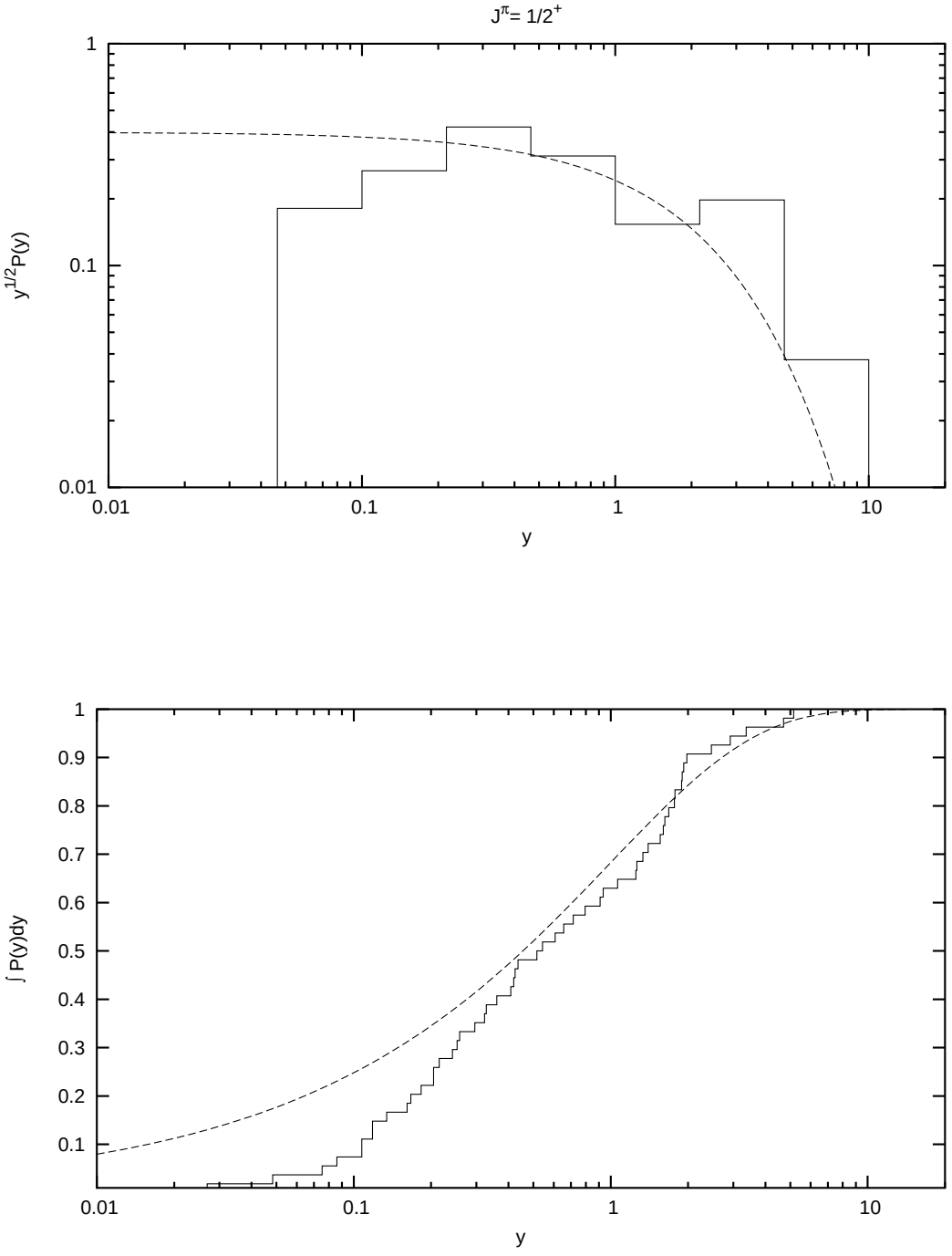

Figure 4.15: The scaled reduced width probability density function (top) and probability distribution function (bottom) for the $J^\pi = \frac{1}{2}^+$ level sequence. The dashed line shows the Porter-Thomas distribution.

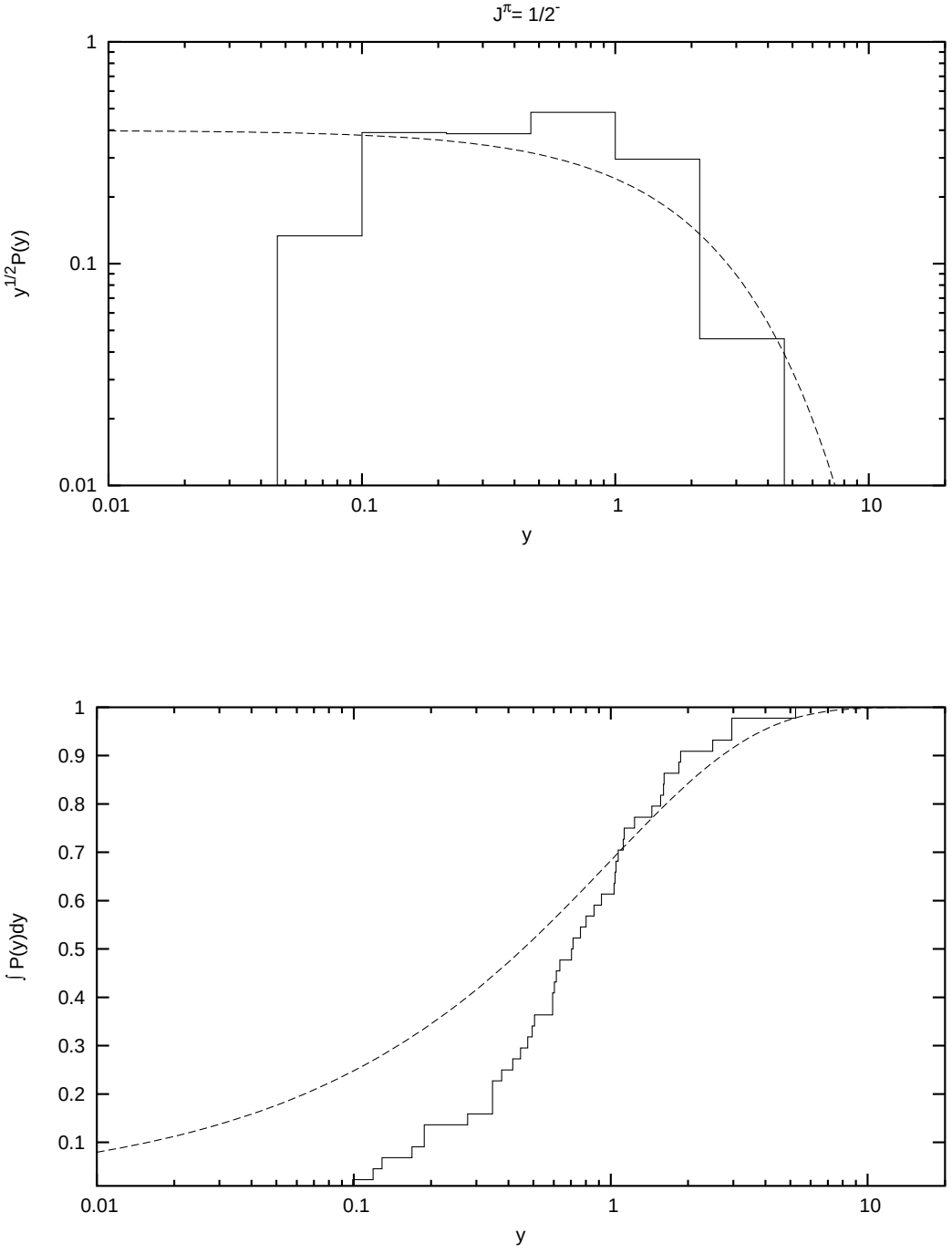

Figure 4.16: The scaled reduced width probability density function (top) and probability distribution function (bottom) for the $J^\pi = \frac{1}{2}^-$ level sequence. The dashed line shows the Porter-Thomas distribution.

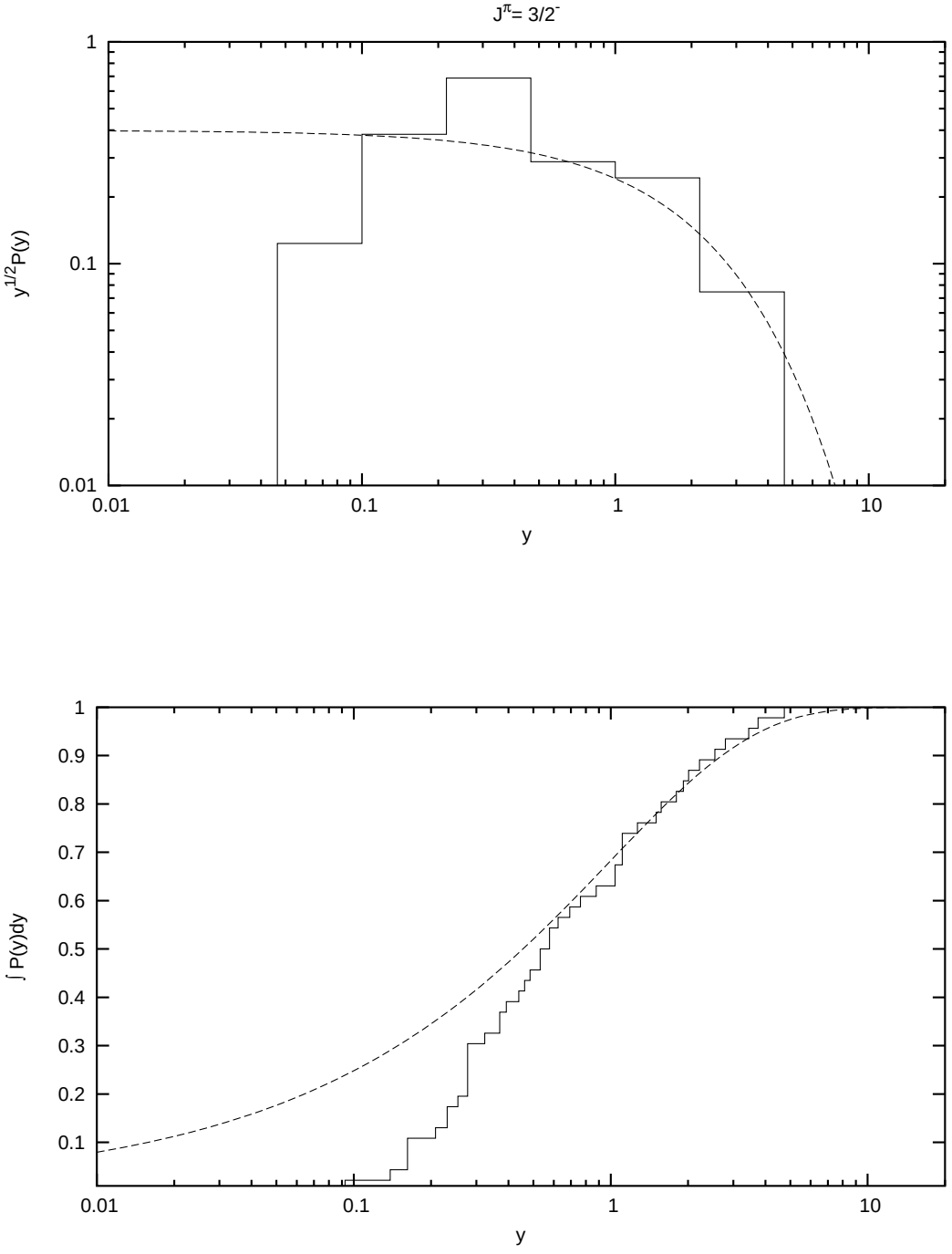

Figure 4.17: The scaled reduced width probability density function (top) and probability distribution function (bottom) for the $J^\pi = \frac{3}{2}^-$level sequence. The dashed line shows the Porter-Thomas distribution.

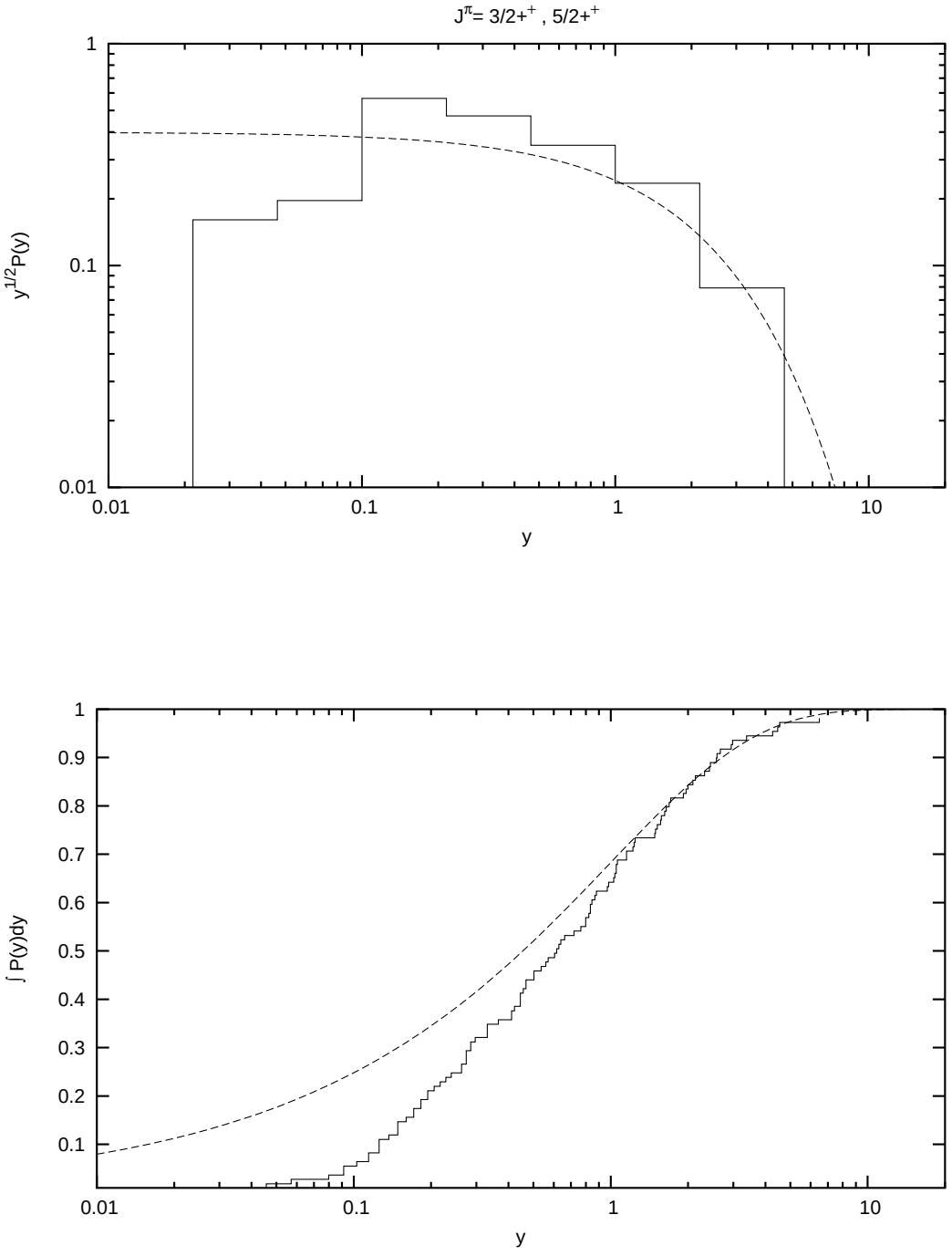

Figure 4.18: The scaled reduced width probability density function (top) and probability distribution function (bottom) for the $J^\pi = \frac{3}{2}^+, \frac{5}{2}^+$ combined level sequence. The dashed line shows the Porter-Thomas distribution. This combined distribution is not expected to be described by the Porter-Thomas distribution. It is shown here only for comparison with other sequences

results. For a sequence of N levels with mean level spacing D, the strength function is defined as

$$S \equiv \frac{\langle \gamma^2 \rangle}{D} \approx \frac{\Sigma \gamma^2}{\Delta E_x}, \tag{4.12}$$

where ΔE_x is the total range of excitation energies. A value of S is calculated for each level sequence after the analog states have been removed. The uncertainty in S is [Lyn68]

$$\delta S = S\sqrt{\frac{2}{N}}. \tag{4.13}$$

We take N to be the estimated number of levels in the sequence (see next section). The proton strength functions have been determined previously for E_p = 2.10-3.23 MeV by Moses *et al.* [Mos71], and for E_p = 3.20-4.76 MeV by Ozawa *et al.* [Oza85]. A theoretical value has also been calculated for E_p = 3.0 MeV by Matsuzaki and Arai [Mat83] for the $J = 1$ cases. The values of S obtained in the current work are listed in Table 4.2 along with the values obtained in the previous experimental and theoretical work.

Table 4.2: Proton strength functions for ^{52}Cr(p,p$_0$).

J^π	$\Sigma\gamma^2_{obs}$ (keV)	S			
	Current†	Current†	Moses‡	Ozawa*	Theory$^*_*$
$\frac{1}{2}^+$	102.15	0.076 ± 0.014	0.067 ± 0.015	0.093 ± 0.012	0.052
$\frac{1}{2}^-$	44.43	0.033 ± 0.006	0.044 ± 0.009	0.014 ± 0.003	0.031
$\frac{3}{2}^-$	19.91	0.015 ± 0.003	0.010 ± 0.004	0.010 ± 0.002	-
$\frac{3}{2}^+$	18.49	0.014 ± 0.004	0.009 ± 0.004	0.068 ± 0.008	-
$\frac{5}{2}^+$	75.29	0.056 ± 0.008	0.041 ± 0.010	0.044 ± 0.006	-
$(\frac{3}{2}^+,\frac{5}{2}^+)$	93.78	0.070 ± 0.009	-	-	-

† Experimental results for E$_p$ = 2.1039-3.4711 MeV

‡ Experimental results for E$_p$ = 2.10-3.23 MeV [Mos71]

* Experimental results for E$_p$ = 3.20-4.76 Mev [Oza85]

$^*_*$ Theroretical results for E$_p$ = 3.00 MeV [Mat83]

4.4 Level Densities

The level density ρ, for a sequence of N levels, over an energy range ΔE is defined by

$$\rho = \frac{N}{\Delta E}. \tag{4.14}$$

The accuracy of ρ depends upon complete counting of the levels in the sequence. As the analysis has shown, completeness is nearly impossible to attain. In the case of the p + ^{52}Cr reaction, the weakest of the resonances go undetected. The effects of missing levels were also seen in the spacing distributions. In order to determine the level density for a given sequence, it is therefore necessary to estimate the true number of levels that comprise a sequence from the available data. There exist two complimentary methods of estimating the observed fraction of levels in a given sequence. Both make use of maximum likelihood estimators.

The analysis of the reduced width distributions showed a minimum observable width in each of the sequences. The first method of estimating the observed fraction of levels in a sequence models this behavior. The technique described by Agvaanluvsan [Agv03] uses a version of the Porter-Thomas distribution which was discussed by Fröhner [Frö80]. This "truncated" probability density function is given by

$$P_f(y) = \begin{cases} 0 & \text{if } y < y_0 \\ \dfrac{1}{\operatorname{erfc}(\sqrt{y_0/2})} \dfrac{e^{\frac{-y}{2}}}{\sqrt{2\pi y}} & \text{if } y \geq y_0 \end{cases}, \tag{4.15}$$

where y_0 is the smallest observed normalized reduced width. Using this form of the probability density function, the maximum likelihood estimator for $\langle\gamma^2\rangle$is then

$$\langle\gamma^2\rangle = \langle\gamma^2\rangle_{obs}\left(1 + \sqrt{\frac{2y_0}{\pi}}\frac{e^{-y_0/2}}{\operatorname{erfc}\sqrt{y_0/2}}\right)^{-1}. \tag{4.16}$$

A new estimate for y_0 is obtained by substituting the value of $\langle\gamma^2\rangle$ into the definition

$$y_i = \frac{\gamma_i^2}{\langle\gamma^2\rangle}. \tag{4.17}$$

This new estimate of y_0 is then substituted back into Eq. 4.16 and the process iterated until $\langle\gamma^2\rangle$ converges. The observed fraction, f_w, can be estimated by comparison of the resulting $\langle\gamma^2\rangle$ to $\langle\gamma^2\rangle_{obs}$. As with the analysis of the reduced widths in the previous section, it is important that the non-statistical analog states be removed from the sequences prior to calculating the estimate of the the missing fraction using this method.

Another method of estimating the observed fraction of levels uses the nearest-neighbor spacing distributions to estimate the observed fraction, f_s. The probability density function for the level spacings in an incomplete sequence as has been discussed by Watson *et al.* [Wat81] and by Agvaanluvsan *et al.* [Agv03]. The function is,

$$P(x) = \sum_{k=0}^{\infty} f_s(1-f_s)^k P(k;x), \tag{4.18}$$

where $P(k;x)$ is the k-th nearest-neighbor distribution. FORTRAN codes have been written by Agvaanluvsan which, given the energies and reduced widths of the observed levels, calculate values for f_w and f_s and the associated uncertainties, which may be asymmetric. Once f_s and f_w are calculated, an estimate of the observed fraction is obtained via the weighted sum of f_w and f_s. The uncertainty δf is given by

$$\left(\frac{1}{\delta f}\right)^2 = \left(\frac{1}{\delta f_w}\right)^2 + \left(\frac{1}{\delta f_s}\right)^2. \tag{4.19}$$

It is now possible to express the corrected number of levels as

$$N_{cor} = \frac{N_{obs}}{f}, \tag{4.20}$$

and the resulting level density is then

$$\rho = \frac{N_{cor}}{\Delta E}. \tag{4.21}$$

There are two sources of uncertainty in the calculation of ρ. The first,

$$\delta\rho_1 = \rho\sqrt{\frac{0.27}{N_{cor}}}, \tag{4.22}$$

is due to the finite number of resonances in the sequence and is taken from Lynn [Lyn68]. The second,

$$\delta\rho_2 = \rho\frac{\delta f}{f}, \tag{4.23}$$

arises from the calculation of the observed fraction. The resulting uncertainty in the level density is then

$$\delta\rho = \sqrt{\delta\rho_1^2 + \delta\rho_2^2} \tag{4.24}$$

The missing fraction estimates f_s and f_w may have asymmetric uncertainties which are propagated throughout the calculation of N_{cor} and, ultimately, ρ. The level densities for all of the J^π specific sequences analyzed are shown in Table 4.3.

Since the $\ell = 2$ combined sequence contains levels with both $J^\pi = \frac{3}{2}^+$ and $J^\pi = \frac{5}{2}^+$ the missing fraction estimation procedure described previously is not applicable. The level density for the $\ell = 2$ combined sequence is therefore obtained using $\rho = \frac{N_{obs}}{\Delta E}$ and the uncertainty is taken to be $\delta\rho_1$. Using these expressions gives a value of $\rho = 0.080 \pm 0.004$.

Table 4.3: Level densities for the ^{53}Mn level sequences.

J^π	N_{obs}	f_w	f_s	f	N_{cor}	ρ (MeV)$^{-1}$
$\frac{1}{2}^+$	54	$0.86^{+0.13}_{-0.14}$	$0.88^{+0.05}_{-0.06}$	$0.88^{+0.05}_{-0.06}$	61	46±4
$\frac{1}{2}^-$	46	$0.72^{+0.17}_{-0.13}$	$0.86^{+0.06}_{-0.07}$	0.84±0.06	55	41±4
$\frac{3}{2}^-$	49	$0.73^{+0.16}_{-0.13}$	$0.83^{+0.06}_{-0.07}$	0.81±0.06	60	45±5

Although the dependence of ρ on excitation energy is fairly well understood, the dependence of level densities on parity remains a topic of interest. The parity asymmetry

$$\alpha = \frac{\rho_+ - \rho_-}{\rho_+ + \rho_-}, \tag{4.25}$$

characterizes this dependence of level densities of sequences of the same J on parity. For the $J = \frac{1}{2}$ case a value of $\alpha = +0.01^{+0.06}_{-0.07}$ is obtained. Although no parity asymmetry is observed in this case, the uncertainty is relatively large, and therefore no conclusive statement can be made.

Chapter 5

Summary and Results

High resolution measurements of the differential cross-sections for the ^{52}Cr(p,p$_0$) and ^{52}Cr(p,p$_1$) reactions were performed over the energy range E_p = 2.1039-3.4711 MeV and E_p = 2.6101-3.4711 MeV, respectively. The goal of this work was the improved determination of level densities in the nuclide ^{53}Mn. The observed cross sections were fit using the multilevel, multichannel, R-matrix code MULTI6. A total of 263 resonances were observed, and 62 resonances had measurable contributions from the first inelastic channel. 66 new levels were identified, and 25 of the previously observed resonances were given new J^π assignments.

The observed resonances were sorted according to total angular momentum J and parity π and statistical tests performed. The exponential dependence of the level densities on excitation energy was removed, and the J^π specific sequences were corrected using the spacing anomaly analysis method. Several of the assignments made during data fitting were revised, and many spacing anomalies were resolved. Some anomalies remained after repeated application of the technique. The nearest-neighbor spacing distributions were compared to the Wigner distribution, which is the predicted distribution for the GOE. None of the sequences exhibit notable agree-

ment with the GOE and the probability distribution functions generally favor Poisson statistics.

The sequences were examined for the presence of isobaric analog states prior to analysis of the reduced width distributions. Analog states were observed in the $J^\pi = \frac{1}{2}^-$ and $\frac{3}{2}^-$ sequences, and the reduced widths of 5 levels we not included in the reduced width analysis. The distributions of the reduced widths were also compared to the Porter-Thomas distribution which is the predicted distribution of the GOE. Although the $\frac{1}{2}^+$ sequence exhibits a qualitative agreement above some small value of γ^2, the sequences do not agree well overall. The probability distribution functions indicate the absence of levels with small reduced widths. In general there is still strong evidence that some levels are missing or misassigned.

The observed fraction of levels for each of the J^π specific sequences was estimated, and the numbers of levels in each of the sequences were corrected using the methods described by Agvaanluvsan. Strength functions were determined using the corrected number of levels for each unique J^π sequence as well as the $J^\pi = \frac{3}{2}^+, \frac{5}{2}^+$ combined sequence. Level densities were determined using the corrected number of levels for each unique J^π sequence as well as the $J^\pi = \frac{3}{2}^+, \frac{5}{2}^+$ combined sequence. The parity asymmetry of the level densities was determined for the $J = \frac{1}{2}$ sequences. No dependence of the level densities on parity was observed.

The size of the data set has increased by 34%, and the spacing anomaly analysis indicates that the data is of higher quality than the previous work. The lack of agreement with the GOE predictions, however, indicates that the level sequences are still neither pure nor complete. Although the experimental system has been improved, the results indicate that not all of the proton resonances in ^{53}Mn in the energy range covered were observed.

Appendix A

Data and Fits

This appendix contains the differential cross-sections measured in this experiment and calculated with MULTI6. The plots are presented in 100-keV segments and all five angles are presented concurrently. The range of the ^{52}Cr(p,p$_0$) data is $2.1039 \leq E_p \leq 3.4711$. The range of the ^{52}Cr(p,p$_1$) data is 2.6101 $E_p \leq 3.4711$. The ^{52}Cr(p,p$_0$) data are presented first, followed by the ^{52}Cr(p,p$_1$) data.

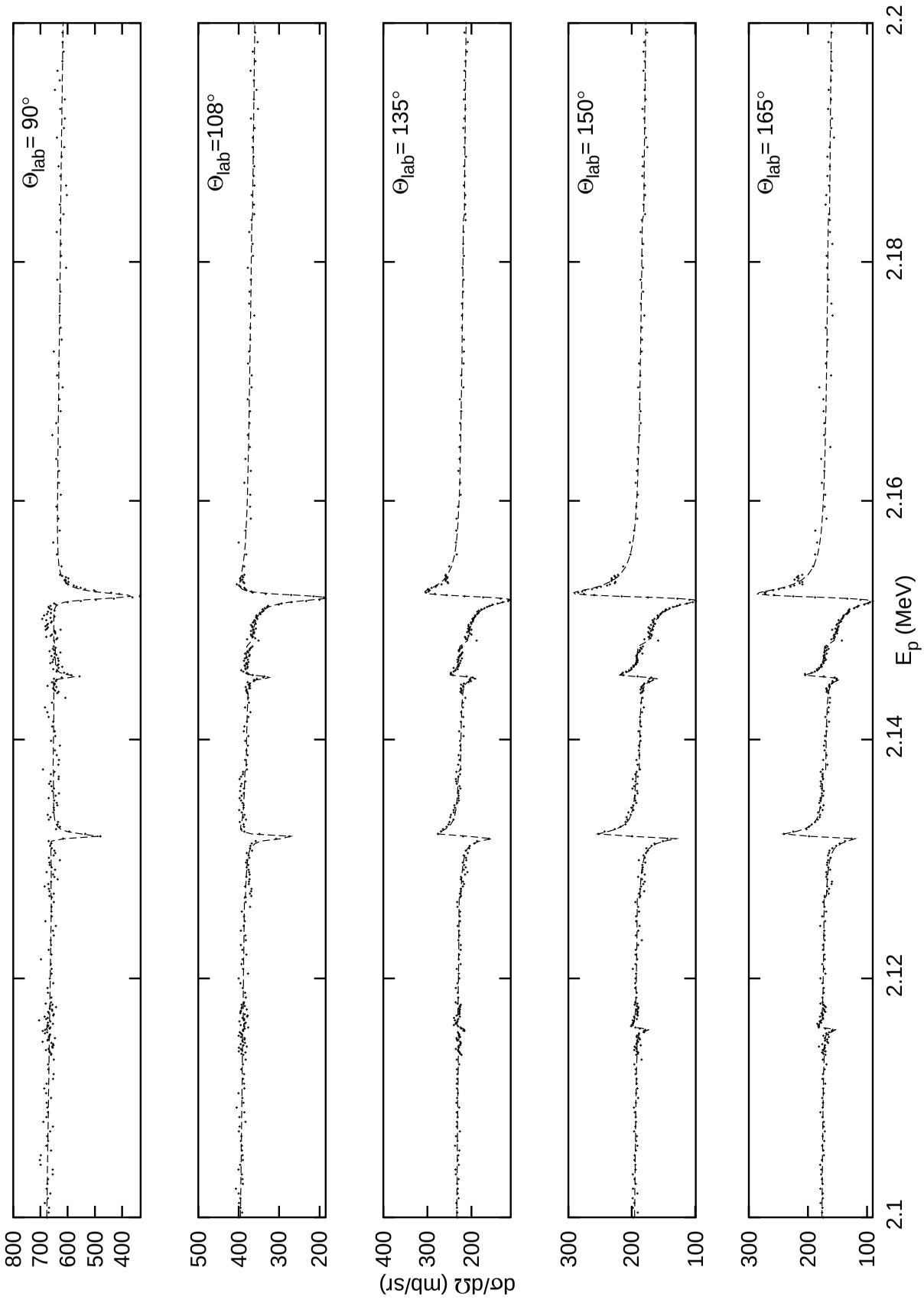

Figure A.1: The ^{52}Cr(p,p$_0$) reaction cross-section and fit for E$_p$= 2.1-2.2 MeV.

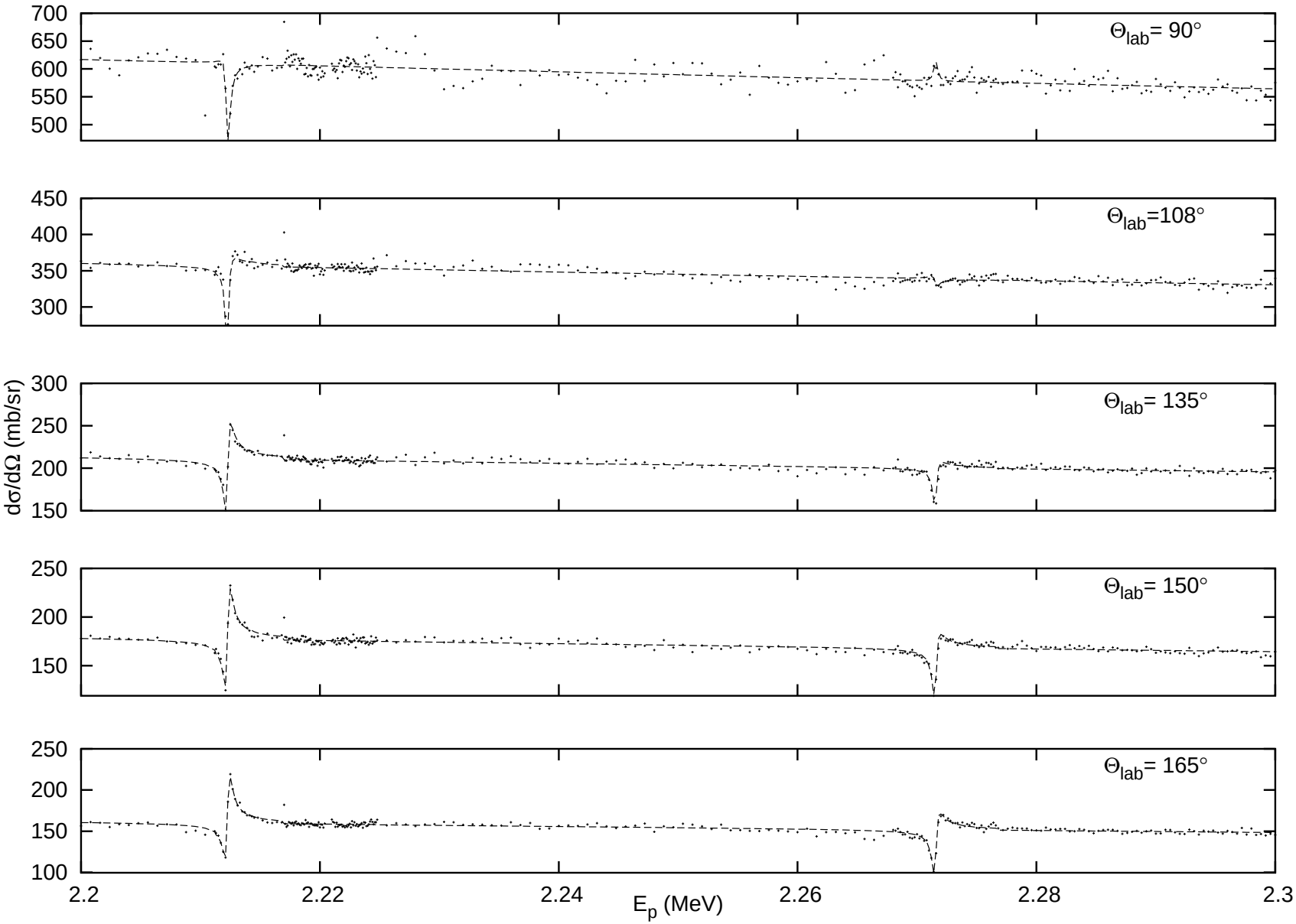

Figure A.2: The ^{52}Cr(p,p$_0$) reaction cross-section and fit for E$_p$= 2.2-2.3 MeV.

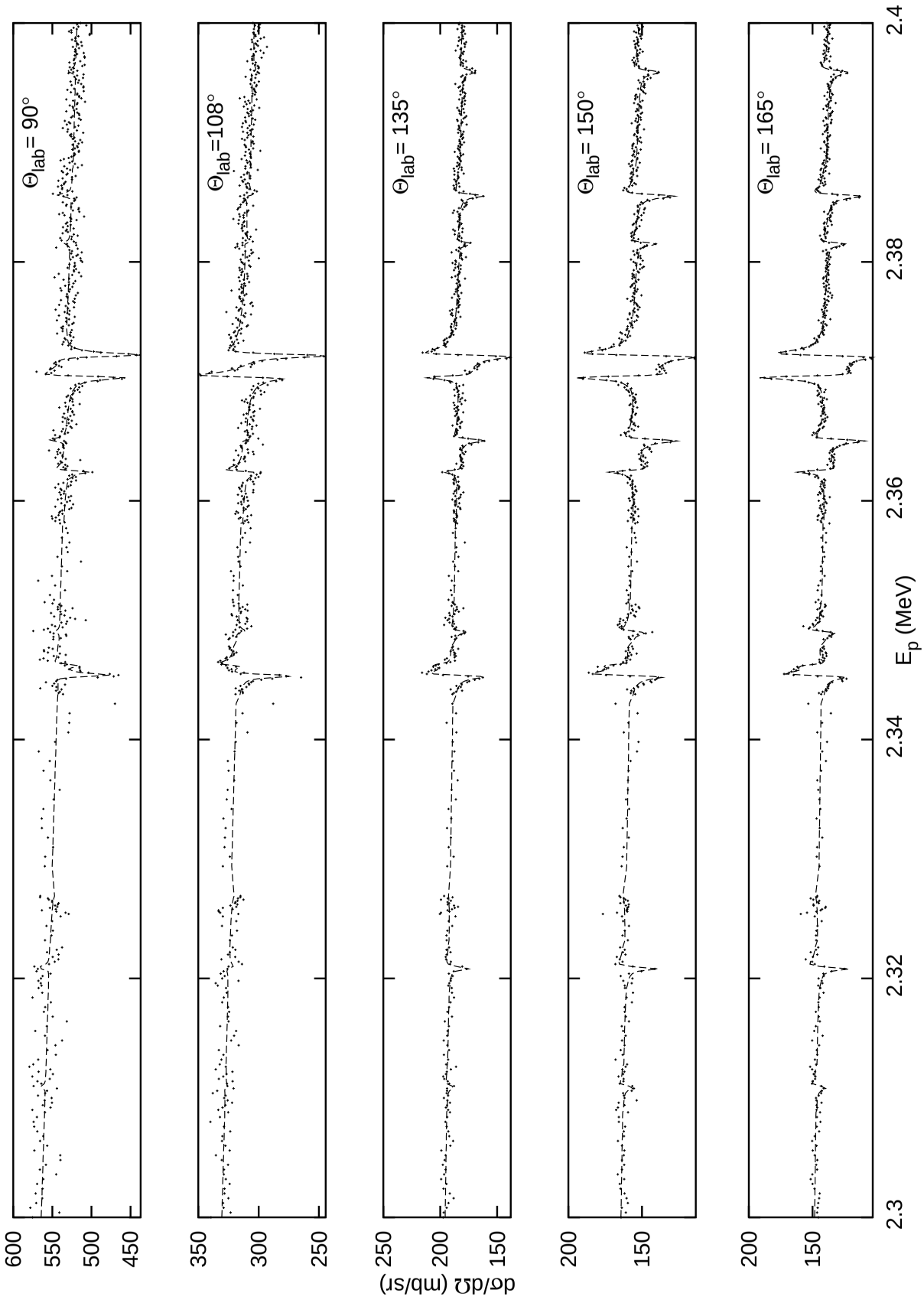

Figure A.3: The ^{52}Cr(p,p$_0$) reaction cross-section and fit for E$_p$= 2.3-2.4 MeV.

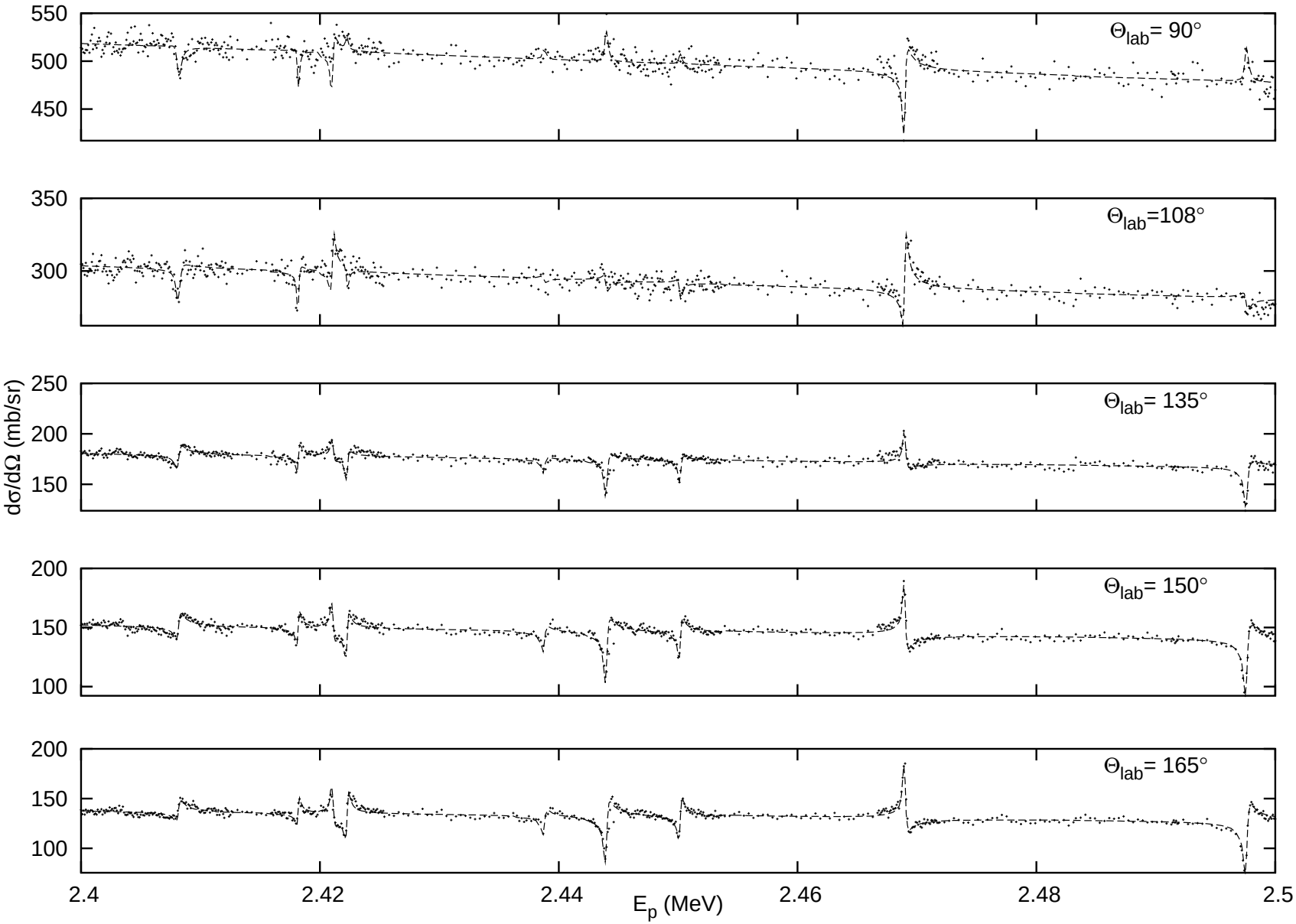

Figure A.4: The ^{52}Cr(p,p$_0$) reaction cross-section and fit for E$_p$= 2.4-2.5 MeV.

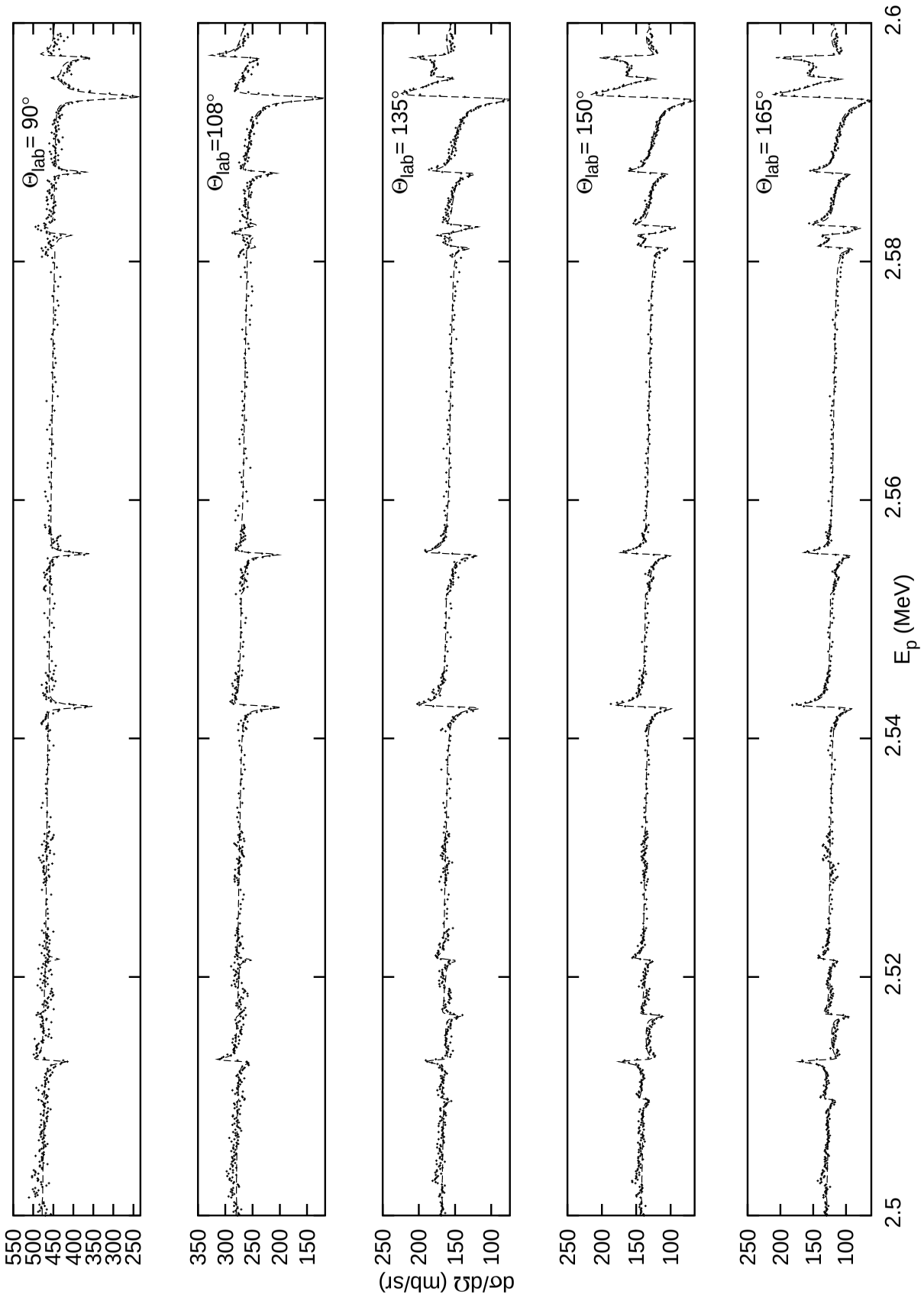

Figure A.5: The ^{52}Cr(p,p$_0$) reaction cross-section and fit for E$_p$= 2.5-2.6 MeV.

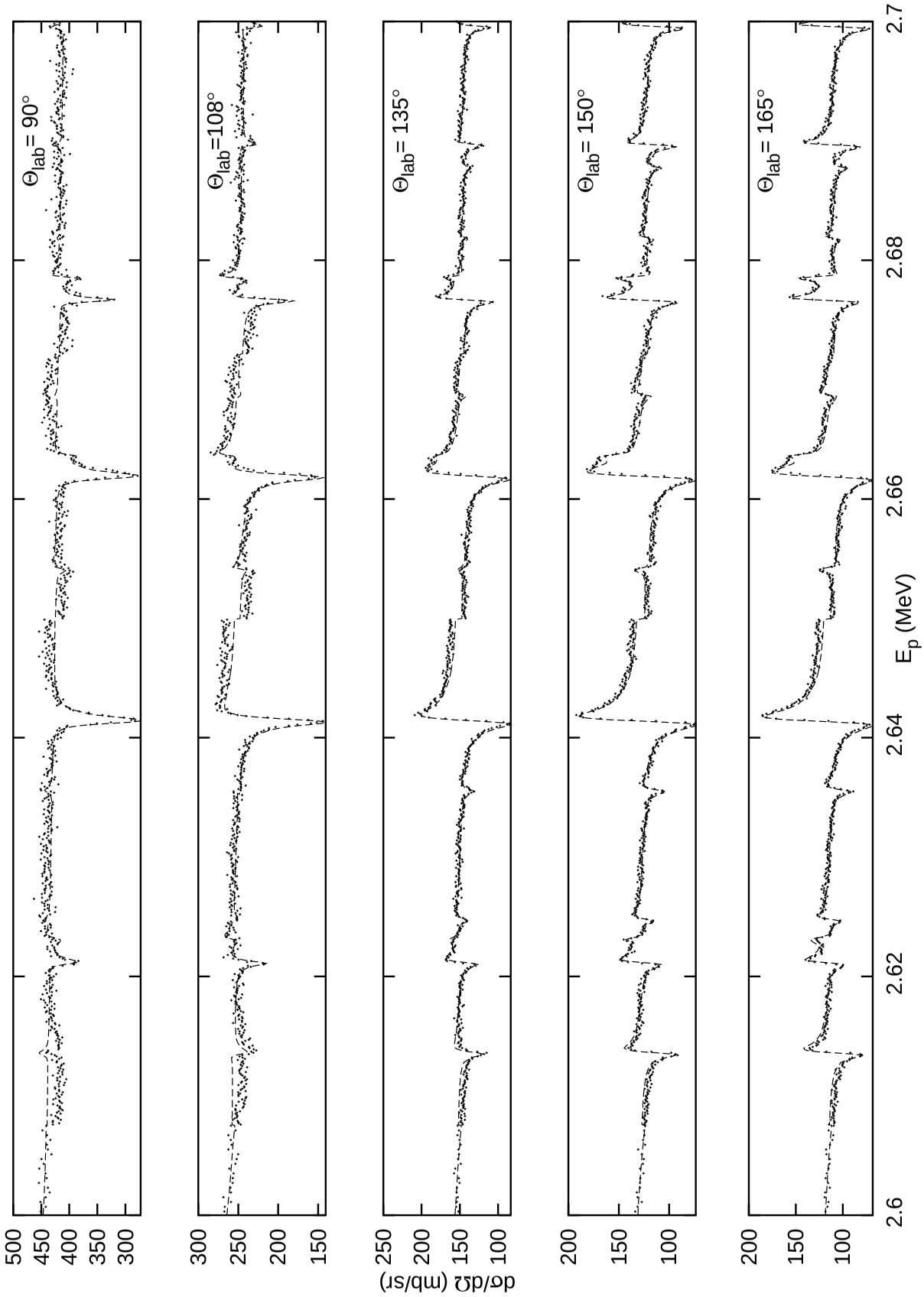

Figure A.6: The ^{52}Cr(p,p$_0$) reaction cross-section and fit for E$_p$= 2.6-2.7 MeV.

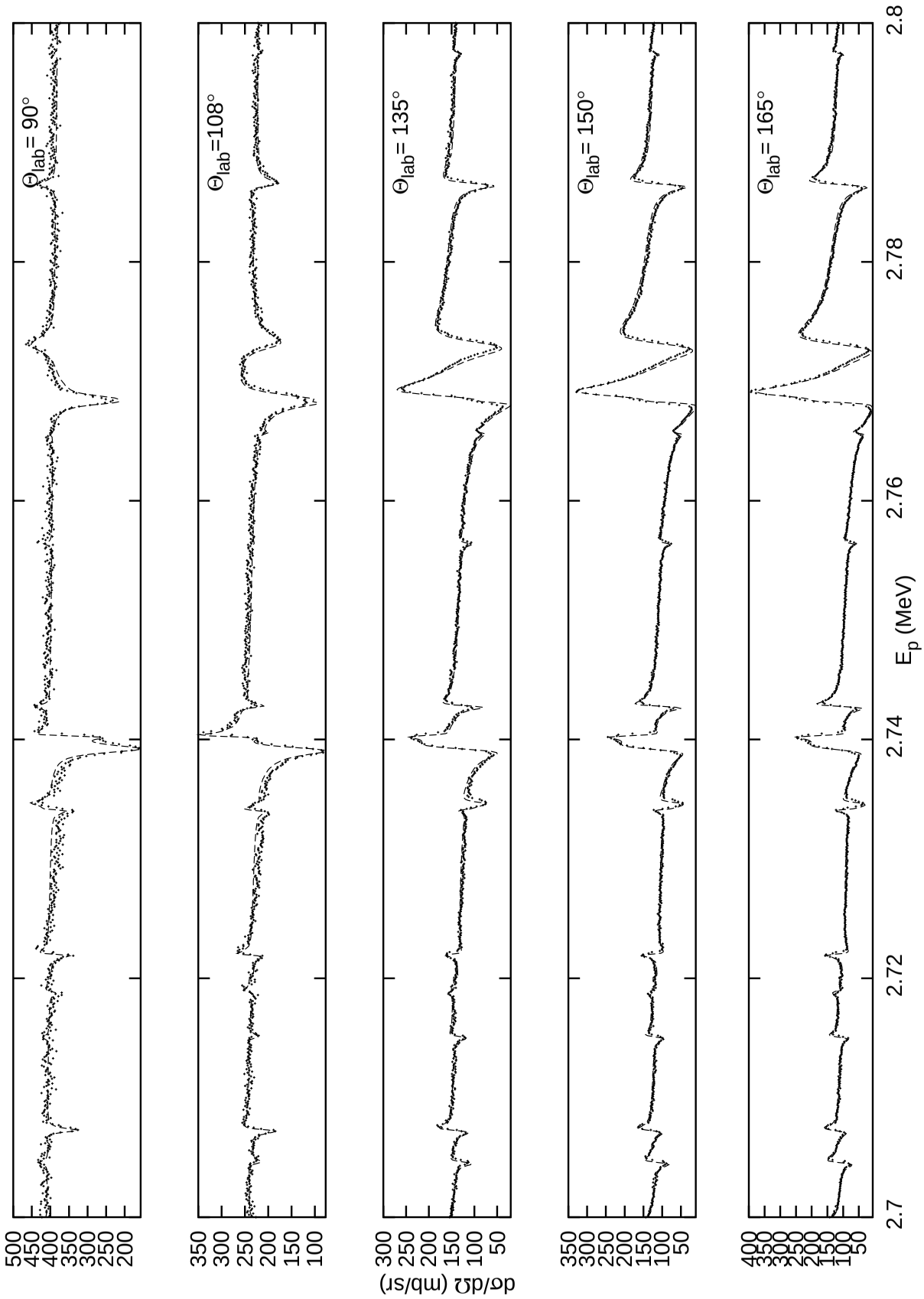

Figure A.7: The ^{52}Cr(p,p$_0$) reaction cross-section and fit for E$_p$= 2.7-2.8 MeV.

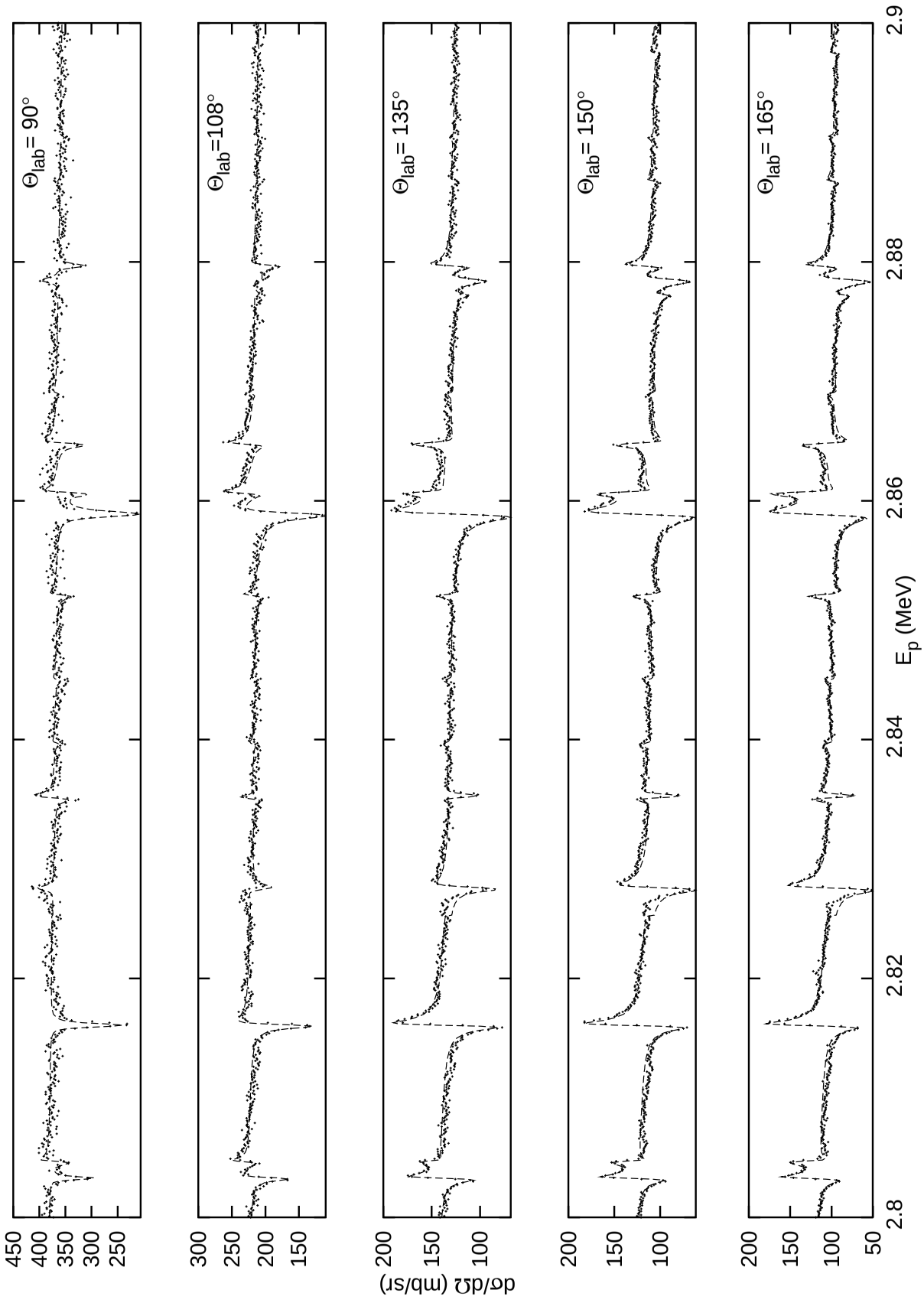

Figure A.8: The ^{52}Cr(p,p$_0$) reaction cross-section and fit for E$_p$= 2.8-2.9 MeV.

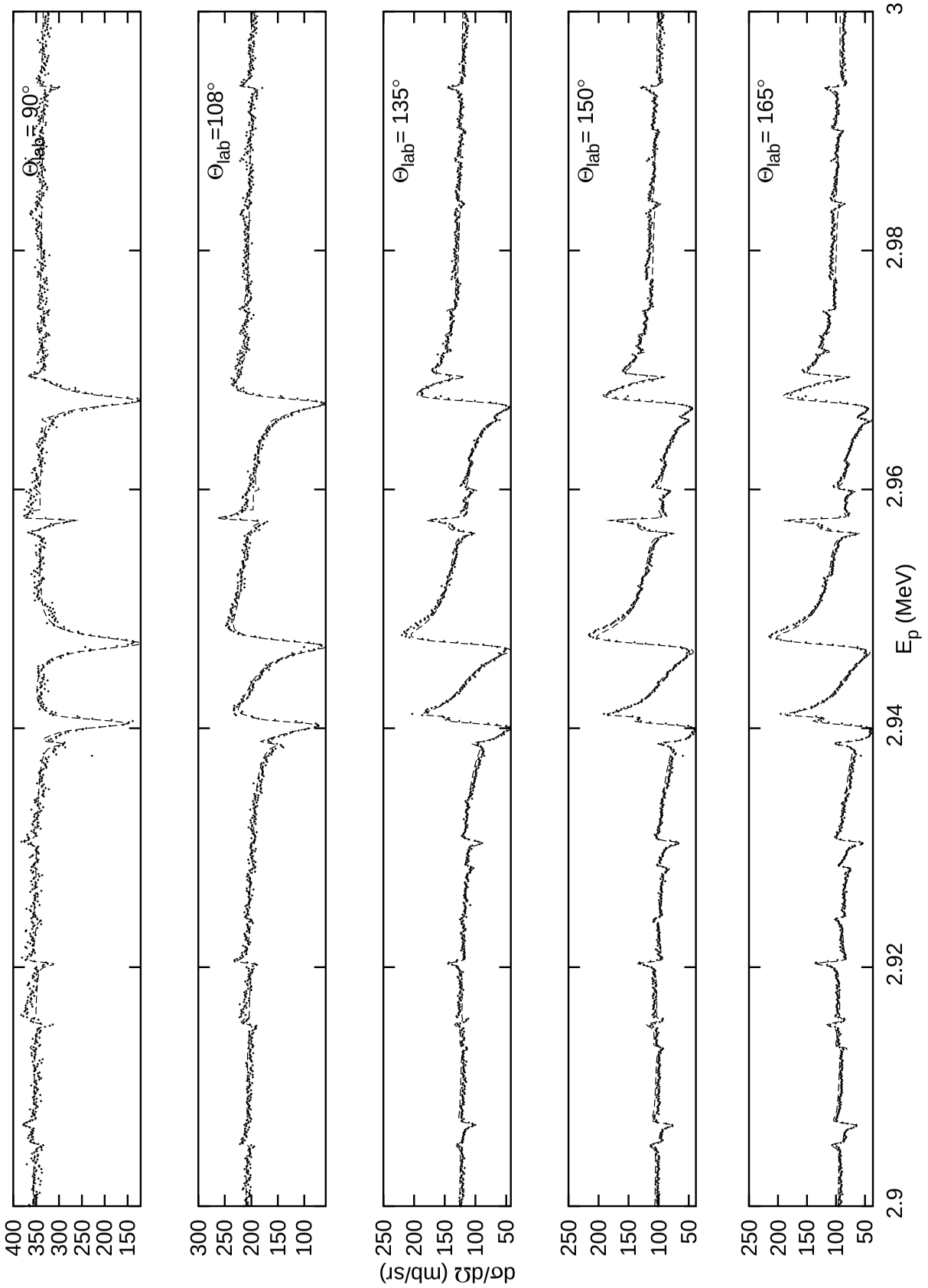

Figure A.9: The ^{52}Cr(p,p$_0$) reaction cross-section and fit for E$_p$= 2.9-3.0 MeV.

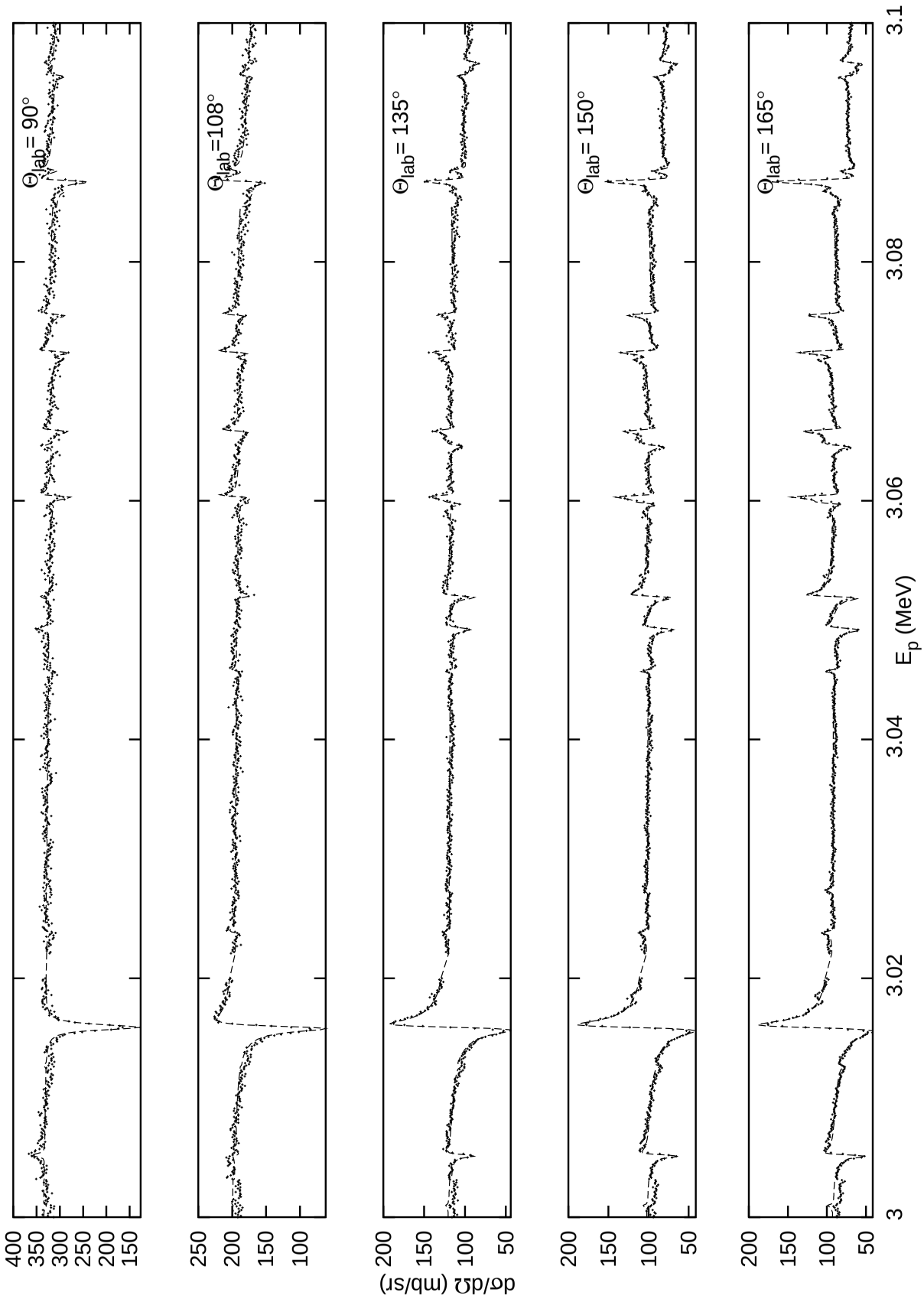

Figure A.10: The ^{52}Cr(p,p$_0$) reaction cross-section and fit for E$_p$= 3.0-3.1 MeV.

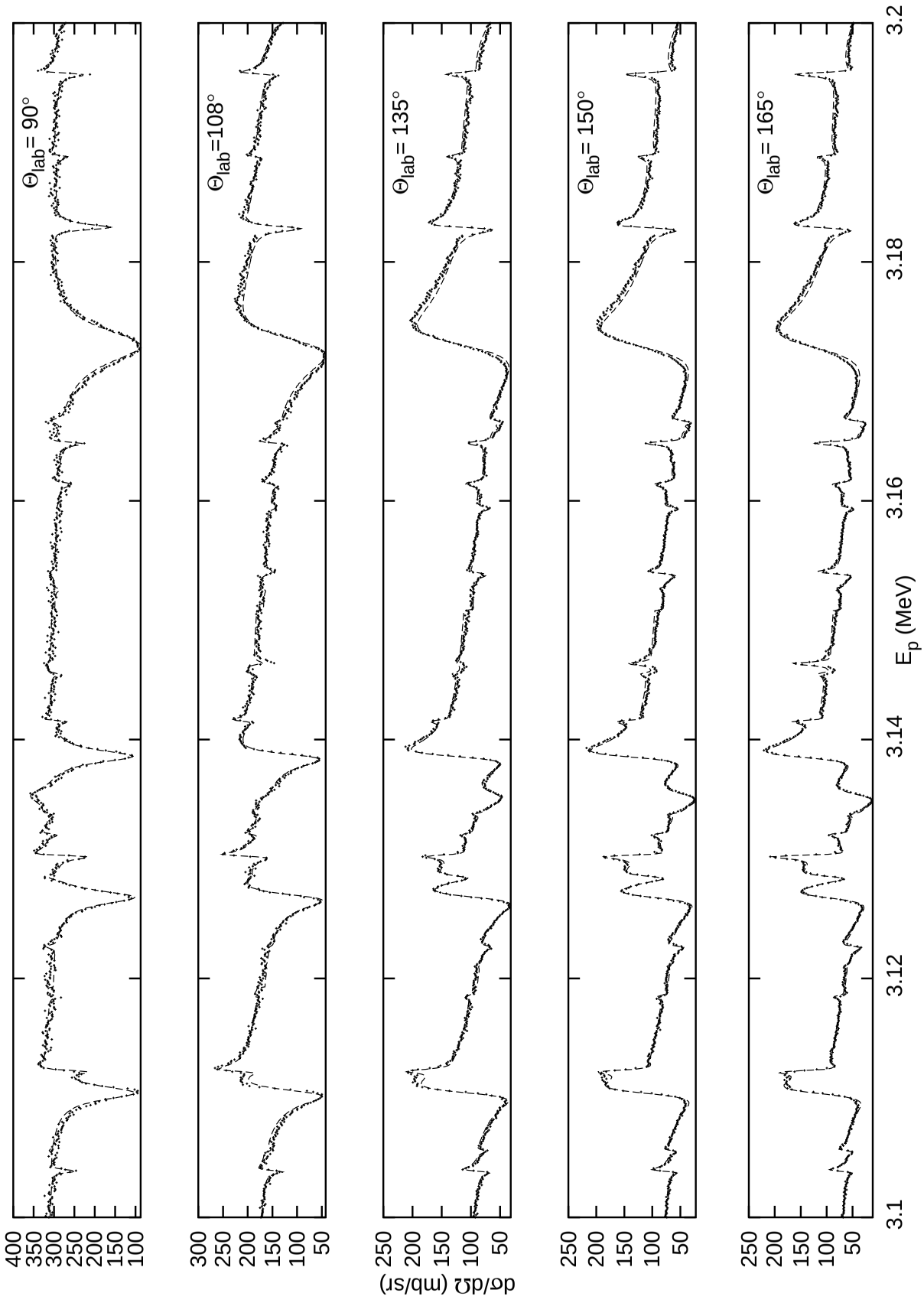

Figure A.11: The ^{52}Cr(p,p$_0$) reaction cross-section and fit for E$_p$= 3.1-3.2 MeV.

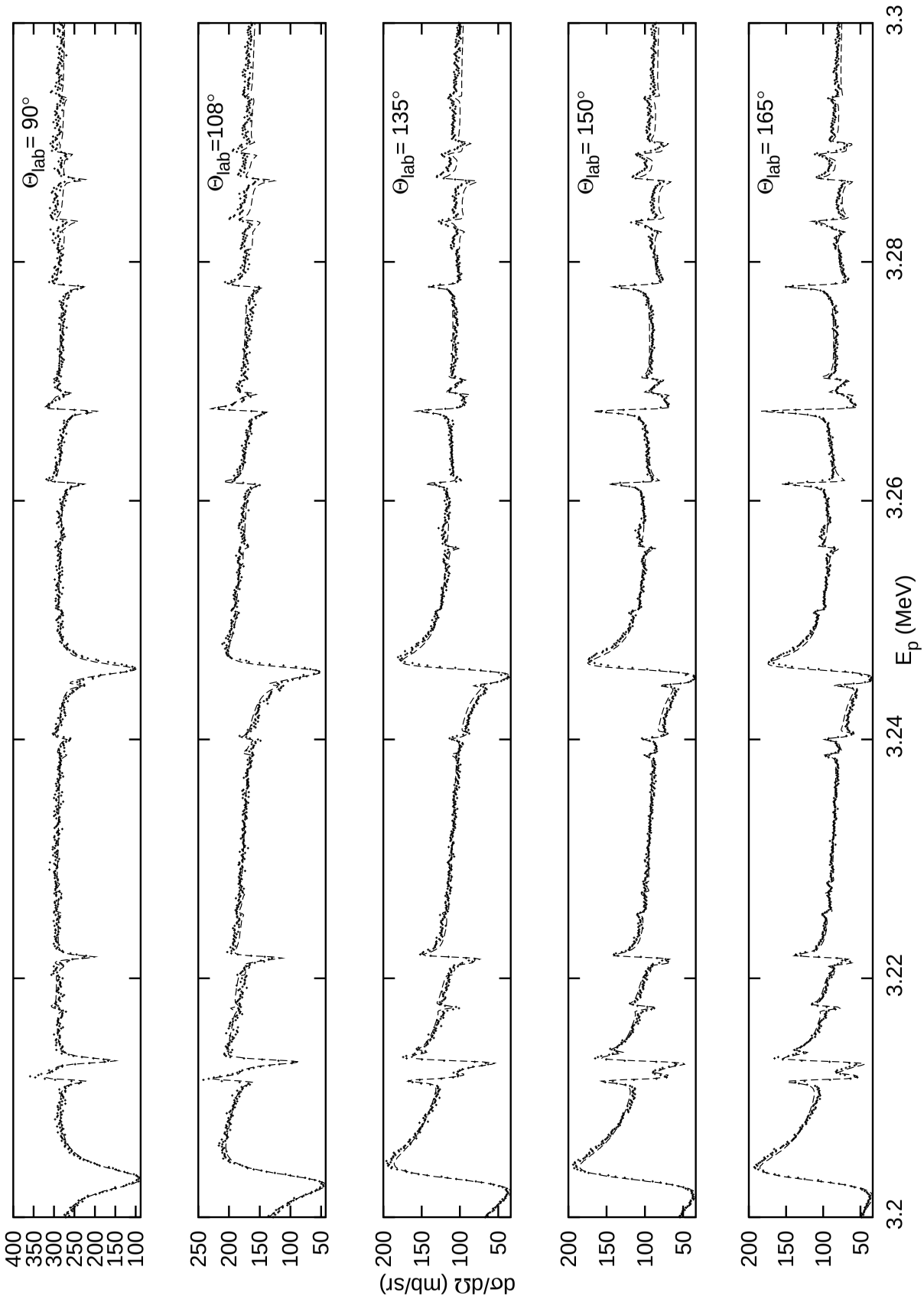

Figure A.12: The ^{52}Cr(p,p$_0$) reaction cross-section and fit for E$_p$= 3.2-3.3 MeV.

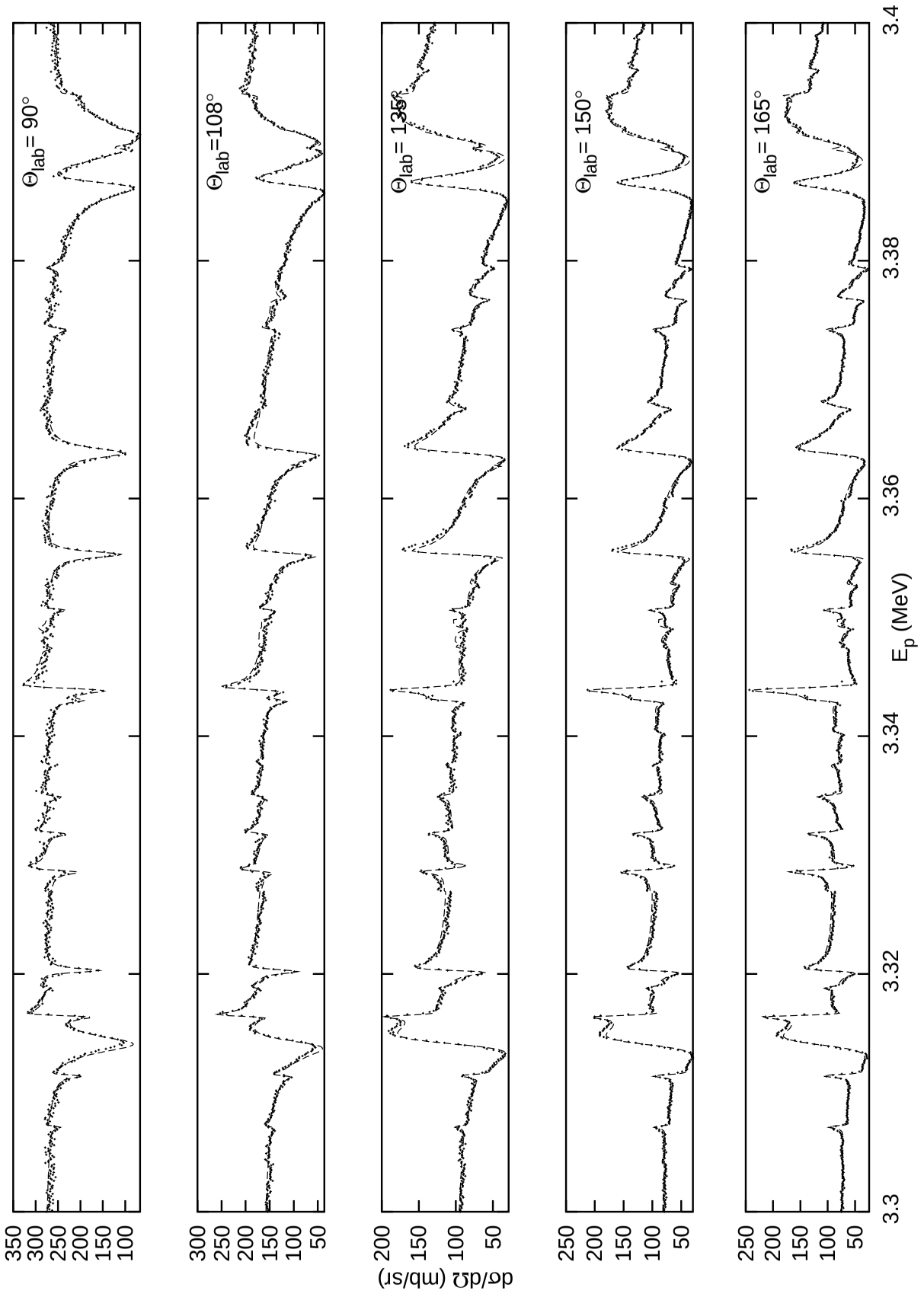

Figure A.13: The ^{52}Cr(p,p$_0$) reaction cross-section and fit for E$_p$= 3.3-3.4 MeV.

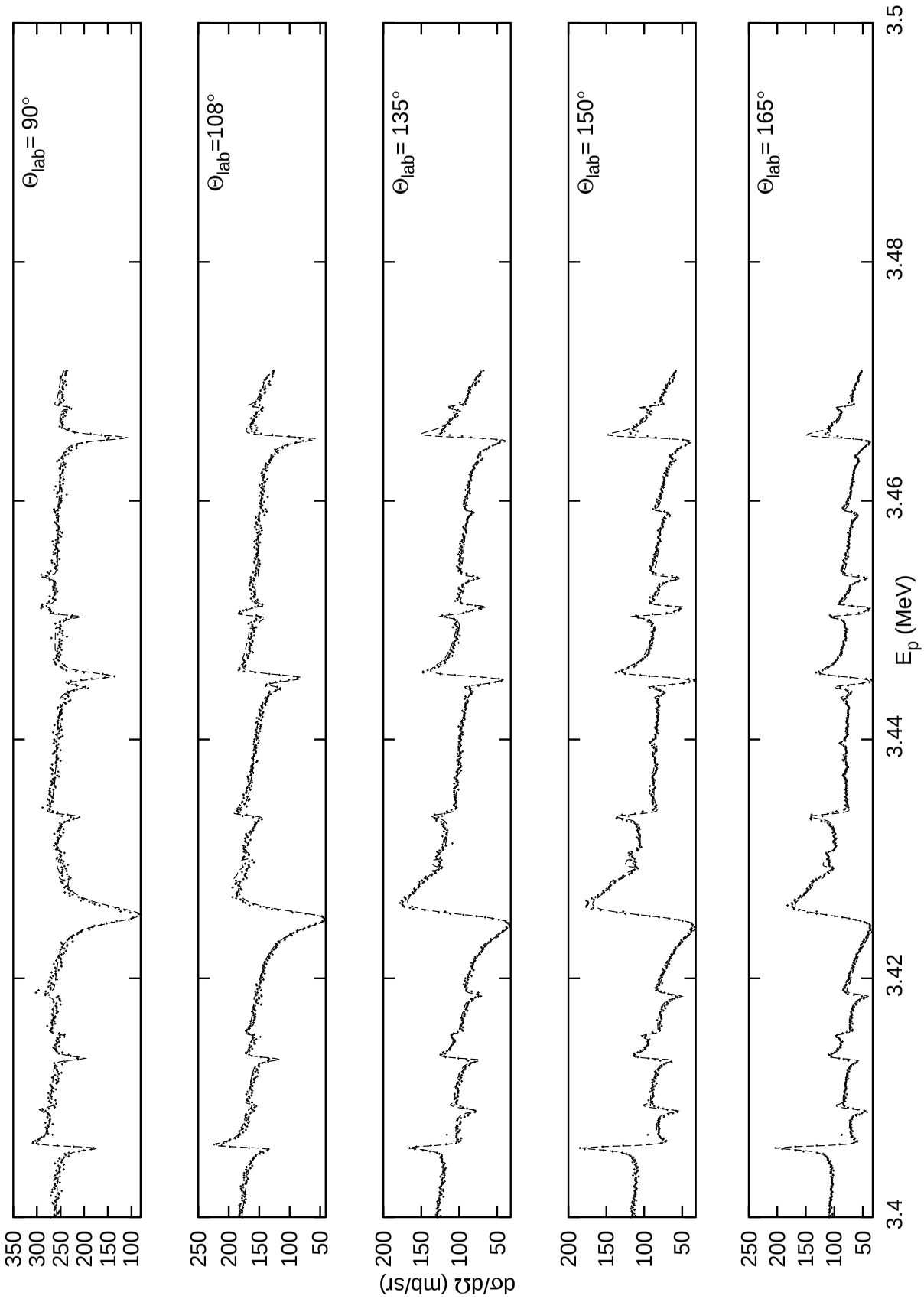

Figure A.14: The ^{52}Cr(p,p$_0$) reaction cross-section and fit for E$_p$= 3.4-3.5 MeV.

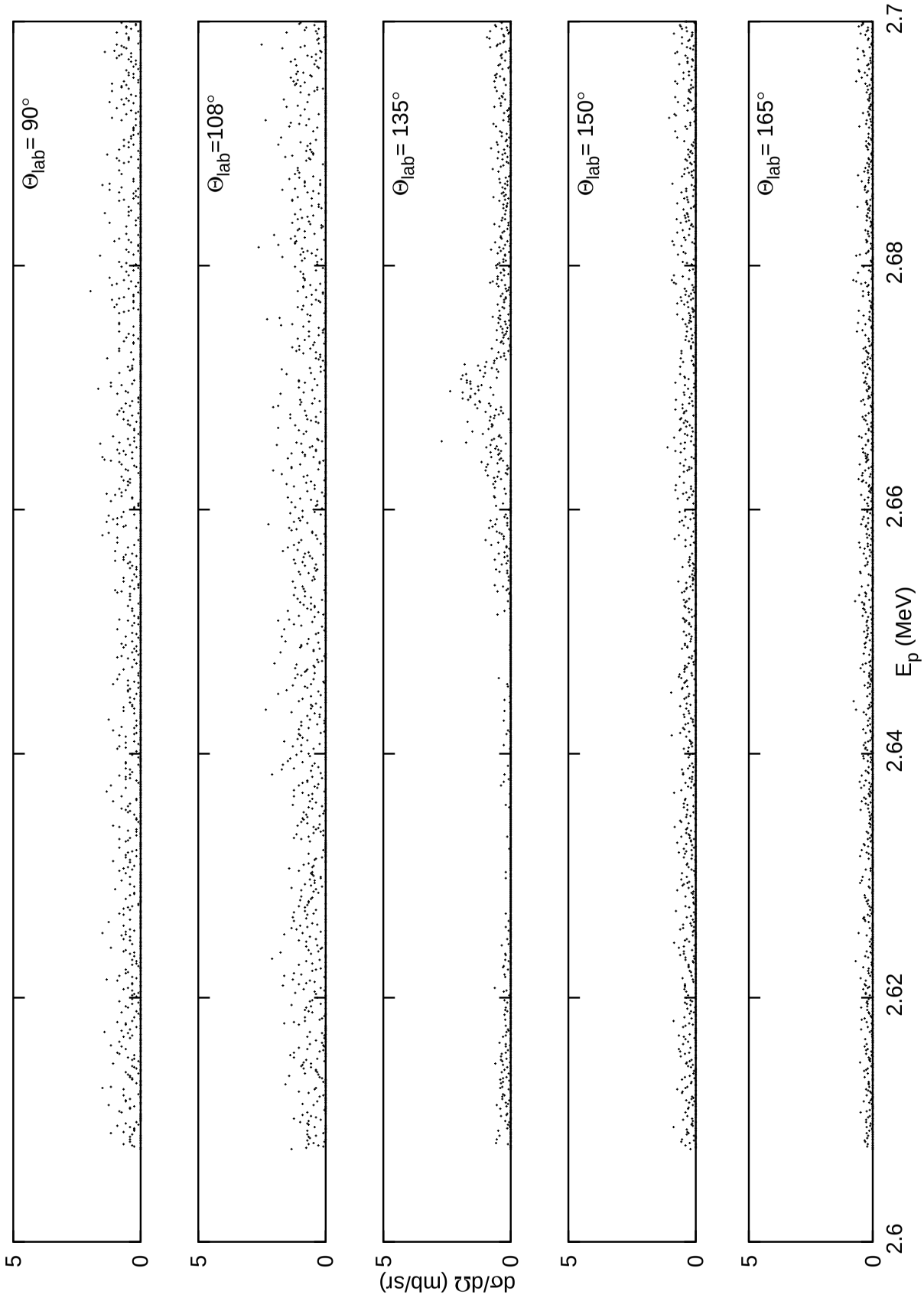

Figure A.15: The ^{52}Cr(p,p$_1$) reaction cross-section and fit for E$_p$= 2.6-2.7 MeV.

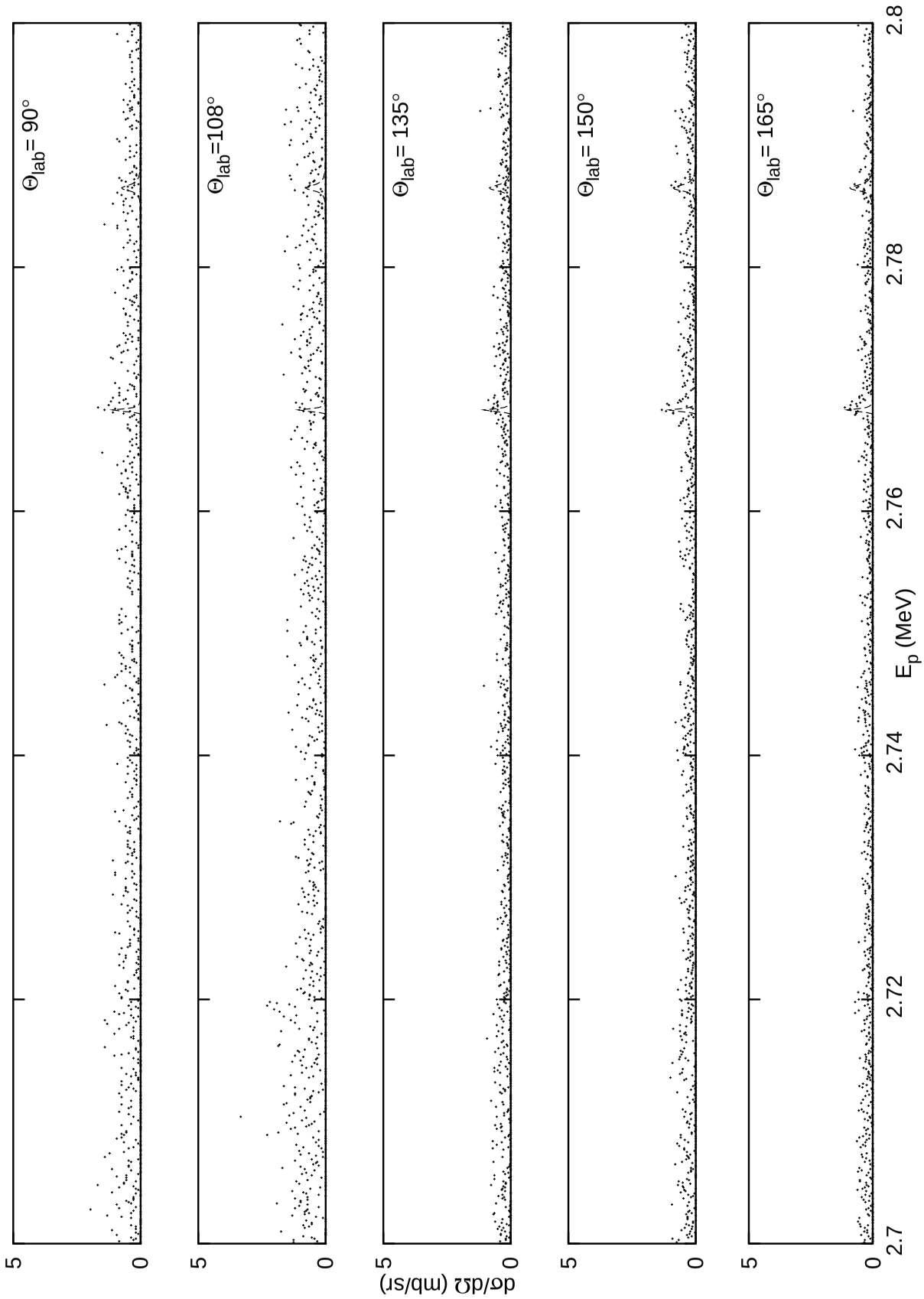

Figure A.16: The ^{52}Cr(p,p$_1$) reaction cross-section and fit for E$_p$= 2.7-2.8 MeV.

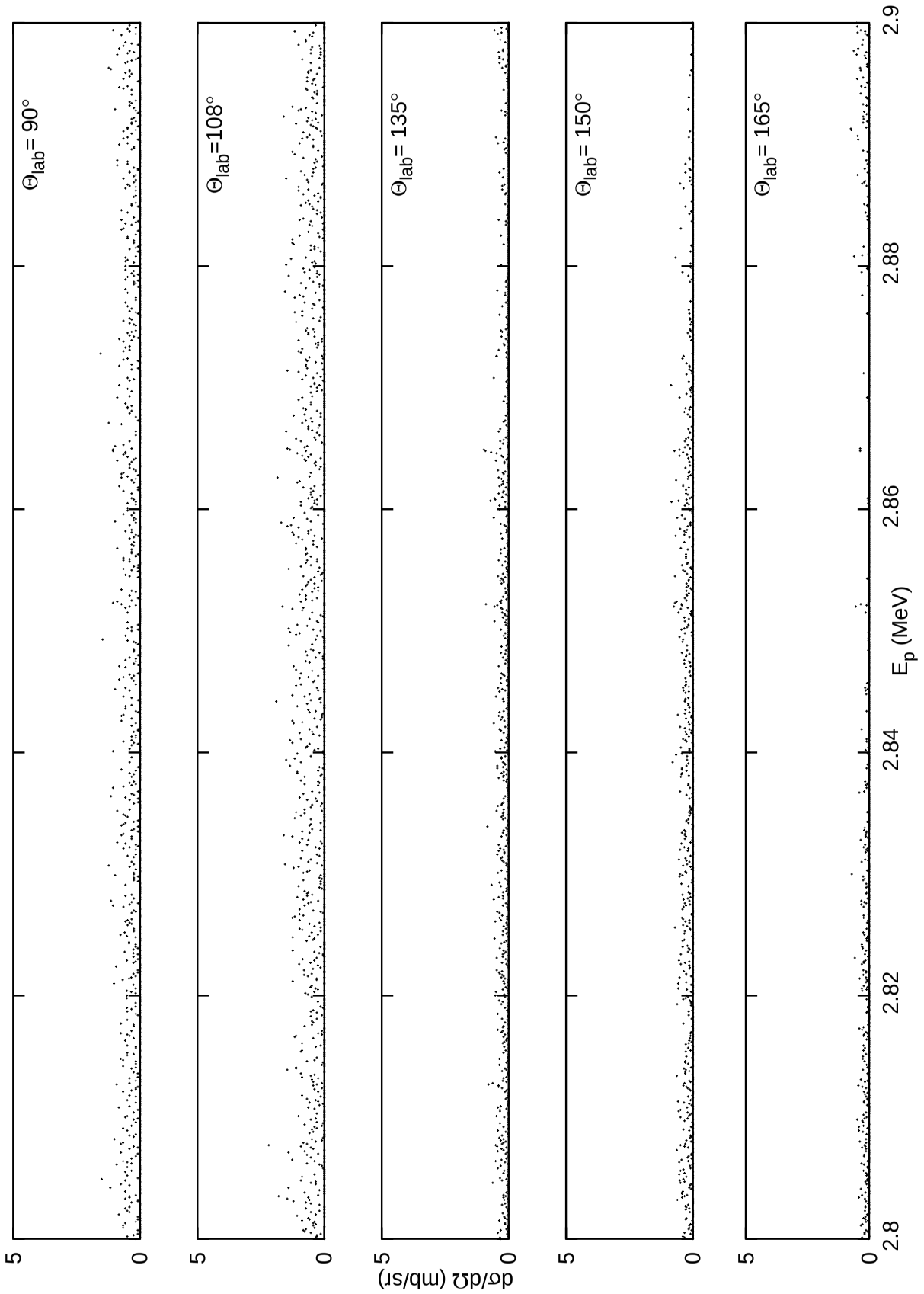

Figure A.17: The ^{52}Cr(p,p$_1$) reaction cross-section and fit for E$_p$= 2.8-2.9 MeV.

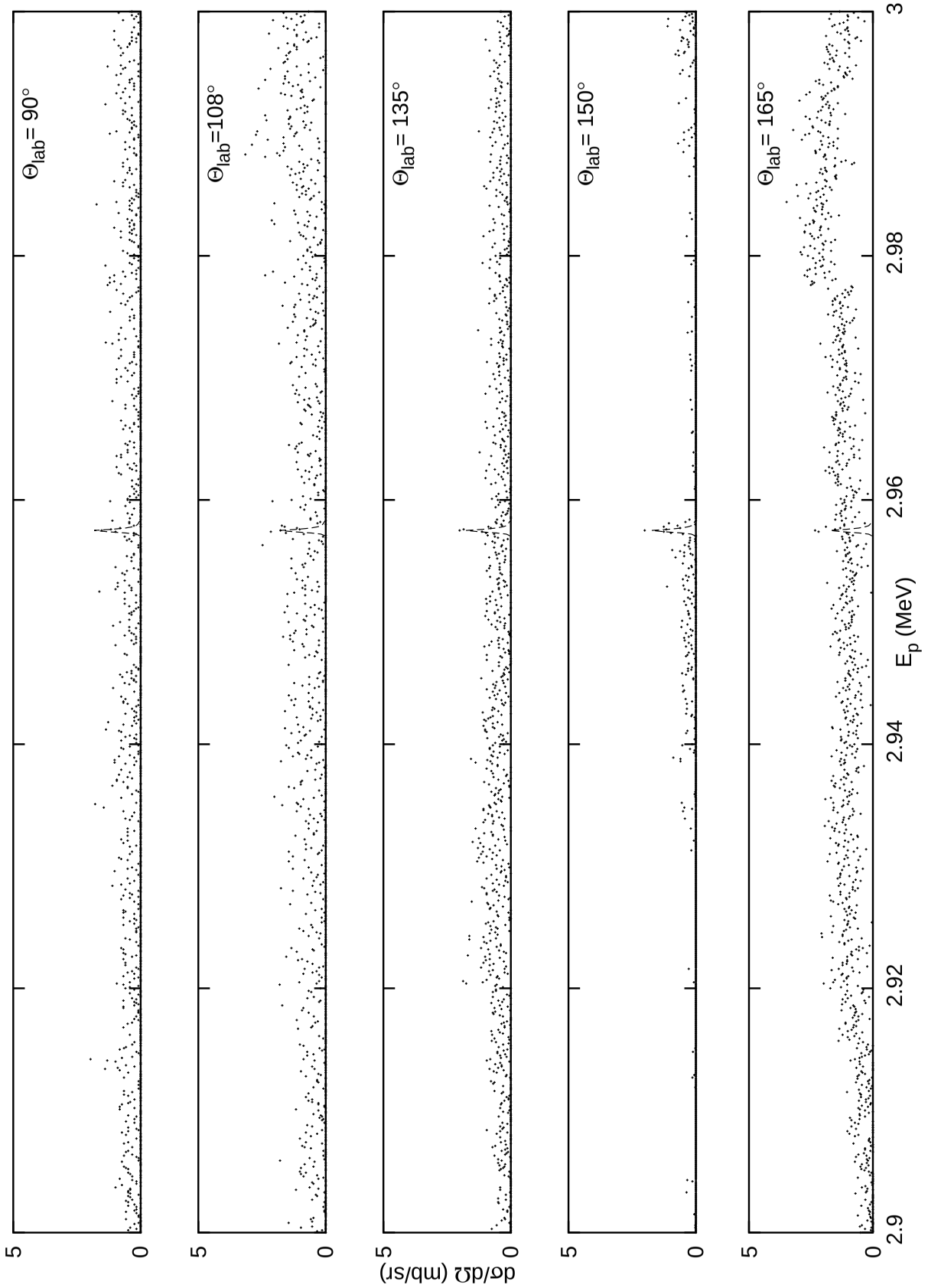

Figure A.18: The ^{52}Cr(p,p$_1$) reaction cross-section and fit for E$_p$= 2.9-3.0 MeV.

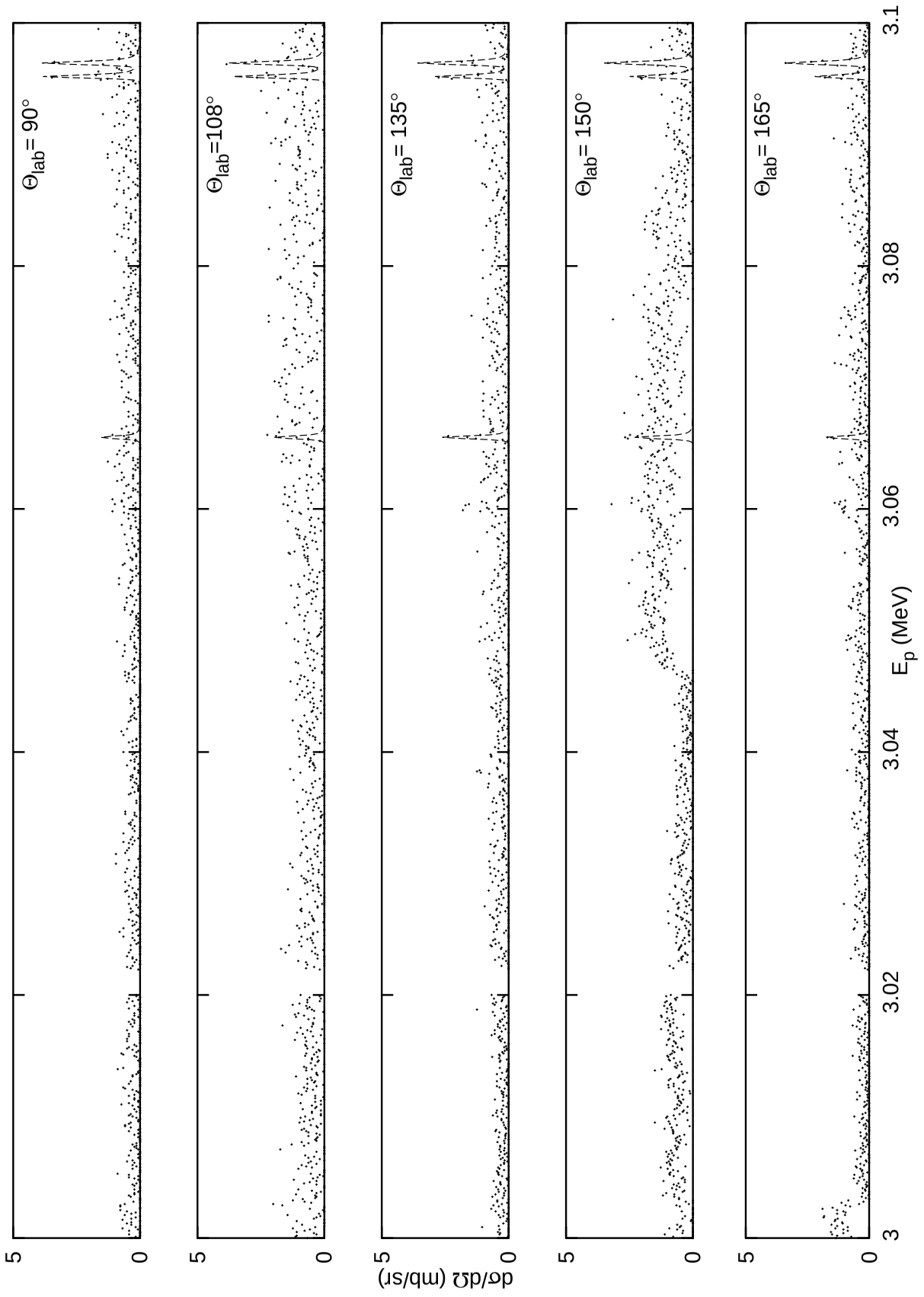

Figure A.19: The ^{52}Cr(p,p$_1$) reaction cross-section and fit for E$_p$= 3.0-3.1 MeV.

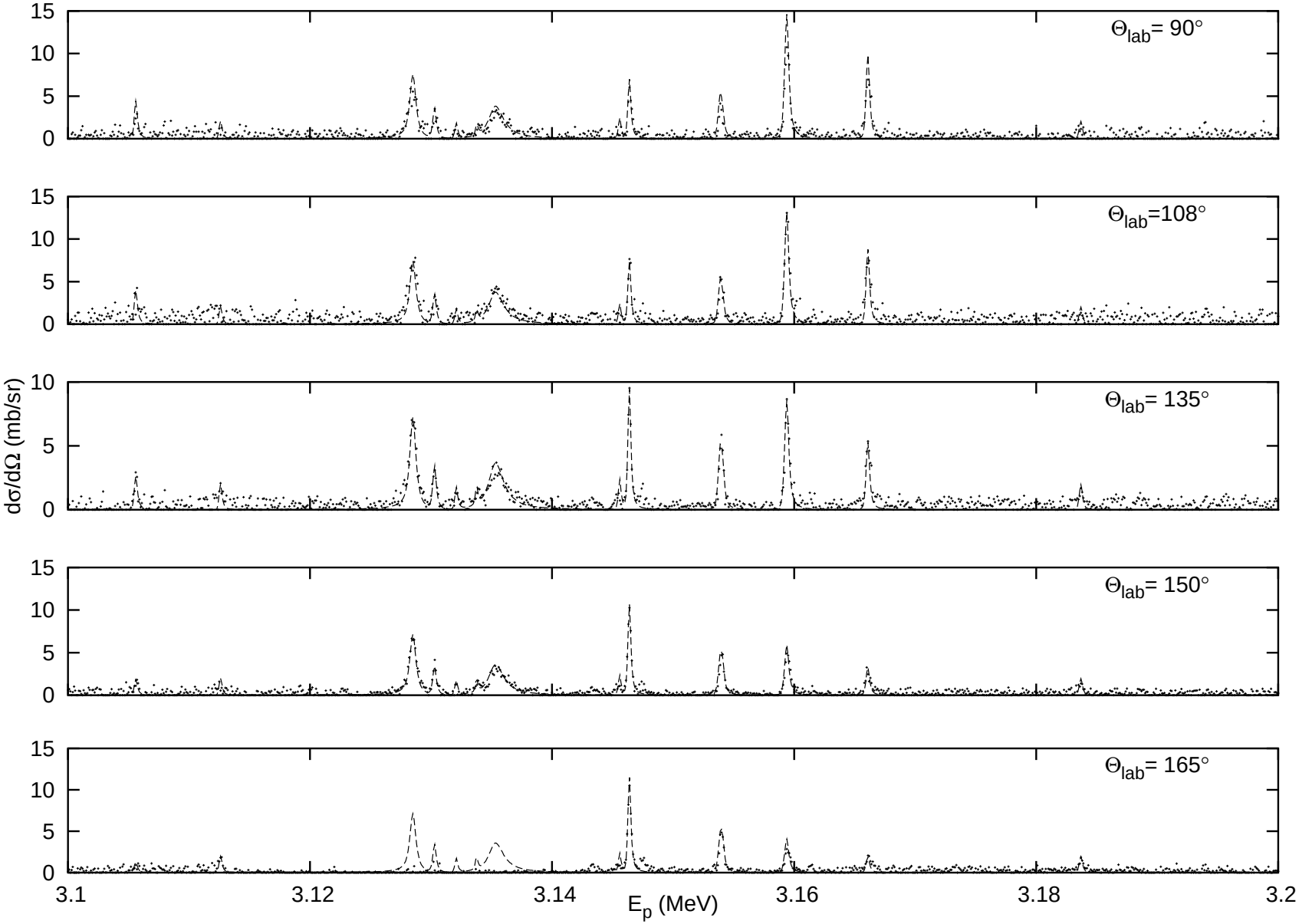

Figure A.20: The ^{52}Cr(p,p$_1$) reaction cross-section and fit for E_p= 3.1-3.2 MeV.

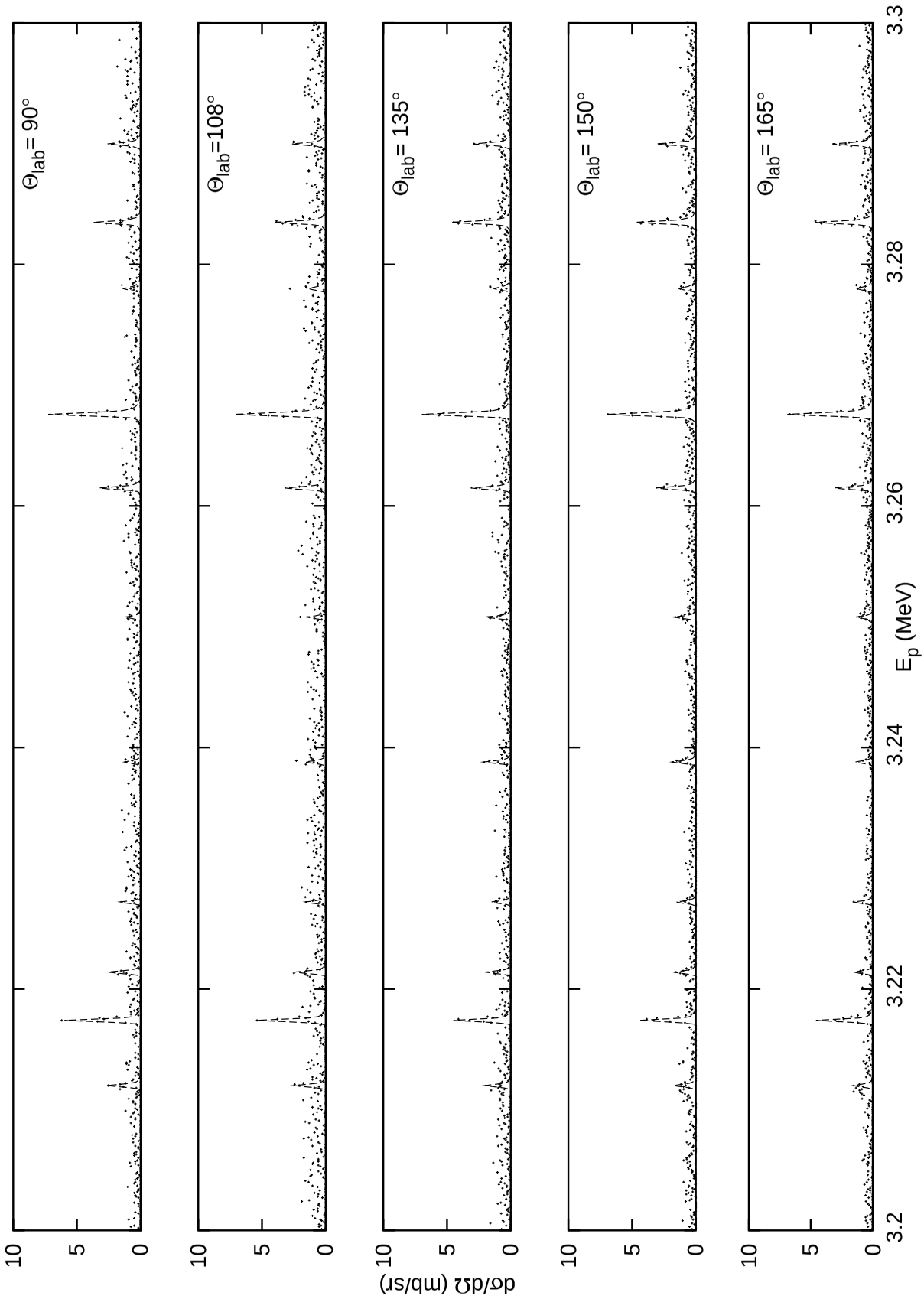

Figure A.21: The ^{52}Cr(p,p$_1$) reaction cross-section and fit for E$_p$= 3.2-3.3 MeV.

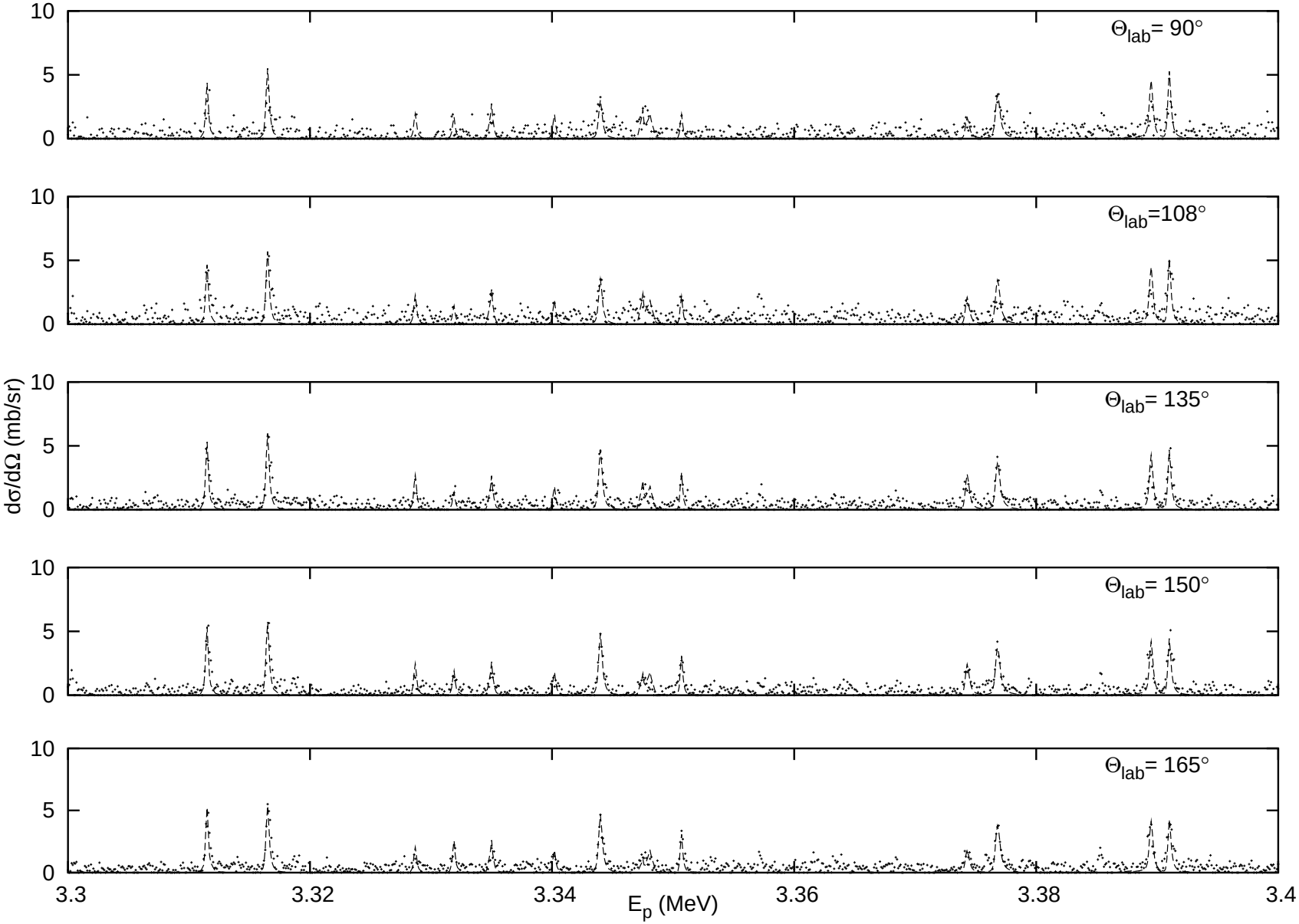

Figure A.22: The ^{52}Cr(p,p$_1$) reaction cross-section and fit for E$_p$= 3.3-3.4 MeV.

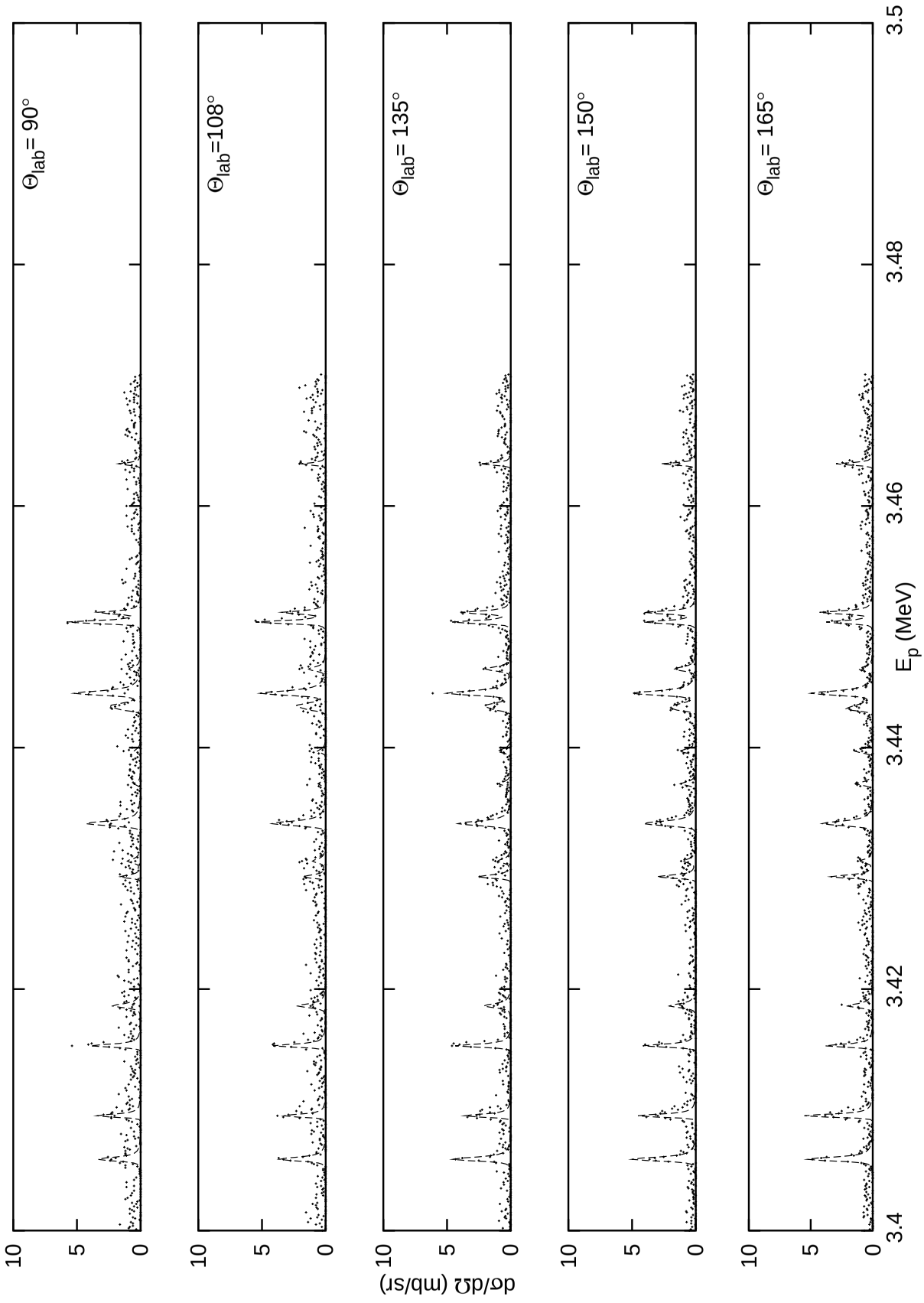

Figure A.23: The ^{52}Cr(p,p$_1$) reaction cross-section and fit for E$_p$= 3.4-3.5 MeV.

Appendix B

Resonance Parameters

This appendix contains the tabulated resonance parameters. First, a comprehensive listing for the current as well as the previous work of Moses [Mos70] is given. Subsequently, the resonance parameters for each of the specific J^{π} sequences as well as the $\ell = 2$ and $\ell = 3$ sequences are presented.

Table B.1: ^{53}Mn resonance parameters.

	Current Work								Previous Work			
Resonance Number	E_p (MeV)	J^π	Γ_p (eV)	γ_p^2 (keV)	s′	ℓ'	$\Gamma_{p'}$ (eV)	$\gamma_{p'}^2$ (keV)	E_p (MeV)	J^π	Γ_p (eV)	γ_p^2 (keV)
1	2.1197	$\frac{1}{2}^-$	30	1.89					2.1188	$\frac{1}{2}^-$	25	1.56
2	2.1358	$\frac{1}{2}^+$	140	3.58					2.1348	$\frac{1}{2}^+$	110	2.78
3	2.1491	$\frac{1}{2}^+$	50	1.22					2.1478	$\frac{1}{2}^+$	37	0.90
4	2.1558	$\frac{1}{2}^+$	400	9.58					2.1545	$\frac{1}{2}^+$	400	9.50
5	2.2160	$\frac{1}{2}^+$	125	2.48					2.2148	$\frac{1}{2}^+$	100	1.97
6†	2.2751	$\frac{1}{2}^-$	140	5.29					2.2212	$\frac{1}{2}^-$	110	4.13
7	2.3144	$\frac{1}{2}^-$	15	0.50					2.3126	$\frac{1}{2}^-$	10	0.32
8	2.3243	$\frac{1}{2}^-$	45	1.46					2.3231	$\frac{1}{2}^-$	32	1.00
9	2.3311	$\frac{5}{2}^+$	14	2.12					2.3301	$\frac{5}{2}^+$	4	0.58
10	2.3487	$\frac{1}{2}^+$	45	0.61					2.3474	$\frac{1}{2}^+$	45	0.59
11	2.3496	$\frac{3}{2}^+$	15	2.14					2.3484	$\frac{1}{2}^+$	15	2.06
12	2.3524	$\frac{3}{2}^-$	15	0.45					2.3509	$\frac{1}{2}^-$	10	0.29

Table B.1: ^{53}Mn resonance parameters (*continued*)

Current Work									Previous Work			
Resonance Number	E_p (MeV)	J^π	Γ_p (eV)	γ_p^2 (keV)	s′	ℓ'	$\Gamma_{p'}$ (eV)	$\gamma_{p'}^2$ (keV)	E_p (MeV)	J^π	Γ_p (eV)	γ_p^2 (keV)
13	2.3657	$\frac{5}{2}^+$	15	2.03					2.3645	$\frac{5}{2}^+$	5	0.65
14	2.3683	$\frac{1}{2}^-$	65	1.86					2.3670	$\frac{1}{2}^-$	50	1.38
15	2.3736	$\frac{5}{2}^+$	43	5.68					2.3722	$\frac{5}{2}^+$	35	4.47
16	2.3754	$\frac{1}{2}^+$	90	1.13					2.3740	$\frac{1}{2}^+$	70	0.85
17	2.3848	$\frac{1}{2}^-$	26	0.71					2.3873	$\frac{1}{2}^-$	50	1.30
18	2.3888	$\frac{1}{2}^-$	60	1.62					n/o			
19	2.3992	$\frac{1}{2}^-$	40	1.05					2.3975	$\frac{1}{2}^-$	20	0.51
20	2.4113	$\frac{1}{2}^+$	30	0.34					2.4093	$\frac{1}{2}^+$	25	0.29
21	2.4213	$\frac{1}{2}^+$	20	0.22					2.4192	$\frac{1}{2}^-$	20	0.49
22	2.4242	$\frac{5}{2}^+$	20	2.26					2.4223	$\frac{5}{2}^+$	5	0.57
23	2.4254	$\frac{3}{2}^-$	32	0.78					2.4235	$\frac{1}{2}^-$	75	1.82
24	2.4418	$\frac{1}{2}^-$	40	0.93					2.4401	$\frac{1}{2}^-$	40	0.93
25	2.4470	$\frac{1}{2}^-$	110	2.52					2.4454	$\frac{1}{2}^-$	100	2.29

Table B.1: ^{53}Mn resonance parameters (*continued*)

	Current Work								Previous Work			
Resonance Number	E_p (MeV)	J^π	Γ_p (eV)	γ_p^2 (keV)	s′	ℓ'	$\Gamma_{p'}$ (eV)	$\gamma_{p'}^2$ (keV)	E_p (MeV)	J^π	Γ_p (eV)	γ_p^2 (keV)
26	2.4532	$\frac{3}{2}^-$	30	0.68					2.4515	$\frac{3}{2}^-$	30	0.68
27	2.4720	$\frac{5}{2}^+$	40	3.91					2.4707	$\frac{5}{2}^+$	30	2.94
28	2.5005	$\frac{1}{2}^-$	150	2.99					2.4991	$\frac{1}{2}^-$	105	2.09
29	2.5125	$\frac{1}{2}^-$	25	0.48					2.5108	$\frac{1}{2}^-$	30	0.58
30	2.5158	$\frac{5}{2}^+$	30	2.58					2.5142	$\frac{5}{2}^+$	30	2.59
31	2.5196	$\frac{1}{2}^-$	55	1.04					2.5178	$\frac{1}{2}^-$	50	0.95
32	2.5243	$\frac{1}{2}^+$	25	0.22					2.5227	$\frac{1}{2}^+$	20	0.17
33	2.5455	$\frac{1}{2}^+$	95	0.78					2.5438	$\frac{1}{2}^+$	95	0.78
34	2.5582	$\frac{1}{2}^+$	75	0.60					2.5569	$\frac{1}{2}^+$	75	0.60
35	2.5839	$\frac{3}{2}^-$	40	0.65					2.5828	$\frac{3}{2}^-$	40	0.64
36	2.5850	$\frac{3}{2}^+$	32	2.27					2.5837	$\frac{3}{2}^+$	10	0.71
37	2.5857	$\frac{3}{2}^-$	60	0.96					2.5845	$\frac{3}{2}^-$	60	0.96
38	2.5901	$\frac{1}{2}^+$	60	0.45					2.5890	$\frac{1}{2}^+$	60	0.44

Table B.1: ^{53}Mn resonance parameters (*continued*)

Current Work									Previous Work			
Resonance Number	E_p (MeV)	J^π	Γ_p (eV)	γ_p^2 (keV)	s′	ℓ'	$\Gamma_{p'}$ (eV)	$\gamma_{p'}^2$ (keV)	E_p (MeV)	J^π	Γ_p (eV)	γ_p^2 (keV)
39	2.5964	$\frac{1}{2}^+$	320	2.35					2.5953	$\frac{1}{2}^+$	300	2.19
40	2.5980	$\frac{1}{2}^-$	80	1.25					2.5969	$\frac{1}{2}^-$	50	0.78
41	2.5998	$\frac{5}{2}^+$	55	3.74					2.5986	$\frac{5}{2}^+$	55	3.75
42	2.6162	$\frac{3}{2}^-$	100	1.49					2.6161	$\frac{3}{2}^-$	70	1.04
43	2.6237	$\frac{1}{2}^+$	75	0.52					2.6236	$\frac{1}{2}^+$	50	0.34
44	2.6257	$\frac{5}{2}^+$	17	1.08					n/o			
45	2.6273	$\frac{3}{2}^-$	33	0.48					n/o			
46	2.6381	$\frac{1}{2}^-$	75	1.06					2.6367	$\frac{1}{2}^-$	50	0.71
47	2.6439	$\frac{1}{2}^+$	375	2.48					2.6425	$\frac{1}{2}^+$	300	1.98
48	2.6567	$\frac{5}{2}^+$	16	0.93					2.6548	$\frac{5}{2}^+$	10	0.59
49	2.6643	$\frac{1}{2}^+$	325	2.06					2.6627	$\frac{1}{2}^+$	275	1.73
50	2.6661	$\frac{5}{2}^+$	25	1.42					2.6642	$\frac{5}{2}^+$	15	0.86
51	2.6711	$\frac{3}{2}^-$	25	0.33					2.6691	$\frac{1}{2}^-$	15	0.20

Table B.1: ^{53}Mn resonance parameters (*continued*)

Current Work									Previous Work			
Resonance Number	E_p (MeV)	J^π	Γ_p (eV)	γ_p^2 (keV)	s′	ℓ'	$\Gamma_{p'}$ (eV)	$\gamma_{p'}^2$ (keV)	E_p (MeV)	J^π	Γ_p (eV)	γ_p^2 (keV)
52	2.6791	$\frac{1}{2}^+$	110	0.67					2.6774	$\frac{1}{2}^+$	100	0.61
53	2.6810	$\frac{5}{2}^+$	25	1.37					2.6792	$\frac{5}{2}^+$	10	0.55
54	2.6843	$\frac{3}{2}^-$	15	0.19					n/o			
55	2.6902	$\frac{1}{2}^-$	30	0.38					2.6885	$\frac{1}{2}^-$	25	0.31
56	2.6921	$\frac{3}{2}^-$	70	0.87					2.6904	$\frac{3}{2}^-$	50	0.62
57	2.7019	$\frac{3}{2}^-$	90	1.10					2.7002	$\frac{1}{2}^-$	125	1.53
58	2.7069	$\frac{3}{2}^-$	100	1.21					2.7054	$\frac{3}{2}^-$	75	0.91
59	2.7085	$\frac{5}{2}^+$	5	0.26					n/o			
60	2.7096	$\frac{1}{2}^+$	95	0.55					2.7080	$\frac{1}{2}^+$	75	0.43
61	2.7174	$\frac{3}{2}^-$	70	0.83					2.7157	$\frac{3}{2}^-$	50	0.59
62	2.7212	$\frac{5}{2}^+$	15	0.74					2.7196	$\frac{3}{2}^+$	25	1.24
63	2.7245	$\frac{5}{2}^+$	35	1.72					2.7227	$\frac{5}{2}^+$	50	2.47
64	2.7363	$\frac{5}{2}^+$	28	1.33					2.7347	$\frac{5}{2}^+$	40	1.91

Table B.1: ^{53}Mn resonance parameters (*continued*)

	Current Work								Previous Work			
Resonance Number	E_p (MeV)	J^π	Γ_p (eV)	γ_p^2 (keV)	s′	ℓ'	$\Gamma_{p'}$ (eV)	$\gamma_{p'}^2$ (keV)	E_p (MeV)	J^π	Γ_p (eV)	γ_p^2 (keV)
65	2.7369	$\frac{1}{2}^-$	265	2.99					2.7353	$\frac{1}{2}^-$	200	2.29
66	2.7414	$\frac{1}{2}^+$	650	3.51					2.7396	$\frac{1}{2}^+$	500	2.69
67	2.7425	$\frac{5}{2}^+$	85	3.98					2.7409	$\frac{5}{2}^+$	120	5.66
68	2.7450	$\frac{3}{2}^-$	185	2.05					2.7434	$\frac{3}{2}^-$	125	1.39
69	2.7586	$\frac{1}{2}^-$	75	0.81					2.7569	$\frac{1}{2}^-$	75	0.81
70	2.7679	$\frac{3}{2}^-$	45	0.48					2.7659	$\frac{3}{2}^-$	30	0.32
71	2.7705	$\frac{5}{2}^+$	30	1.31	$\frac{5}{2}$	0	1	1.54	2.7686	$\frac{5}{2}^+$	40	1.76
72	2.7707	$\frac{1}{2}^+$	875	4.56					2.7689	$\frac{1}{2}^+$	700	3.56
73	2.7710	$\frac{3}{2}^-$	975	10.21					2.7691	$\frac{3}{2}^-$	800	8.40
74	2.7752	$\frac{3}{2}^-$	1400	14.53					2.7734	$\frac{3}{2}^-$	600	6.24
75	2.7886	$\frac{3}{2}^-$	425	4.29	$\frac{5}{2}$	1	3	10.79	2.7868	$\frac{3}{2}^-$	400	4.04
76	2.7996	$\frac{3}{2}^-$	30	0.30					2.7979	$\frac{3}{2}^-$	25	0.25
77	2.8054	$\frac{1}{2}^+$	80	0.38					2.8036	$\frac{1}{2}^+$	70	0.33

Table B.1: ^{53}Mn resonance parameters (*continued*)

	Current Work								Previous Work			
Resonance Number	E_p (MeV)	J^π	Γ_p (eV)	γ_p^2 (keV)	s′	ℓ'	$\Gamma_{p'}$ (eV)	$\gamma_{p'}^2$ (keV)	E_p (MeV)	J^π	Γ_p (eV)	γ_p^2 (keV)
78	2.8068	$\frac{5}{2}^+$	23	0.92					2.8050	$\frac{5}{2}^+$	5	0.20
79	2.8181	$\frac{1}{2}^+$	175	0.81					2.8165	$\frac{1}{2}^+$	175	0.81
80	2.8296	$\frac{3}{2}^-$	175	1.62					2.8279	$\frac{1}{2}^-$	250	2.32
81	2.8371	$\frac{5}{2}^+$	27	1.01					2.8352	$\frac{5}{2}^+$	10	0.37
82	2.8374	$\frac{1}{2}^-$	125	1.14					2.8356	$\frac{1}{2}^-$	90	0.82
83	2.8417	$\frac{3}{2}^+$	10	0.37					n/o			
84	2.8469	$\frac{3}{2}^+$	12	0.44					n/o			
85	2.8540	$\frac{5}{2}^+$	25	0.90					2.8520	$\frac{5}{2}^+$	5	0.18
86	2.8608	$\frac{1}{2}^+$	310	1.33					2.8589	$\frac{1}{2}^+$	200	0.86
87	2.8626	$\frac{5}{2}^+$	50	1.75					2.8607	$\frac{5}{2}^+$	20	0.71
88	2.8667	$\frac{3}{2}^+$	75	2.61					2.8648	$\frac{5}{2}^+$	20	0.70
89	2.8709	$\frac{5}{2}^+$	7	0.24					n/o			
90	2.8792	$\frac{3}{2}^-$	25	0.21					2.8771	$\frac{1}{2}^-$	20	0.17

Table B.1: ^{53}Mn resonance parameters (*continued*)

Current Work									Previous Work			
Resonance Number	E_p (MeV)	J^π	Γ_p (eV)	γ_p^2 (keV)	s′	ℓ'	$\Gamma_{p'}$ (eV)	$\gamma_{p'}^2$ (keV)	E_p (MeV)	J^π	Γ_p (eV)	γ_p^2 (keV)
91	2.8804	$\frac{1}{2}^-$	195	1.63					2.8784	$\frac{1}{2}^-$	125	1.05
92	2.8816	$\frac{1}{2}^+$	60	0.25					2.8795	$\frac{1}{2}^+$	40	0.17
93	2.8886	$\frac{3}{2}^-$	17	0.14					n/o			
94	2.8923	$\frac{5}{2}^+$	3	0.10					n/o			
95	2.8993	$\frac{3}{2}^-$	15	0.12					n/o			
96	2.9070	$\frac{5}{2}^+$	13	0.41					2.9047	$\frac{3}{2}^+$	5	0.16
97	2.9087	$\frac{1}{2}^-$	110	0.87					2.9064	$\frac{1}{2}^-$	60	0.47
98	2.9151	$\frac{1}{2}^-$	45	0.35					n/o			
99	2.9171	$\frac{5}{2}^+$	18	0.56					2.9146	$\frac{5}{2}^+$	10	0.31
100	2.9221	$\frac{5}{2}^+$	35	1.07					2.9199	$\frac{5}{2}^+$	15	0.46
101	2.9258	$\frac{5}{2}^+$	12	0.36					n/o			
102	2.9301	$\frac{3}{2}^-$	33	0.25					n/o			
103	2.9322	$\frac{1}{2}^-$	150	1.13					2.9301	$\frac{1}{2}^-$	110	0.83

Table B.1: ^{53}Mn resonance parameters (*continued*)

	Current Work								Previous Work			
Resonance Number	E_p (MeV)	J^π	Γ_p (eV)	γ_p^2 (keV)	s′	ℓ'	$\Gamma_{p'}$ (eV)	$\gamma_{p'}^2$ (keV)	E_p (MeV)	J^π	Γ_p (eV)	γ_p^2 (keV)
104	2.9405	$\frac{5}{2}^+$	37	1.09					2.9384	$\frac{5}{2}^+$	20	0.59
105	2.9421	$\frac{1}{2}^+$	700	2.60					2.9400	$\frac{1}{2}^+$	600	2.23
106	2.9427	$\frac{3}{2}^-$	75	0.55					2.9405	$\frac{1}{2}^-$	300	2.22
107	2.9488	$\frac{1}{2}^+$	1100	4.04					2.9466	$\frac{1}{2}^+$	1000	3.67
108	2.9543	$\frac{5}{2}^+$	3	0.09					n/o			
109	2.9579	$\frac{1}{2}^-$	150	1.08					2.9555	$\frac{1}{2}^-$	115	0.83
110	2.9591	$\frac{5}{2}^+$	65	1.83	$\frac{5}{2}$	0	2	0.86	2.9566	$\frac{5}{2}^+$	60	1.71
111	2.9616	$\frac{3}{2}^-$	35	0.25					2.9592	$\frac{3}{2}^-$	35	0.25
112	2.9639	$\frac{3}{2}^-$	10	0.07					2.9612	$\frac{1}{2}^-$	10	0.07
113	2.9675	$\frac{1}{2}^-$	85	0.60					2.9649	$\frac{3}{2}^-$	30	
114	2.9690	$\frac{1}{2}^+$	950	3.37					2.9665	$\frac{1}{2}^+$	800	2.84
115	2.9711	$\frac{1}{2}^-$	200	1.40					2.9684	$\frac{1}{2}^-$	175	1.23
116	2.9730	$\frac{3}{2}^+$	15	0.41					n/o			

Table B.1: ^{53}Mn resonance parameters (*continued*)

Current Work									Previous Work			
Resonance Number	E_p (MeV)	J^π	Γ_p (eV)	γ_p^2 (keV)	s′	ℓ'	$\Gamma_{p'}$ (eV)	$\gamma_{p'}^2$ (keV)	E_p (MeV)	J^π	Γ_p (eV)	γ_p^2 (keV)
117	2.9733	$\frac{1}{2}^+$	15	0.05					2.9706	$\frac{1}{2}^-$	10	0.07
118	2.9746	$\frac{5}{2}^+$	9	0.25					n/o			
119	2.9766	$\frac{3}{2}^+$	18	0.49					2.9738	$\frac{3}{2}^+$	5	0.14
120	2.9856	$\frac{1}{2}^-$	25	0.17					2.9825	$\frac{1}{2}^-$	15	0.10
121	2.9917	$\frac{3}{2}^-$	18	0.12					n/o			
122	2.9952	$\frac{3}{2}^+$	35	0.91					2.9921	$\frac{5}{2}$	10	0.26
123	3.0025	$\frac{5}{2}^+$	2	0.05					n/o			
124	3.0067	$\frac{1}{2}^-$	110	0.72					3.0038	$\frac{1}{2}^-$	110	0.72
125	3.0142	$\frac{1}{2}^-$	15	0.10					3.0113	$\frac{3}{2}^-$	25	0.16
126	3.0174	$\frac{1}{2}^+$	450	1.48					3.0147	$\frac{1}{2}^+$	450	1.48
127	3.0254	$\frac{5}{2}^+$	10	0.24					n/o			
128	3.0288	$\frac{5}{2}^-$	3	0.52					n/o			
129	3.0472	$\frac{5}{2}^+$	6	0.13					n/o			

Table B.1: ^{53}Mn resonance parameters (*continued*)

Current Work									Previous Work			
Resonance Number	E_p (MeV)	J^π	Γ_p (eV)	γ_p^2 (keV)	s′	ℓ'	$\Gamma_{p'}$ (eV)	$\gamma_{p'}^2$ (keV)	E_p (MeV)	J^π	Γ_p (eV)	γ_p^2 (keV)
130	3.0507	$\frac{1}{2}^-$	105	0.64					3.0478	$\frac{1}{2}^-$	90	0.55
131	3.0534	$\frac{3}{2}^-$	80	0.48					3.0504	$\frac{1}{2}^-$	100	0.60
132	3.0612	$\frac{3}{2}^-$	27	0.16					3.0582	$\frac{1}{2}^-$	50	0.30
133	3.0618	$\frac{5}{2}^+$	32	0.73					3.0589	$\frac{5}{2}^+$	25	0.57
134	3.0660	$\frac{1}{2}^-$	60	0.35					3.0630	$\frac{1}{2}^-$	75	0.44
135	3.0672	$\frac{5}{2}^+$	28	0.63	$\frac{3}{2}$	2	1	4.21	3.0643	$\frac{3}{2}^+$	20	0.45
					$\frac{5}{2}$	0	1	0.28				
136	3.0732	$\frac{3}{2}^+$	18	0.40					3.0702	$\frac{3}{2}^+$	5	0.11
137	3.0738	$\frac{5}{2}^+$	33	0.73					3.0709	$\frac{5}{2}^+$	20	0.45
138	3.0769	$\frac{5}{2}^+$	25	0.55					3.0741	$\frac{5}{2}^+$	10	0.22
139	3.0873	$\frac{5}{2}^+$	9	0.19					n/o			
140	3.0881	$\frac{5}{2}^+$	70	1.50					3.0855	$\frac{5}{2}^+$	75	1.62
141	3.0890	$\frac{3}{2}^+$	25	0.54					3.0862	$\frac{5}{2}^+$	5	0.11

Table B.1: ^{53}Mn resonance parameters (*continued*)

Current Work									Previous Work			
Resonance Number	E_p (MeV)	J^π	Γ_p (eV)	γ_p^2 (keV)	s′	ℓ'	$\Gamma_{p'}$ (eV)	$\gamma_{p'}^2$ (keV)	E_p (MeV)	J^π	Γ_p (eV)	γ_p^2 (keV)
142	3.0969	$\frac{3}{2}^+$	25	0.53	$\frac{3}{2}$	0	1	0.20	n/o			
					$\frac{3}{2}$	2	1	2.96				
					$\frac{5}{2}$	2	5	14.78				
143	3.0980	$\frac{3}{2}^-$	35	0.20	$\frac{3}{2}$	1	2	1.01	n/o			
					$\frac{5}{2}$	1	6	3.02				
144	3.1051	$\frac{1}{2}^+$	70	0.20					3.1024	$\frac{1}{2}^+$	40	0.11
145	3.1068	$\frac{3}{2}^-$	42	0.23	$\frac{3}{2}$	1	6	2.88	3.1042	$\frac{1}{2}^+$	15	0.04
					$\frac{5}{2}$	1	1	0.48				
146	3.1116	$\frac{1}{2}^+$	1250	3.53					3.109	$\frac{1}{2}^+$	1300	3.68
147	3.1135	$\frac{3}{2}^+$	115	2.34					3.1110	$\frac{3}{2}^+$	115	2.36
148	3.1138	$\frac{3}{2}^+$	8	0.16	$\frac{5}{2}$	0	3	0.55	n/o			
149	3.1197	$\frac{5}{2}^+$	10	0.20					n/o			
150	3.1222	$\frac{3}{2}^+$	2	0.04					n/o			

Table B.1: ^{53}Mn resonance parameters (*continued*)

	Current Work								Previous Work			
Resonance Number	E_p (MeV)	J^π	Γ_p (eV)	γ_p^2 (keV)	s′	ℓ'	$\Gamma_{p'}$ (eV)	$\gamma_{p'}^2$ (keV)	E_p (MeV)	J^π	Γ_p (eV)	γ_p^2 (keV)
151	3.1239	$\frac{1}{2}^-$	115	0.61					3.1210	$\frac{1}{2}^-$	100	0.53
152	3.1280	$\frac{1}{2}^+$	1200	3.31					3.1251	$\frac{1}{2}^+$	800	2.21
153	3.1297	$\frac{1}{2}^-$	350	1.85	$\frac{3}{2}$	1	75	31.95	3.1268	$\frac{1}{2}^-$	250	1.32
154	3.1315	$\frac{5}{2}^+$	95	1.87	$\frac{5}{2}$	0	5	0.84	3.1285	$\frac{5}{2}^+$	100	1.98
155	3.1333	$\frac{5}{2}^+$	20	0.39	$\frac{5}{2}$	0	2	0.33	3.1302	$\frac{5}{2}^+$	10	0.20
156	3.1350	$\frac{3}{2}^+$	15	0.29	$\frac{3}{2}$	0	2	0.33	3.1320	$\frac{3}{2}^+$	10	0.20
157	3.1365	$\frac{1}{2}^-$	1250	6.52	$\frac{3}{2}$	1	85	34.96	3.1339	$\frac{1}{2}^-$	1000	5.22
158	3.1398	$\frac{1}{2}^+$	1100	2.98					3.1372	$\frac{1}{2}^+$	1000	2.71
159	3.1427	$\frac{5}{2}^+$	30	0.58	$\frac{5}{2}$	0	10	1.58	3.1399	$\frac{5}{2}^+$	20	0.39
160	3.1467	$\frac{5}{2}^+$	15	0.29	$\frac{5}{2}$	0	3	0.46	n/o			
161	3.1475	$\frac{5}{2}^-$	25	3.29	$\frac{3}{2}$	1	13	5.05	3.1447	$\frac{5}{2}^+$	4	0.53
					$\frac{5}{2}$	1	3	1.17				
162	3.1538	$\frac{5}{2}^+$	12	0.23					3.1507	$\frac{3}{2}^+$	10	0.19

Table B.1: ^{53}Mn resonance parameters (*continued*)

Current Work									Previous Work			
Resonance Number	E_p (MeV)	J^π	Γ_p (eV)	γ_p^2 (keV)	s′	ℓ'	$\Gamma_{p'}$ (eV)	$\gamma_{p'}^2$ (keV)	E_p (MeV)	J^π	Γ_p (eV)	γ_p^2 (keV)
163	3.1550	$\frac{3}{2}^-$	75	0.38	$\frac{3}{2}$	1	4	1.50	3.1521	$\frac{3}{2}^-$	60	0.30
					$\frac{5}{2}$	1	8	2.99				
164	3.1552	$\frac{5}{2}^-$	10	1.29	$\frac{3}{2}$	1	3	1.12	n/o			
					$\frac{5}{2}$	1	1	0.37				
165	3.1605	$\frac{3}{2}^-$	45	0.23	$\frac{5}{2}$	1	8	2.91	3.1574	$\frac{1}{2}^-$	80	0.40
					$\frac{3}{2}$	1	55	20.01				
166	3.1626	$\frac{3}{2}^+$	50	0.92					3.1594	$\frac{5}{2}^+$	20	0.37
167	3.1660	$\frac{5}{2}^+$	55	1.01					3.1629	$\frac{5}{2}^+$	35	0.65
168	3.1672	$\frac{3}{2}^-$	20	0.10	$\frac{3}{2}$	1	55	19.34	n/o			
169	3.1678	$\frac{1}{2}^-$	155	0.77					3.1649	$\frac{1}{2}^-$	175	0.87
170	3.1741	$\frac{1}{2}^+$	3400	8.76					3.1713	$\frac{1}{2}^-$	4000	10.31
171	3.1839	$\frac{1}{2}^+$	300	0.76					3.1814	$\frac{1}{2}^+$	300	0.76
172	3.1847	$\frac{5}{2}^+$	4	0.07	$\frac{5}{2}$	0	5	0.64	n/o			

Table B.1: ^{53}Mn resonance parameters (*continued*)

	Current Work								Previous Work			
Resonance Number	E_p (MeV)	J^π	Γ_p (eV)	γ_p^2 (keV)	s′	ℓ'	$\Gamma_{p'}$ (eV)	$\gamma_{p'}^2$ (keV)	E_p (MeV)	J^π	Γ_p (eV)	γ_p^2 (keV)
173	3.1899	$\frac{3}{2}^+$	40	0.70					n/o			
174	3.1968	$\frac{5}{2}^+$	75	1.30					3.1939	$\frac{5}{2}^+$	75	1.31
175	3.2042	$\frac{1}{2}^+$	2200	5.43					3.2015	$\frac{1}{2}^+$	2200	5.43
176	3.2125	$\frac{3}{2}^+$	100	1.68					3.2094	$\frac{5}{2}^+$	40	0.68
177	3.2130	$\frac{3}{2}^-$	25	0.12	$\frac{3}{2}$	1	2	0.56	n/o			
					$\frac{5}{2}$	1	2	0.56				
178	3.2141	$\frac{1}{2}^+$	325	0.79					3.2112	$\frac{1}{2}^+$	300	0.73
179	3.2148	$\frac{3}{2}^-$	20	0.09					n/o			
180	3.2183	$\frac{5}{2}^+$	9	0.15	$\frac{3}{2}$	2	3	4.62	n/o			
					$\frac{5}{2}$	2	8	12.32				
181	3.2186	$\frac{3}{2}^-$	35	0.16					3.2156	$\frac{1}{2}^+$	20	0.05
182	3.2220	$\frac{5}{2}^+$	10	0.17					n/o			
183	3.2223	$\frac{3}{2}^-$	25	0.11	$\frac{3}{2}$	1	2	0.54	n/o			

Table B.1: ^{53}Mn resonance parameters (*continued*)

Current Work									Previous Work			
Resonance Number	E_p (MeV)	J^π	Γ_p (eV)	γ_p^2 (keV)	s′	ℓ'	$\Gamma_{p'}$ (eV)	$\gamma_{p'}^2$ (keV)	E_p (MeV)	J^π	Γ_p (eV)	γ_p^2 (keV)
183	3.2223	$\frac{3}{2}^-$			$\frac{5}{2}$	1	2	0.54				
184	3.2227	$\frac{1}{2}^+$	125	0.30					3.2197	$\frac{1}{2}^+$	160	0.38
185	3.2264	$\frac{3}{2}^+$	10	0.16					††			
186	3.2281	$\frac{5}{2}^+$	7	0.11	$\frac{5}{2}$	0	2	0.21				
187	3.2289	$\frac{5}{2}^+$	5	0.08								
188	3.2397	$\frac{5}{2}^+$	13	0.21	$\frac{3}{2}$	2	1	1.38				
					$\frac{5}{2}$	0	1	0.10				
189	3.2410	$\frac{5}{2}^+$	15	0.24								
190	3.2415	$\frac{1}{2}^-$	30	0.13								
191	3.2455	$\frac{5}{2}^+$	25	0.39								
192	3.2468	$\frac{1}{2}^+$	1000	2.33								
193	3.2516	$\frac{5}{2}^+$	8	0.13	$\frac{3}{2}$	2	1	1.304				
					$\frac{5}{2}$	0	1	0.10				

Table B.1: ^{53}Mn resonance parameters (*continued*)

Current Work									Previous Work			
Resonance Number	E_p (MeV)	J^π	Γ_p (eV)	γ_p^2 (keV)	s′	ℓ'	$\Gamma_{p'}$ (eV)	$\gamma_{p'}^2$ (keV)	E_p (MeV)	J^π	Γ_p (eV)	γ_p^2 (keV)
194	3.2569	$\frac{3}{2}^-$	27	0.12								
195	3.2623	$\frac{5}{2}^+$	50	0.76	$\frac{5}{2}$	0	4	0.36				
196	3.2684	$\frac{5}{2}^+$	95	1.44	$\frac{5}{2}$	0	11	0.97				
197	3.2698	$\frac{1}{2}^+$	40	0.09								
198	3.2710	$\frac{3}{2}^-$	40	0.17								
199	3.2788	$\frac{5}{2}^+$	58	0.86	$\frac{5}{2}$	0	2	0.17				
200	3.2834	$\frac{1}{2}^-$	30	0.12								
201	3.2843	$\frac{5}{2}^+$	30	0.44	$\frac{3}{2}$	2	1	1.11				
					$\frac{5}{2}$	0	3	0.25				
					$\frac{5}{2}$	2	1	0.11				
202	3.2877	$\frac{1}{2}^+$	65	0.14								
203	3.2898	$\frac{5}{2}^+$	20	0.29								
204	3.2907	$\frac{3}{2}^-$	30	0.12	$\frac{5}{2}$	1	6	1.18				

Table B.1: ^{53}Mn resonance parameters (*continued*)

Current Work									Previous Work			
Resonance Number	E_p (MeV)	J^π	Γ_p (eV)	γ_p^2 (keV)	s′	ℓ'	$\Gamma_{p'}$ (eV)	$\gamma_{p'}^2$ (keV)	E_p (MeV)	J^π	Γ_p (eV)	γ_p^2 (keV)
205	3.2945	$\frac{5}{2}^+$	10	0.14								
206	3.3079	$\frac{5}{2}^+$	18	0.25								
207	3.3122	$\frac{5}{2}^+$	50	0.70	$\frac{3}{2}$	2	2	1.95				
					$\frac{5}{2}$	0	1	0.07				
207	3.3122	$\frac{5}{2}^+$			$\frac{5}{2}$	2	3	2.93				
208	3.3148	$\frac{1}{2}^+$	1550	3.29								
209	3.3172	$\frac{5}{2}^+$	100	1.38	$\frac{3}{2}$	2	1	0.95				
					$\frac{5}{2}$	0	8	0.60				
210	3.3196	$\frac{5}{2}^+$	12	0.17								
211	3.3210	$\frac{1}{2}^+$	225	0.47								
212	3.3293	$\frac{5}{2}^+$	85	0.15	$\frac{5}{2}$	0	3	0.20				
					$\frac{3}{2}$	2	1	0.90				
213	3.3298	$\frac{1}{2}^-$	90	0.35								

Table B.1: ^{53}Mn resonance parameters (*continued*)

Current Work									Previous Work			
Resonance Number	E_p (MeV)	J^π	Γ_p (eV)	γ_p^2 (keV)	s′	ℓ'	$\Gamma_{p'}$ (eV)	$\gamma_{p'}^2$ (keV)	E_p (MeV)	J^π	Γ_p (eV)	γ_p^2 (keV)
214	3.3325	$\frac{5}{2}^+$	50	0.67	$\frac{5}{2}$	0	1	0.07				
					$\frac{5}{2}$	2	1	0.89				
					$\frac{3}{2}$	2	1	0.89				
215	3.3356	$\frac{5}{2}^+$	35	0.47	$\frac{5}{2}$	0	4	0.26				
216	3.3382	$\frac{5}{2}^+$	10	0.13								
217	3.3408	$\frac{1}{2}^-$	50	0.19	$\frac{3}{2}$	1	5	0.79				
					$\frac{5}{2}$	3	5	45.17				
218	3.3436	$\frac{1}{2}^+$	80	0.16								
219	3.3446	$\frac{5}{2}^+$	225	2.96	$\frac{5}{2}$	0	7	0.45				
					$\frac{3}{2}$	2	4	3.36				
220	3.3480	$\frac{1}{2}^+$	25	0.05	$\frac{3}{2}$	2	5	4.13				
					$\frac{5}{2}$	2	5	4.13				
221	3.3484	$\frac{3}{2}^-$	15	0.06	$\frac{3}{2}$	1	3	0.46				

Table B.1: ^{53}Mn resonance parameters (*continued*)

Current Work									Previous Work			
Resonance Number	E_p (MeV)	J^π	Γ_p (eV)	γ_p^2 (keV)	s′	ℓ'	$\Gamma_{p'}$ (eV)	$\gamma_{p'}^2$ (keV)	E_p (MeV)	J^π	Γ_p (eV)	γ_p^2 (keV)
					$\frac{5}{2}$	1	3	0.46				
222	3.3497	$\frac{1}{2}^-$	75	0.28								
223	3.3513	$\frac{5}{2}^+$	30	0.39	$\frac{3}{2}$	2	1	0.81				
					$\frac{5}{2}$	0	1	0.62				
					$\frac{5}{2}$	2	1	0.81				
224	3.3533	$\frac{1}{2}^-$	50	0.19								
225	3.3559	$\frac{1}{2}^+$	500	1.01								
226	3.3643	$\frac{1}{2}^+$	850	1.69								
227	3.3681	$\frac{1}{2}^-$	125	0.45								
228	3.3687	$\frac{5}{2}^-$	8	0.65								
229	3.3748	$\frac{5}{2}^+$	40	0.50	$\frac{5}{2}$	0	2	0.11				
					$\frac{3}{2}$	2	2	1.47				
230	3.3773	$\frac{3}{2}^-$	125	0.45	$\frac{5}{2}$	1	6	0.81				

Table B.1: ^{53}Mn resonance parameters (*continued*)

Current Work									Previous Work			
Resonance Number	E_p (MeV)	J^π	Γ_p (eV)	γ_p^2 (keV)	s′	ℓ'	$\Gamma_{p'}$ (eV)	$\gamma_{p'}^2$ (keV)	E_p (MeV)	J^π	Γ_p (eV)	γ_p^2 (keV)
					$\frac{5}{2}$	3	6	45.38				
231	3.3799	$\frac{1}{2}^-$	175	0.62								
232	3.3866	$\frac{1}{2}^+$	1500	2.90								
233	3.3899	$\frac{1}{2}^+$	500	0.96	$\frac{3}{2}$	2	17	11.65				
					$\frac{5}{2}$	2	17	11.65				
234	3.3907	$\frac{1}{2}^+$	3250	6.26								
235	3.3915	$\frac{5}{2}^+$	15	0.18	$\frac{3}{2}$	2	4	2.72				
					$\frac{5}{2}$	2	7	4.77				
236	3.3945	$\frac{5}{2}^+$	30	0.36								
237	3.3966	$\frac{3}{2}^-$	20	0.07								
238	3.3994	$\frac{5}{2}^+$	8	0.10								
239	3.4063	$\frac{5}{2}^+$	125	1.48	$\frac{3}{2}$	2	2	1.28				
					$\frac{5}{2}$	0	3	0.15				

Table B.1: ^{53}Mn resonance parameters (*continued*)

Current Work									Previous Work			
Resonance Number	E_p (MeV)	J^π	Γ_p (eV)	γ_p^2 (keV)	s′	ℓ'	$\Gamma_{p'}$ (eV)	$\gamma_{p'}^2$ (keV)	E_p (MeV)	J^π	Γ_p (eV)	γ_p^2 (keV)
239	3.4063	$\frac{5}{2}^+$			$\frac{5}{2}$	2	3	1.91				
240	3.4094	$\frac{1}{2}^-$	175	0.60								
241	3.4099	$\frac{5}{2}^+$	10	0.12	$\frac{5}{2}$	0	5	0.25				
					$\frac{5}{2}$	2	5	3.14				
242	3.4137	$\frac{1}{2}^+$	105	0.20								
243	3.4157	$\frac{5}{2}^+$	20	0.23	$\frac{5}{2}$	0	7	0.34				
					$\frac{3}{2}$	2	1	0.61				
244	3.4190	$\frac{1}{2}^-$	150	0.51	$\frac{5}{2}$	3	7	43.48				
					$\frac{3}{2}$	1	7	0.80				
245	3.4257	$\frac{1}{2}^+$	1700	3.13								
246	3.4286	$\frac{5}{2}^+$	10	0.11								
247	3.4297	$\frac{3}{2}^-$	20	0.07	$\frac{3}{2}$	3	4	23.65				
					$\frac{5}{2}$	1	2	0.22				

Table B.1: ^{53}Mn resonance parameters (*continued*)

Current Work									Previous Work			
Resonance Number	E_p (MeV)	J^π	Γ_p (eV)	γ_p^2 (keV)	s′	ℓ'	$\Gamma_{p'}$ (eV)	$\gamma_{p'}^2$ (keV)	E_p (MeV)	J^π	Γ_p (eV)	γ_p^2 (keV)
248	3.4310	$\frac{5}{2}^+$	10	0.11	$\frac{5}{2}$	0	2	0.09				
249	3.4341	$\frac{5}{2}^+$	75	0.85	$\frac{5}{2}$	0	10	0.45				
250	3.4373	$\frac{5}{2}^-$	3	0.21	$\frac{3}{2}$	1	2	0.21				
251	3.4400	$\frac{5}{2}^-$	6	0.42	$\frac{3}{2}$	1	2	0.21				
252	3.4435	$\frac{5}{2}^+$	7	0.08	$\frac{5}{2}$	0	1	0.04				
					$\frac{5}{2}$	2	3	1.63				
253	3.4438	$\frac{5}{2}^-$	10	0.70	$\frac{5}{2}$	1	2	0.21				
					$\frac{5}{2}$	3	2	11.08				
254	3.4448	$\frac{5}{2}^+$	65	0.72	$\frac{5}{2}$	0	12	0.52				
255	3.4456	$\frac{1}{2}^+$	450	0.81								
256	3.4468	$\frac{5}{2}^+$	4	0.04	$\frac{3}{2}$	2	5	2.68				
					$\frac{5}{2}$	0	2	0.09				
257	3.4507	$\frac{3}{2}^+$	70	0.77	$\frac{3}{2}$	0	2	0.08				

Table B.1: ^{53}Mn resonance parameters (*continued*)

Current Work									Previous Work			
Resonance Number	E_p (MeV)	J^π	Γ_p (eV)	γ_p^2 (keV)	s′	ℓ'	$\Gamma_{p'}$ (eV)	$\gamma_{p'}^2$ (keV)	E_p (MeV)	J^π	Γ_p (eV)	γ_p^2 (keV)
					$\frac{3}{2}$	2	2	1.06				
					$\frac{5}{2}$	2	8	4.23				
258	3.4515	$\frac{3}{2}^-$	85	0.27	$\frac{5}{2}$	1	8	0.80				
259	3.4539	$\frac{1}{2}^-$	130	0.42								
260	3.4594	$\frac{3}{2}^-$	30	0.10								
261	3.4638	$\frac{3}{2}^-$	12	0.04	$\frac{3}{2}$	3	2	10.12				
					$\frac{5}{2}$	1	3	0.29				
262	3.4656	$\frac{1}{2}^+$	400	0.70								
263	3.4682	$\frac{3}{2}^+$	30	0.32								

† Previous assignment is probably a typographical error

†† End of Moses data

Table B.2: $J^\pi = \frac{1}{2}^+$ level sequence.

Resonance Number	E_p (MeV)	J^π	Γ_p (eV)	γ_p^2 (keV)	s′	ℓ′	$\Gamma_{p'}$ (eV)	$\gamma_{p'}^2$ (keV)
2	2.1358	$\frac{1}{2}^+$	140	3.58				
3	2.1491	$\frac{1}{2}^+$	50	1.22				
4	2.1558	$\frac{1}{2}^+$	400	9.58				
5	2.2160	$\frac{1}{2}^+$	125	2.48				
10	2.3487	$\frac{1}{2}^+$	45	0.61				
16	2.3754	$\frac{1}{2}^+$	90	1.13				
20	2.4113	$\frac{1}{2}^+$	30	0.34				
21	2.4213	$\frac{1}{2}^+$	20	0.22				
32	2.5243	$\frac{1}{2}^+$	25	0.22				
33	2.5455	$\frac{1}{2}^+$	95	0.78				
34	2.5582	$\frac{1}{2}^+$	75	0.60				
38	2.5901	$\frac{1}{2}^+$	60	0.45				
39	2.5964	$\frac{1}{2}^+$	320	2.35				
43	2.6237	$\frac{1}{2}^+$	75	0.52				
47	2.6439	$\frac{1}{2}^+$	375	2.48				
49	2.6643	$\frac{1}{2}^+$	325	2.06				
52	2.6791	$\frac{1}{2}^+$	110	0.67				
60	2.7096	$\frac{1}{2}^+$	95	0.55				
66	2.7414	$\frac{1}{2}^+$	650	3.51				
72	2.7707	$\frac{1}{2}^+$	875	4.56				
77	2.8054	$\frac{1}{2}^+$	80	0.38				

Table B.2: $J^\pi = \frac{1}{2}^+$ level sequence (*continued*)

Resonance Number	E_p (MeV)	J^π	Γ_p (eV)	γ_p^2 (keV)	s′	ℓ'	$\Gamma_{p'}$ (eV)	$\gamma_{p'}^2$ (keV)
79	2.8181	$\frac{1}{2}^+$	175	0.81				
86	2.8608	$\frac{1}{2}^+$	310	1.33				
92	2.8816	$\frac{1}{2}^+$	60	0.25				
105	2.9421	$\frac{1}{2}^+$	700	2.60				
107	2.9488	$\frac{1}{2}^+$	1100	4.04				
114	2.9690	$\frac{1}{2}^+$	950	3.37				
117	2.9733	$\frac{1}{2}^+$	15	0.05				
126	3.0174	$\frac{1}{2}^+$	450	1.48				
144	3.1051	$\frac{1}{2}^+$	70	0.20				
146	3.1116	$\frac{1}{2}^+$	1250	3.53				
152	3.1280	$\frac{1}{2}^+$	1200	3.31				
158	3.1398	$\frac{1}{2}^+$	1100	2.98				
170	3.1741	$\frac{1}{2}^+$	3400	8.76				
171	3.1839	$\frac{1}{2}^+$	300	0.76				
175	3.2042	$\frac{1}{2}^+$	2200	5.43				
178	3.2141	$\frac{1}{2}^+$	325	0.79				
184	3.2227	$\frac{1}{2}^+$	125	0.30				
192	3.2468	$\frac{1}{2}^+$	1000	2.33				
197	3.2698	$\frac{1}{2}^+$	40	0.09				
202	3.2877	$\frac{1}{2}^+$	65	0.14				
208	3.3148	$\frac{1}{2}^+$	1550	3.29				

Table B.2: $J^\pi = \frac{1}{2}^+$ level sequence (*continued*)

Resonance Number	E_p (MeV)	J^π	Γ_p (eV)	γ_p^2 (keV)	s′	ℓ'	$\Gamma_{p'}$ (eV)	$\gamma_{p'}^2$ (keV)
211	3.3210	$\frac{1}{2}^+$	225	0.47				
218	3.3436	$\frac{1}{2}^+$	80	0.16				
220	3.3480	$\frac{1}{2}^+$	25	0.05	$\frac{3}{2}$	2	5	4.13
					$\frac{5}{2}$	2	5	4.13
225	3.3559	$\frac{1}{2}^+$	500	1.01				
226	3.3643	$\frac{1}{2}^+$	850	1.69				
232	3.3866	$\frac{1}{2}^+$	1500	2.90				
233	3.3899	$\frac{1}{2}^+$	500	0.96	$\frac{3}{2}$	2	17	11.65
					$\frac{5}{2}$	2	17	11.65
234	3.3907	$\frac{1}{2}^+$	3250	6.26				
242	3.4137	$\frac{1}{2}^+$	105	0.20				
245	3.4257	$\frac{1}{2}^+$	1700	3.13				
255	3.4456	$\frac{1}{2}^+$	450	0.81				
262	3.4656	$\frac{1}{2}^+$	400	0.70				

Table B.3: $J^\pi = \frac{1}{2}^-$ level sequence.

Resonance Number	E_p (MeV)	J^π	Γ_p (eV)	γ_p^2 (keV)	s′	ℓ'	$\Gamma_{p'}$ (eV)	$\gamma_{p'}^2$ (keV)
1	2.1197	$\frac{1}{2}^-$	30	1.89				
6	2.2751	$\frac{1}{2}^-$	140	5.29				
7	2.3144	$\frac{1}{2}^-$	15	0.50				
8	2.3243	$\frac{1}{2}^-$	45	1.46				
14	2.3683	$\frac{1}{2}^-$	65	1.86				
17	2.3848	$\frac{1}{2}^-$	26	0.71				
18	2.3888	$\frac{1}{2}^-$	60	1.62				
19	2.3992	$\frac{1}{2}^-$	40	1.05				
24	2.4418	$\frac{1}{2}^-$	40	0.93				
25	2.4470	$\frac{1}{2}^-$	110	2.52				
28	2.5005	$\frac{1}{2}^-$	150	2.99				
29	2.5125	$\frac{1}{2}^-$	25	0.48				
31	2.5196	$\frac{1}{2}^-$	55	1.04				
40	2.5980	$\frac{1}{2}^-$	80	1.25				
46	2.6381	$\frac{1}{2}^-$	75	1.06				
55	2.6902	$\frac{1}{2}^-$	30	0.38				
65	2.7369	$\frac{1}{2}^-$	265	2.99				
69	2.7586	$\frac{1}{2}^-$	75	0.81				
82	2.8374	$\frac{1}{2}^-$	125	1.14				
91	2.8804	$\frac{1}{2}^-$	195	1.63				
97	2.9087	$\frac{1}{2}^-$	110	0.87				

Table B.3: $J^\pi = \frac{1}{2}^-$ level sequence (*continued*)

Resonance Number	E_p (MeV)	J^π	Γ_p (eV)	γ_p^2 (keV)	s′	ℓ'	$\Gamma_{p'}$ (eV)	$\gamma_{p'}^2$ (keV)
98	2.9151	$\frac{1}{2}^-$	45	0.35				
103	2.9322	$\frac{1}{2}^-$	150	1.13				
109	2.9579	$\frac{1}{2}^-$	150	1.08				
113	2.9675	$\frac{1}{2}^-$	85	0.60				
115	2.9711	$\frac{1}{2}^-$	200	1.40				
120	2.9856	$\frac{1}{2}^-$	25	0.17				
124	3.0067	$\frac{1}{2}^-$	110	0.72				
125	3.0142	$\frac{1}{2}^-$	15	0.10				
130	3.0507	$\frac{1}{2}^-$	105	0.64				
134	3.0660	$\frac{1}{2}^-$	60	0.35				
151	3.1239	$\frac{1}{2}^-$	115	0.61				
153	3.1297	$\frac{1}{2}^-$	350	1.85	$\frac{3}{2}$	1	75	31.95
157	3.1365	$\frac{1}{2}^-$	1250	6.52	$\frac{3}{2}$	1	85	34.96
169	3.1678	$\frac{1}{2}^-$	155	0.77				
190	3.2415	$\frac{1}{2}^-$	30	0.13				
200	3.2834	$\frac{1}{2}^-$	30	0.12				
213	3.3298	$\frac{1}{2}^-$	90	0.35				
217	3.3408	$\frac{1}{2}^-$	50	0.19	$\frac{3}{2}$	1	5	0.79
					$\frac{5}{2}$	3	5	45.17
222	3.3497	$\frac{1}{2}^-$	75	0.28				
224	3.3533	$\frac{1}{2}^-$	50	0.19				

Table B.3: $J^\pi = \frac{1}{2}^-$ level sequence (*continued*)

Resonance Number	E_p (MeV)	J^π	Γ_p (eV)	γ_p^2 (keV)	s′	ℓ'	$\Gamma_{p'}$ (eV)	$\gamma_{p'}^2$ (keV)
227	3.3681	$\frac{1}{2}^-$	125	0.45				
231	3.3799	$\frac{1}{2}^-$	175	0.62				
240	3.4094	$\frac{1}{2}^-$	175	0.60				
244	3.4190	$\frac{1}{2}^-$	150	0.51	$\frac{5}{2}$	3	7	43.48
					$\frac{3}{2}$	1	7	0.80
259	3.4539	$\frac{1}{2}^-$	130	0.42				

Table B.4: $J^\pi = \frac{3}{2}^-$ level sequence.

Resonance Number	E_p (MeV)	J^π	Γ_p (eV)	γ_p^2 (keV)	s′	ℓ'	$\Gamma_{p'}$ (eV)	$\gamma_{p'}^2$ (keV)
12	2.3524	$\frac{3}{2}^-$	15	0.45				
23	2.4254	$\frac{3}{2}^-$	32	0.78				
26	2.4532	$\frac{3}{2}^-$	30	0.68				
35	2.5839	$\frac{3}{2}^-$	40	0.65				
37	2.5857	$\frac{3}{2}^-$	60	0.96				
42	2.6162	$\frac{3}{2}^-$	100	1.49				
45	2.6273	$\frac{3}{2}^-$	33	0.48				
51	2.6711	$\frac{3}{2}^-$	25	0.33				
54	2.6843	$\frac{3}{2}^-$	15	0.19				
56	2.6921	$\frac{3}{2}^-$	70	0.87				
57	2.7019	$\frac{3}{2}^-$	90	1.10				
58	2.7069	$\frac{3}{2}^-$	100	1.21				
61	2.7174	$\frac{3}{2}^-$	70	0.83				
68	2.7450	$\frac{3}{2}^-$	185	2.05				
70	2.7679	$\frac{3}{2}^-$	45	0.48				
73	2.7710	$\frac{3}{2}^-$	975	10.21				
74	2.7752	$\frac{3}{2}^-$	1400	14.53				
75	2.7886	$\frac{3}{2}^-$	425	4.29	$\frac{5}{2}$	1	3	10.79
76	2.7996	$\frac{3}{2}^-$	30	0.30				
80	2.8296	$\frac{3}{2}^-$	175	1.62				
90	2.8792	$\frac{3}{2}^-$	25	0.21				

Table B.4: $J^\pi = \frac{3}{2}^-$ level sequence (*continued*)

Resonance Number	E_p (MeV)	J^π	Γ_p (eV)	γ_p^2 (keV)	s′	ℓ'	$\Gamma_{p'}$ (eV)	$\gamma_{p'}^2$ (keV)
93	2.8886	$\frac{3}{2}^-$	17	0.14				
95	2.8993	$\frac{3}{2}^-$	15	0.12				
102	2.9301	$\frac{3}{2}^-$	33	0.25				
106	2.9427	$\frac{3}{2}^-$	75	0.55				
111	2.9616	$\frac{3}{2}^-$	35	0.25				
112	2.9639	$\frac{3}{2}^-$	10	0.07				
121	2.9917	$\frac{3}{2}^-$	18	0.12				
131	3.0534	$\frac{3}{2}^-$	80	0.48				
132	3.0612	$\frac{3}{2}^-$	27	0.16				
143	3.0980	$\frac{3}{2}^-$	35	0.20	$\frac{3}{2}$	1	2	1.01
					$\frac{5}{2}$	1	6	3.02
145	3.1068	$\frac{3}{2}^-$	42	0.23	$\frac{3}{2}$	1	6	2.88
					$\frac{5}{2}$	1	1	0.48
163	3.1550	$\frac{3}{2}^-$	75	0.38	$\frac{3}{2}$	1	4	1.50
					$\frac{5}{2}$	1	8	2.99
165	3.1605	$\frac{3}{2}^-$	45	0.23	$\frac{3}{2}$	1	55	20.01
					$\frac{5}{2}$	1	8	2.91
168	3.1672	$\frac{3}{2}^-$	20	0.10	$\frac{3}{2}$	1	55	19.34
177	3.2130	$\frac{3}{2}^-$	25	0.12	$\frac{3}{2}$	1	2	0.56
					$\frac{5}{2}$	1	2	0.56
179	3.2148	$\frac{3}{2}^-$	20	0.09				

Table B.4: $J^\pi = \frac{3}{2}^-$ level sequence (*continued*)

Resonance Number	E_p (MeV)	J^π	Γ_p (eV)	γ_p^2 (keV)	s′	ℓ'	$\Gamma_{p'}$ (eV)	$\gamma_{p'}^2$ (keV)
181	3.2186	$\frac{3}{2}^-$	35	0.16				
183	3.2223	$\frac{3}{2}^-$	25	0.11	$\frac{3}{2}$	1	2	0.54
					$\frac{5}{2}$	1	2	0.54
194	3.2569	$\frac{3}{2}^-$	27	0.12				
198	3.2710	$\frac{3}{2}^-$	40	0.17				
204	3.2907	$\frac{3}{2}^-$	30	0.12	$\frac{5}{2}$	1	6	1.18
221	3.3484	$\frac{3}{2}^-$	15	0.06	$\frac{3}{2}$	1	3	0.46
					$\frac{5}{2}$	1	3	0.46
230	3.3773	$\frac{3}{2}^-$	125	0.45	$\frac{5}{2}$	1	6	0.81
					$\frac{5}{2}$	3	6	45.38
237	3.3966	$\frac{3}{2}^-$	20	0.07				
247	3.4297	$\frac{3}{2}^-$	20	0.07	$\frac{3}{2}$	3	4	23.65
					$\frac{5}{2}$	1	2	0.22
258	3.4515	$\frac{3}{2}^-$	85	0.27	$\frac{5}{2}$	1	8	0.80
260	3.4594	$\frac{3}{2}^-$	30	0.10				
261	3.4638	$\frac{3}{2}^-$	12	0.04	$\frac{3}{2}$	3	2	10.12
					$\frac{5}{2}$	1	3	0.29

Table B.5: $\ell = 2$ level sequence.

Resonance Number	E_p (MeV)	J^π	Γ_p (eV)	γ_p^2 (keV)	s′	ℓ'	$\Gamma_{p'}$ (eV)	$\gamma_{p'}^2$ (keV)
9	2.3311	$\frac{5}{2}^+$	14	2.12				
11	2.3496	$\frac{3}{2}^+$	15	2.14				
13	2.3657	$\frac{5}{2}^+$	15	2.03				
15	2.3736	$\frac{5}{2}^+$	43	5.68				
22	2.4242	$\frac{5}{2}^+$	20	2.26				
27	2.4720	$\frac{5}{2}^+$	40	3.91				
30	2.5158	$\frac{5}{2}^+$	30	2.58				
36	2.5850	$\frac{3}{2}^+$	32	2.27				
41	2.5998	$\frac{5}{2}^+$	55	3.74				
44	2.6257	$\frac{5}{2}^+$	17	1.08				
48	2.6567	$\frac{5}{2}^+$	16	0.93				
50	2.6661	$\frac{5}{2}^+$	25	1.42				
53	2.6810	$\frac{5}{2}^+$	25	1.37				
59	2.7085	$\frac{5}{2}^+$	5	0.26				
62	2.7212	$\frac{5}{2}^+$	15	0.74				
63	2.7245	$\frac{5}{2}^+$	35	1.72				
64	2.7363	$\frac{5}{2}^+$	28	1.33				
67	2.7425	$\frac{5}{2}^+$	85	3.98				
71	2.7705	$\frac{5}{2}^+$	30	1.31	$\frac{5}{2}$	0	1	1.54
78	2.8068	$\frac{5}{2}^+$	23	0.92				
81	2.8371	$\frac{5}{2}^+$	27	1.01				

Table B.5: $\ell = 2$ level sequence (*continued*)

Resonance Number	E_p (MeV)	J^π	Γ_p (eV)	γ_p^2 (keV)	s′	ℓ'	$\Gamma_{p'}$ (eV)	$\gamma_{p'}^2$ (keV)
83	2.8417	$\frac{3}{2}^+$	10	0.37				
84	2.8469	$\frac{3}{2}^+$	12	0.44				
85	2.8540	$\frac{5}{2}^+$	25	0.90				
87	2.8626	$\frac{5}{2}^+$	50	1.75				
88	2.8667	$\frac{3}{2}^+$	75	2.61				
89	2.8709	$\frac{5}{2}^+$	7	0.24				
94	2.8923	$\frac{5}{2}^+$	3	0.10				
96	2.9070	$\frac{5}{2}^+$	13	0.41				
99	2.9171	$\frac{5}{2}^+$	18	0.56				
100	2.9221	$\frac{5}{2}^+$	35	1.07				
101	2.9258	$\frac{5}{2}^+$	12	0.36				
104	2.9405	$\frac{5}{2}^+$	37	1.09				
108	2.9543	$\frac{5}{2}^+$	3	0.09				
110	2.9591	$\frac{5}{2}^+$	65	1.83	$\frac{5}{2}$	0	2	0.86
116	2.9730	$\frac{3}{2}^+$	15	0.41				
118	2.9746	$\frac{5}{2}^+$	9	0.25				
119	2.9766	$\frac{3}{2}^+$	18	0.49				
122	2.9952	$\frac{3}{2}^+$	35	0.91				
123	3.0025	$\frac{5}{2}^+$	2	0.05				
127	3.0254	$\frac{5}{2}^+$	10	0.24				
129	3.0472	$\frac{5}{2}^+$	6	0.13				

Table B.5: $\ell = 2$ level sequence (*continued*)

Resonance Number	E_p (MeV)	J^π	Γ_p (eV)	γ_p^2 (keV)	s′	ℓ'	$\Gamma_{p'}$ (eV)	$\gamma_{p'}^2$ (keV)
133	3.0618	$\frac{5}{2}^+$	32	0.73				
135	3.0672	$\frac{5}{2}^+$	28	0.63	$\frac{3}{2}$	2	1	4.21
					$\frac{5}{2}$	0	1	0.28
136	3.0732	$\frac{3}{2}^+$	18	0.40				
137	3.0738	$\frac{5}{2}^+$	33	0.73				
138	3.0769	$\frac{5}{2}^+$	25	0.55				
139	3.0873	$\frac{5}{2}^+$	9	0.19				
140	3.0881	$\frac{5}{2}^+$	70	1.50				
141	3.0890	$\frac{3}{2}^+$	25	0.54				
142	3.0969	$\frac{3}{2}^+$	25	0.53	$\frac{3}{2}$	0	1	0.20
					$\frac{3}{2}$	2	1	2.96
					$\frac{5}{2}$	2	5	14.78
147	3.1135	$\frac{3}{2}^+$	115	2.34				
148	3.1138	$\frac{3}{2}^+$	8	0.16	$\frac{5}{2}$	0	3	0.55
149	3.1197	$\frac{5}{2}^+$	10	0.20				
150	3.1222	$\frac{3}{2}^+$	2	0.04				
154	3.1315	$\frac{5}{2}^+$	95	1.87	$\frac{5}{2}$	0	5	0.84
155	3.1333	$\frac{5}{2}^+$	20	0.39	$\frac{5}{2}$	0	2	0.33
156	3.1350	$\frac{3}{2}^+$	15	0.29	$\frac{3}{2}$	0	2	0.33
159	3.1427	$\frac{5}{2}^+$	30	0.58	$\frac{5}{2}$	0	10	1.58
160	3.1467	$\frac{5}{2}^+$	15	0.29	$\frac{5}{2}$	0	3	0.46

Table B.5: $\ell = 2$ level sequence (*continued*)

Resonance Number	E_p (MeV)	J^π	Γ_p (eV)	γ_p^2 (keV)	s′	ℓ'	$\Gamma_{p'}$ (eV)	$\gamma_{p'}^2$ (keV)
162	3.1538	$\frac{5}{2}^+$	12	0.23				
166	3.1626	$\frac{3}{2}^+$	50	0.92				
167	3.1660	$\frac{5}{2}^+$	55	1.01				
172	3.1847	$\frac{5}{2}^+$	4	0.07	$\frac{5}{2}$	0	5	0.64
173	3.1899	$\frac{3}{2}^+$	40	0.70				
174	3.1968	$\frac{5}{2}^+$	75	1.30				
176	3.2125	$\frac{3}{2}^+$	100	1.68				
180	3.2183	$\frac{5}{2}^+$	9	0.15	$\frac{3}{2}$	2	3	4.62
					$\frac{5}{2}$	2	8	12.32
182	3.2220	$\frac{5}{2}^+$	10	0.17				
185	3.2264	$\frac{3}{2}^+$	10	0.16				
186	3.2281	$\frac{5}{2}^+$	7	0.11	$\frac{5}{2}$	0	2	0.21
187	3.2289	$\frac{5}{2}^+$	5	0.08				
188	3.2397	$\frac{5}{2}^+$	13	0.21	$\frac{3}{2}$	2	1	1.38
					$\frac{5}{2}$	0	1	0.10
189	3.2410	$\frac{5}{2}^+$	15	0.24				
191	3.2455	$\frac{5}{2}^+$	25	0.39				
193	3.2516	$\frac{5}{2}^+$	8	0.13	$\frac{3}{2}$	2	1	1.30
					$\frac{5}{2}$	0	1	0.10
195	3.2623	$\frac{5}{2}^+$	50	0.76	$\frac{5}{2}$	0	4	0.36
196	3.2684	$\frac{5}{2}^+$	95	1.44	$\frac{5}{2}$	0	11	0.97

Table B.5: $\ell = 2$ level sequence (*continued*)

Resonance Number	E_p (MeV)	J^π	Γ_p (eV)	γ_p^2 (keV)	s′	ℓ'	$\Gamma_{p'}$ (eV)	$\gamma_{p'}^2$ (keV)
199	3.2788	$\frac{5}{2}^+$	58	0.86	$\frac{5}{2}$	0	2	0.17
201	3.2843	$\frac{5}{2}^+$	30	0.44	$\frac{3}{2}$	2	1	1.11
					$\frac{5}{2}$	0	3	0.25
					$\frac{5}{2}$	2	1	0.11
203	3.2898	$\frac{5}{2}^+$	20	0.29				
205	3.2945	$\frac{5}{2}^+$	10	0.14				
206	3.3079	$\frac{5}{2}^+$	18	0.25				
207	3.3122	$\frac{5}{2}^+$	50	0.70	$\frac{3}{2}$	2	2	1.95
					$\frac{5}{2}$	0	1	0.07
					$\frac{5}{2}$	2	3	2.93
209	3.3172	$\frac{5}{2}^+$	100	1.38	$\frac{3}{2}$	2	1	0.95
					$\frac{5}{2}$	0	8	0.60
210	3.3196	$\frac{5}{2}^+$	12	0.17				
212	3.3293	$\frac{5}{2}^+$	85	0.15	$\frac{3}{2}$	2	1	0.90
					$\frac{5}{2}$	0	3	0.20
214	3.3325	$\frac{5}{2}^+$	50	0.67	$\frac{3}{2}$	2	1	0.89
					$\frac{5}{2}$	2	1	0.89
					$\frac{5}{2}$	0	1	0.07
215	3.3356	$\frac{5}{2}^+$	35	0.47	$\frac{5}{2}$	0	4	0.26
216	3.3382	$\frac{5}{2}^+$	10	0.13				
219	3.3446	$\frac{5}{2}^+$	225	2.96	$\frac{3}{2}$	2	4	3.36

Table B.5: $\ell = 2$ level sequence (*continued*)

Resonance Number	E_p (MeV)	J^π	Γ_p (eV)	γ_p^2 (keV)	s′	ℓ'	$\Gamma_{p'}$ (eV)	$\gamma_{p'}^2$ (keV)
					$\frac{5}{2}$	0	7	0.45
223	3.3513	$\frac{5}{2}^+$	30	0.39	$\frac{3}{2}$	2	1	0.81
					$\frac{5}{2}$	0	1	0.62
					$\frac{5}{2}$	2	1	0.81
229	3.3748	$\frac{5}{2}^+$	40	0.50	$\frac{3}{2}$	2	2	1.47
					$\frac{5}{2}$	0	2	0.11
235	3.3915	$\frac{5}{2}^+$	15	0.18	$\frac{3}{2}$	2	4	2.72
					$\frac{5}{2}$	2	7	4.77
236	3.3945	$\frac{5}{2}^+$	30	0.36				
238	3.3994	$\frac{5}{2}^+$	8	0.10				
239	3.4063	$\frac{5}{2}^+$	125	1.48	$\frac{3}{2}$	2	2	1.28
					$\frac{5}{2}$	0	3	0.15
					$\frac{5}{2}$	2	3	1.91
241	3.4099	$\frac{5}{2}^+$	10	0.12	$\frac{5}{2}$	0	5	0.25
					$\frac{5}{2}$	2	5	3.14
243	3.4157	$\frac{5}{2}^+$	20	0.23	$\frac{3}{2}$	2	1	0.61
					$\frac{5}{2}$	0	7	0.34
246	3.4286	$\frac{5}{2}^+$	10	0.11				
248	3.4310	$\frac{5}{2}^+$	10	0.11	$\frac{5}{2}$	0	2	0.09
249	3.4341	$\frac{5}{2}^+$	75	0.85	$\frac{5}{2}$	0	10	0.45
252	3.4435	$\frac{5}{2}^+$	7	0.08	$\frac{5}{2}$	0	1	0.04

Table B.5: $\ell = 2$ level sequence (*continued*)

Resonance Number	E_p (MeV)	J^π	Γ_p (eV)	γ_p^2 (keV)	s′	ℓ'	$\Gamma_{p'}$ (eV)	$\gamma_{p'}^2$ (keV)
					$\frac{5}{2}$	2	3	1.63
254	3.4448	$\frac{5}{2}^+$	65	0.72	$\frac{5}{2}$	0	12	0.52
256	3.4468	$\frac{5}{2}^+$	4	0.04	$\frac{3}{2}$	2	5	2.68
					$\frac{5}{2}$	0	2	0.09
257	3.4507	$\frac{3}{2}^+$	70	0.77	$\frac{3}{2}$	0	2	0.08
					$\frac{3}{2}$	2	2	1.06
					$\frac{5}{2}$	2	8	4.23
263	3.4682	$\frac{3}{2}^+$	30	0.32				

Table B.6: $\ell = 3$ level sequence

Resonance Number	E_p (MeV)	J^π	Γ_p (eV)	γ_p^2 (keV)	s′	ℓ'	$\Gamma_{p'}$ (eV)	$\gamma_{p'}^2$ (keV)
128	3.0288	$\frac{5}{2}^-$	3	0.52				
161	3.1475	$\frac{5}{2}^-$	25	3.29	$\frac{3}{2}$	1	13	5.05
					$\frac{5}{2}$	1	3	1.17
164	3.1552	$\frac{5}{2}^-$	10	1.29	$\frac{3}{2}$	1	3	1.12
					$\frac{5}{2}$	1	1	0.37
228	3.3687	$\frac{5}{2}^-$	8	0.65				
250	3.4373	$\frac{5}{2}^-$	3	0.21	$\frac{3}{2}$	1	2	0.21
251	3.4400	$\frac{5}{2}^-$	6	0.42	$\frac{3}{2}$	1	2	0.21
253	3.4438	$\frac{5}{2}^-$	10	0.7	$\frac{5}{2}$	1	2	0.21
					$\frac{5}{2}$	3	2	11.08

Appendix C

Energy Unfolding of Level Sequences

Prior to performing the spacing analysis presented in chapter 4, the exponential dependence of the level density on excitation energy must be removed from each sequence individually. The integrated level density, N(E), is linearized using the procedure described by Shriner *et al.* [Shr90]. The energy endpoints used in the calculation of the linear level densities are E_{min} = 8623.8 keV and E_{max} = 9964.9 keV. The endpoints represent the entire energy range covered in the experiment. The results of the linearizations for each of the sequences analyzed are presented in this appendix.

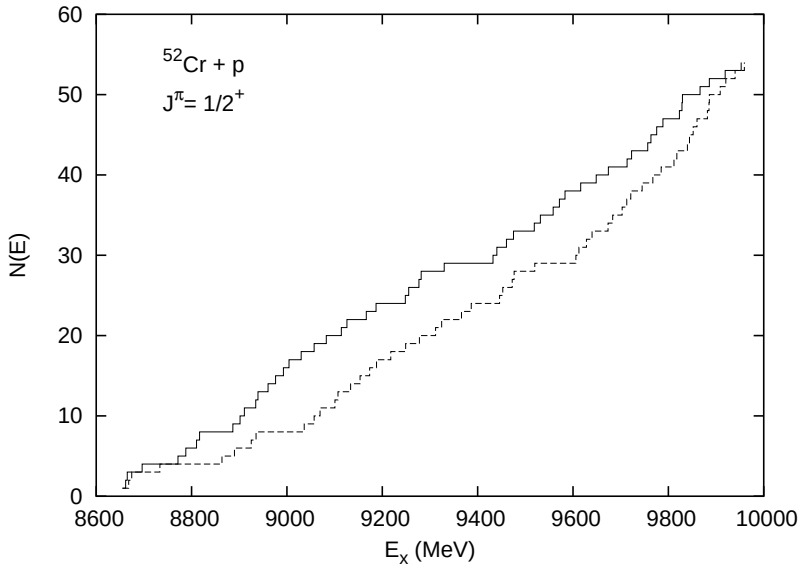

Figure C.1: Integrated level density N(E) for the $J^{\pi} = \frac{1}{2}^{+}$ level sequence. The experimental energies are shown by the dashed line while the solid line represents linearized values.

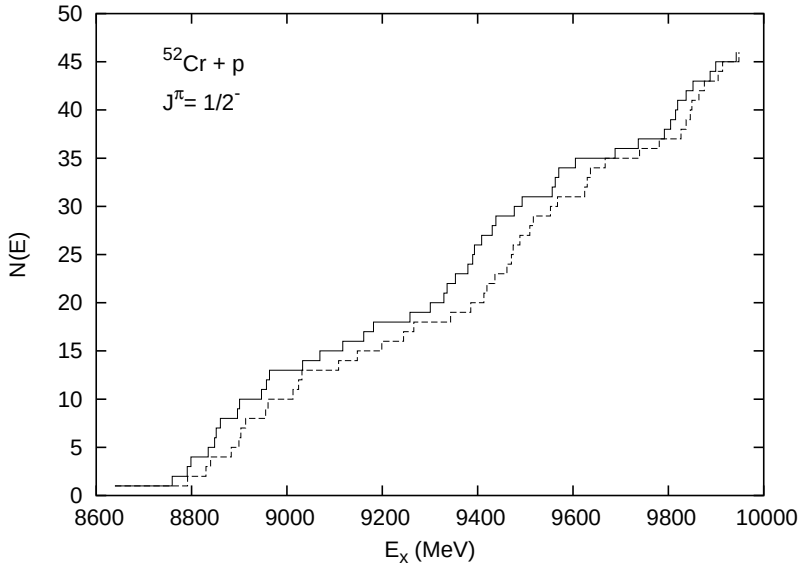

Figure C.2: Integrated level density N(E) for the $J^{\pi} = \frac{1}{2}^{-}$ level sequence. The experimental energies are shown by the dashed line while the solid line represents linearized values.

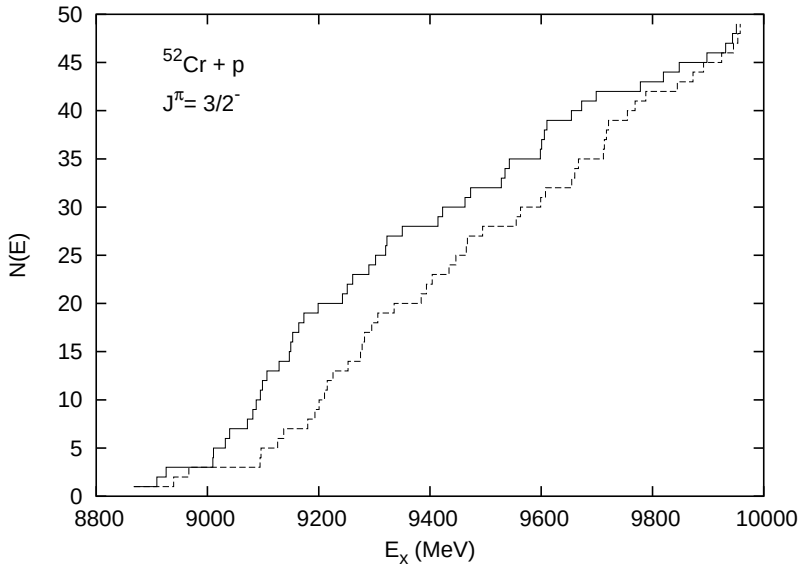

Figure C.3: Integrated level density N(E) for the $J^{\pi} = \frac{3}{2}^{-}$ level sequence. The experimental energies are shown by the dashed line while the solid line represents linearized values.

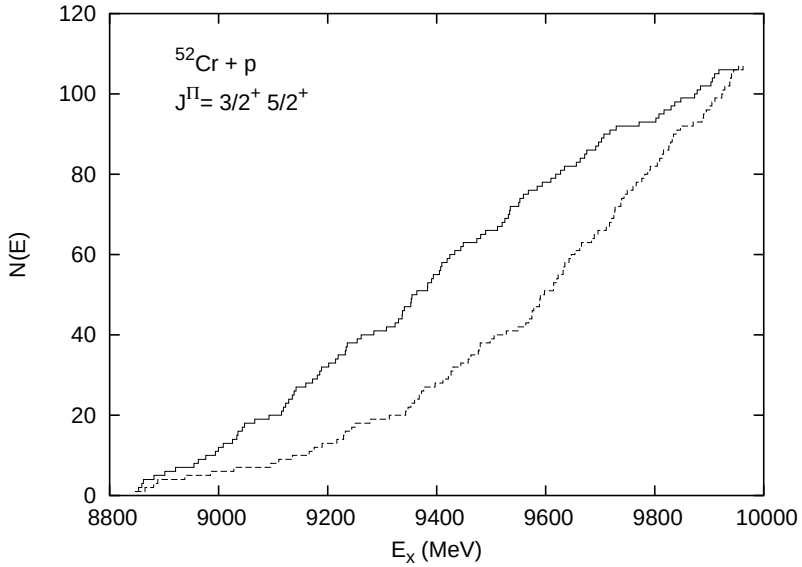

Figure C.4: Integrated level density N(E) for the $J^{\pi} = \frac{3}{2}^{+}$, $\frac{5}{2}^{+}$ combined sequence. The experimental energies are shown by the dashed line while the solid line represents linearized values.

Bibliography

[Agv03] U. Agvaanluvsan, G. E. Mitchell, J. F. Shriner, Jr., and M. P. Pato, "Missing Level Corrections in Nuclear Resonances", Nuclear Instruments and Methods in Physics Research **A498**, 459 (2003).

[Bie52] L. C. Biedenharn, J. M. Blatt, and M. E. Rose, "Some Properties of the Racah and Associated Coefficients", Review of Modern Physics **24**, 249 (1952).

[Bil76] E. G. Bilpuch, A. M. Lane, G. E. Mitchell, and J. D. Moses, "Fine Structure of Analog States", Physics Reports **28**, 145 (1976).

[Boh36] N. Bohr, Nature **137**, 344 (1936).

[Con51] E. U. Condon and G. H. Shortley, *The Theory of Atomic Spectra*, Cambridge University Press, Cambridge, 1951.

[Frö80] F. H. Fröhner, "Nuclear Theory and Applications", IAEA-SMR- **43**, 59 (1980).

[Guh98] T. Guhr, A. Müller-Groeling, and H. A. Weidenmüller, "Random Matrix Theories in Quantum Physics: Common Concepts", Physics Reports **299**, 190 (1998).

[Hub54] R. Huby, "Phase of Matrix Elements in Nuclear Reactions and Radioactive Decay", Proceedings of the Physical Society, Section A **67**, 1103 (1954).

[Jän69] J. Jänecke, "Systematics of Coulomb Energies and Excitation Energies of Isobaric Analog States", in *Isospin in Nuclear Physics*, edited by D. H. Wilkinson, North-Holland, Amsterdam, 1969.

[Kap38] P. L. Kapur and R. E. Peierls, Proc. Roy. Soc. **A166**, 277 (1938).

[Lan58] A. M. Lane and R. G. Thomas, "R-Matrix Theory of Nuclear Reactions", Reviews of Modern Physics **30**, 257 (1958).

[Lyn68] J. E. Lynn, *The Theory of Neutron Resonance Reactions*, Clarendon, Oxford, 1968.

[Mat83] T. Matsuzaki and E. Arai, Zeitschrift fur Physik **A313**, 293 (1983).

[Meh91] M. L. Mehta, *Random Matrices*, Academic Press, New York, second edition, 1991.

[Mos70] J. D. Moses, *A High Resolution Study of Isobaric Analog Resonances in* ^{51}*Mn,* ^{53}*Mn, and* ^{55}*Mn*, Ph.D. thesis, Duke University, 1970.

[Mos71] J. D. Moses, H. W. Newson, E. G. Bilpuch, and G. E. Mitchell, "Fine Structure of Analogue States in ^{51}Mn, ^{53}Mn, ^{55}Mn", Nuclear Physics **A175**, 556 (1971).

[Nel83] R. O. Nelson, *Proton Resonance Spectroscopy in* ^{28}*Si and* ^{30}*P*, Ph.D. thesis, Duke University, 1983.

[Nnd04] National Nuclear Data Center, www.nndc.bnl.gov/masses, 2004.

[Oza85] Y. Ozawa, Y. Oguri, and E. Arai, "High Resolution Measurements of Analog States in ^{53}Mn", Nuclear Physics A **440**, 13 (1985).

[Por56] C. E. Porter and R. G. Thomas, "Fluctuations of Nuclear Reaction Widths", Physical Review **104**, 483 (1956).

[Shr90] J. F. Shriner, Jr., E. G. Bilpuch, P. Endt, and G. E. Mitchell, "Fluctuation Properties of States in ^{26}Al", Zeitschrift für Physik **A335**, 393 (1990).

[Sod87] J. P. Soderstrum, M. A. Boyd, C. R. Gould, and N. R. Roberson, *XSYS Reference Manual*, Triangle Universities Nuclear Laboratory, Durham, NC, sixth edition, 1987.

[Wat81] W. A. Watson, E. G. Bilpuch, and G. E. Mitchell, "Statistical Analysis of Imperfect Eigenvalue Sequences", Nuclear Instruments and Methods **188**, 571 (1981).

[Wig47] E. P. Wigner and L. Eisenbud, "Higher Angular Momenta and Long Range Interaction in Resonance Reactions", Physical Review **72**, 29 (1947).

[Wig65] E. P. Wigner, in *Statistical Theories of Spectra: Fluctuations*, edited by C. E. Porter, Academic Press, New York, 1965.

[Wim74] J. F. Wimpey, *Electromagnetic Decay of Fragmented Analogue States in ^{45}Sc and ^{63}Cu*, Ph.D. thesis, North Carolina State University, 1974.

[Wyl71] W. Wylie, F. Zamboni, and W. Zych, Helvetica Physica Acta **44**, 757 (1971).